ETH zürich

IMBRSea

Variability Of Water Column Denitrification and its Drivers in the Eastern Tropical Pacific Oxygen Deficient Zones

Andrea van Langen Rosón

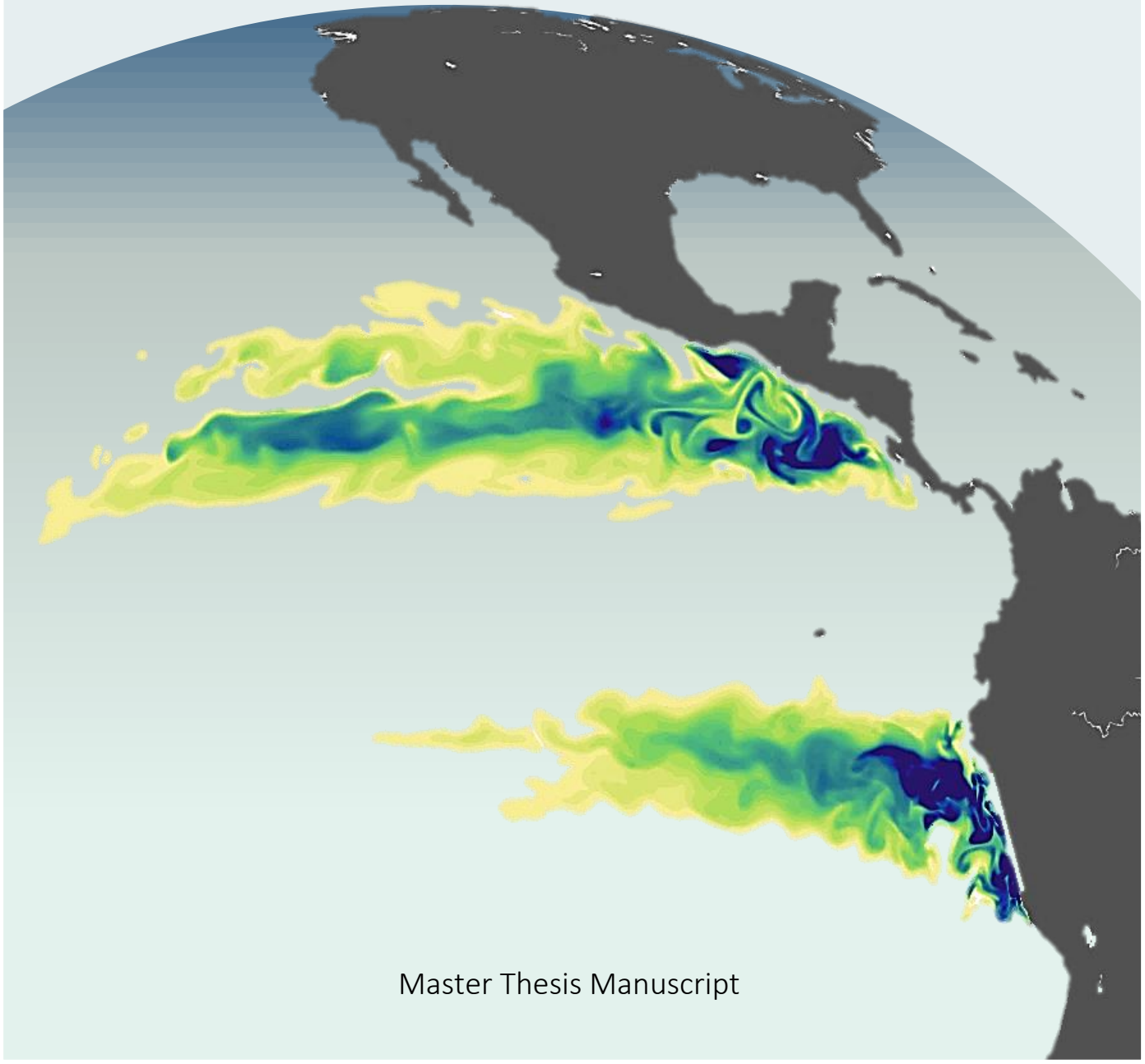

Master Thesis Manuscript

No data can be taken out of this work without prior approval of the thesis promoter / supervisor (*)

The journal guidelines followed in this thesis are from Global Biogeochemical Cycles, ISSN: 0886-6236.

Variability Of Water Column Denitrification and its Drivers in the Eastern Tropical Pacific Oxygen Deficient Zones

By

Andrea van Langen Rosón

in partial fulfilment of the requirements for the degree of

Master of Science
in Marine Biological Resources

Supervisors:

Prof. Dr. Nicolas Gruber,	ETH Zürich
Dr. Eike Köhn,	ETH Zürich
Jana Härri,	ETH Zürich

Zürich, 06.06.2023

Executive Summary

Water column denitrification (WCD) is the primary pathway for organic matter remineralization under suboxic conditions. The Eastern Tropical Pacific (ETP) oxygen-deficient zones (ODZs) are major regions of marine WCD, resulting in oceanic nitrogen (N) loss, a crucial nutrient for marine life. WCD in the ETP is characterized by strong intra-annual to decadal variability, yet major uncertainties remain concerning the magnitude and mechanisms driving these fluctuations. In this study, the processes inducing WCD variability were characterized using a 41 year hindcast simulation of a regional coupled physical-biogeochemical ocean model over the period 1979 to 2019. The annual N loss in the ETP was estimated at 52.9 Tg N yr^{-1}, with increases of up to 8 Tg N $month^{-1}$, a doubling of the mean WCD rate, within a 7-month period. WCD occurs predominantly at the upper ODZ boundaries, where high organic matter fluxes, and the shoaling and expansion of the ODZ synergistically increase WCD. The stable ODZ cores (~10°N 90°W and ~7°S 80°W) contribute the most to WCD and are surrounded by regions of increasing variability. The highly variable regions at the ODZ edges, despite their smaller ODZ volume and shorter residence time, have the highest WCD rates. This highlights the importance of mesoscale variability, such as eddies, in controlling WCD. Additionally, climatic variability significantly influences WCD in the ETP, particularly in the ODZ cores. On seasonal timescales, wind-induced upwelling during austral summer drives higher WCD rates in the Southern ETP, while intermittent gap winds during boreal winter and spring increase WCD rates in the Northern ETP. The El Niño Southern Oscillation (ENSO) describes 54% of the interannual WCD variability, with La Niña episodes enhancing mean WCD rates by 51% and El Niño episodes decreasing mean WCD rates by 47%. The Pacific Decadal Oscillation (PDO) accounts for 15.7% of the decadal WCD variability. The close correlation of the PDO to the WCD drivers suggests that the PDO induces a similar, but smaller, response as ENSO on WCD. Furthermore, our findings underscore the challenges of studying WCD events in situ due to the superimposed strong variability. Lastly, we show that WCD drives a 20% increase in N limitation, affecting the euphotic zones above the ODZs and extending into the central Pacific. Altogether, the strong WCD variability and consequential N deficiency have potential implications for primary productivity and the efficiency of the biological pump, thus acting as a positive feedback for climate change.

Abstract

In the Eastern Tropical Pacific (ETP) oxygen-deficient zones (ODZs), organic matter remineralization occurs through water column denitrification (WCD), leading to an estimated annual nitrogen (N) loss of 52.9 Tg. In this study, through ROMS-BEC hindcast simulations, we characterize the processes driving WCD variability in the ETP and examine its implications. This study found that WCD predominantly occurs at the upper boundaries of the ODZs, where enhanced organic matter fluxes, and the shoaling and expansion of the ODZ synergistically intensify WCD. The stable ODZ cores contribute the most to WCD. However, the variable outer edges of the ODZs exhibit the highest WCD rates, despite their smaller volumes and shorter residence times, highlighting the influence of mesoscale variability in controlling WCD dynamics. The seasonal cycle, through wind-induced upwelling, enhances WCD during austral summer in the Southern ETP, whereas intermittent gap winds during boreal winter and spring enhance WCD in the Northern ETP. The El Niño Southern Oscillation drives a ~50% increase in WCD during La Niña episodes, while the Pacific Decadal Oscillation describes 15.7% of the decadal variability in WCD. WCD leads to a 20% increase in N limitation, impacting the euphotic zone, with potential implications for primary productivity and the efficiency of the biological pump.

Table of contents

CHAPTER 1

Introduction

1.1 Water Column Denitrification in a Changing Ocean

Nitrogen (N) is a key element in the functioning of marine ecosystems, acting as a limiting nutrient for primary production, and is mainly governed by biological processes in its oceanic cycling. While N is primarily introduced into the oceans through N fixation, canonical denitrification and anaerobic ammonium oxidation (anammox) lead to the substantial loss of oceanic N (Gruber, 2008; Sigman and Casciotti, 2001). In this study, these processes are jointly referred to as water column denitrification (WCD). At suboxic conditions, WCD becomes the dominant pathway of remineralization of organic matter (Ward et al., 2009; Sigman and Casciotti, 2001). WCD is mediated by heterotrophic and lithoautotrophic bacteria (Strous et al, 1999), which employ nitrate (NO_3^-) as an alternative oxidant for respiration. Through a sequence of individually regulated reactions (Graf et al., 2014; Dalsgaard et al., 2012), denitrifiers convert NO_3^- to nitrite (NO_2^-), then to nitric and nitrous oxides (NO, N_2O) and finally to N gas (N_2). The stoichiometric formulas of these processes can be written as shown in Equations 1 and 2 (Gruber, 2008).

Heterotrophic denitrification:

$$C_{106}H_{175}O_{42}N_{16}P + 104NO_3^- \rightarrow 106CO_2 + 60N_2 + H_3PO_4 + 138H_2O \qquad (1)$$

Anammox:

$$NO_2^- + NH_4^+ \rightarrow 2N_2 + 2H_2O \qquad (2)$$

Marine oxygen deficient zones (ODZs) in the water column, where oxygen (O_2) concentrations drop below 5 mmol m^{-3}, are hotspots of WCD and account for up to 50% of the oceanic N loss (DeVries et al., 2013). These ODZs have extensive effects on global N cycling, despite the fact that they occupy merely ~0.05% of the global oceans (Löscher et al., 2016). The Eastern Tropical Pacific Ocean (ETP) hosts the two largest ODZs in the world (Karstensen et al., 2008; Paulmier and Ruiz-Pino, 2009) and accounts for 15-40% of all fixed N loss in the ocean (Yang et al., 2017). ODZs emerge between 300-700m depth (Busecke et al, 2022) in regions where O_2 consumption is high and the supply of O_2 is low (Sarmiento and Gruber, 2006). In the eastern boundaries of the subtropical gyres and along the Equator, strong upwelling of nutrient-rich waters fuels biological productivity and the downward export of organic matter, inducing high respiration rates and limiting the transport of O_2 to depths, thereby leading to the development of ODZs in subsurface waters (Karstensen et al., 2008; Cabré et al., 2015). The ETP ODZs are located in the so-called 'shadow zones', where relatively old water ages indicate poor ventilation (Luyten et al. 1983; Paulmier and Ruiz-Pino, 2009; Karstensen et al., 2008; Stramma et al., 2010). At the equator, the ODZs are separated into a northern and southern part due to ventilation by the oxygen-rich eastward-flowing Equatorial Undercurrent (EUC) in the thermocline (Stramma et al., 2010; Cabré et al., 2015; Busecke et al., 2019). The ETP region is highly dynamic, with complex physical and biological processes that lead to strong natural fluctuations in the volume and distribution

of the ODZs on a range of timescales, which subsequently translates to a pronounced variability in WCD (Deutsch et al., 2011).

The human-induced climate warming has resulted in a decrease in O_2 solubility, which combined with increased stratification of the water column reduces the ventilation of subsurface O_2, leading to subsurface O_2 depletion (Keeling et al., 2010; Schmidtko et al., 2017; Keeling and Garcia, 2002). As a consequence, ODZs are projected to undergo changes in size and distribution (Busecke et al., 2022; Deutsch et al., 2011; Zhou et al., 2022), with severe consequences for marine biogeochemistry and ecosystems. Moreover, the use of industrial N fertilizers and the burning of fossil fuels has led to an increased release of N into the atmosphere, augmenting the N deposition over the oceans and altering the natural balance of the marine N cycle (Yang and Gruber, 2016). Despite their significance, the effects of ODZs on biogeochemical cycles in the marine ecosystems are still poorly understood, especially in the open ocean (Gruber et al., 2021).

1.2 Previous Research and Knowledge Gaps

A major impediment to estimating changes in the marine N cycle is the uncertainty about the rates, distribution, and sensitivity of WCD to climatic forcing. The few available studies on WCD in the ETP have shown that rates of WCD are considerably sensitive to temporal climatic variability (Yang et al., 2017; Deutsch et al., 2011; Horak et al., 2016). This variability can be attributed to changes in biological productivity and the structure of ODZs, which are in turn determined by physical influences on different temporal timescales (Yang et al., 2017; Köhn et al., 2022; Deutsch et al., 2011). The current notion is that, during enhanced upwelling, increased nutrient availability in the euphotic zone promotes primary production and thereby increases the export of organic matter to depths. The upwelling of subsurface low-oxygenated waters moreover leads to the shoaling of the ODZs. Furthermore, increased organic matter export fluxes drive a high O_2 demand for organic matter remineralization, which increases O_2 depletion and contributes to the expansion of the ODZs (Cabré et al., 2015). When organic matter export coincides with the suboxic conditions of the ODZ, WCD arises. Hence, WCD is dependent on the extent of the ODZ, both its volume and its distribution in the water column, and the availability of organic matter for remineralization. The processes driving, and being driven by, WCD are illustrated in Figure 1. As shown in Figure 1, the downward sinking of organic matter for remineralization is represented as the POC (particulate organic carbon) export.

The N* tracer serves as a metric for constraining WCD rates and understanding the impact of WCD on the marine ecosystem. Variability of oceanic N is mostly determined by the biological pump, which can be separated into two components: N consumption and release by plankton, adhering to the nitrogen-to-phosphorus (N:P) Redfield ratio, and the influence of denitrification and N fixation, where N is not converted according to the Redfield ratio. The N* concentration, which is calculated according to Equation 3, is based on the average nitrate-to-phosphate Redfield ratio in organic matter and includes a correction of 2.90 µmol kg^{-1} to force the global mean of N* to be zero (Gruber and Sarmiento, 1997).

$$N* = [NO_3^-] - 16[PO_4^{3-}] + 2.90\ \frac{\mu mol}{kg} \quad (3)$$

As N* is unaffected by changes due to primary production, the N* tracer can be applied to discern the specific contribution of denitrification and N fixation to the oceanic N variability (Deutsch et al., 2001).

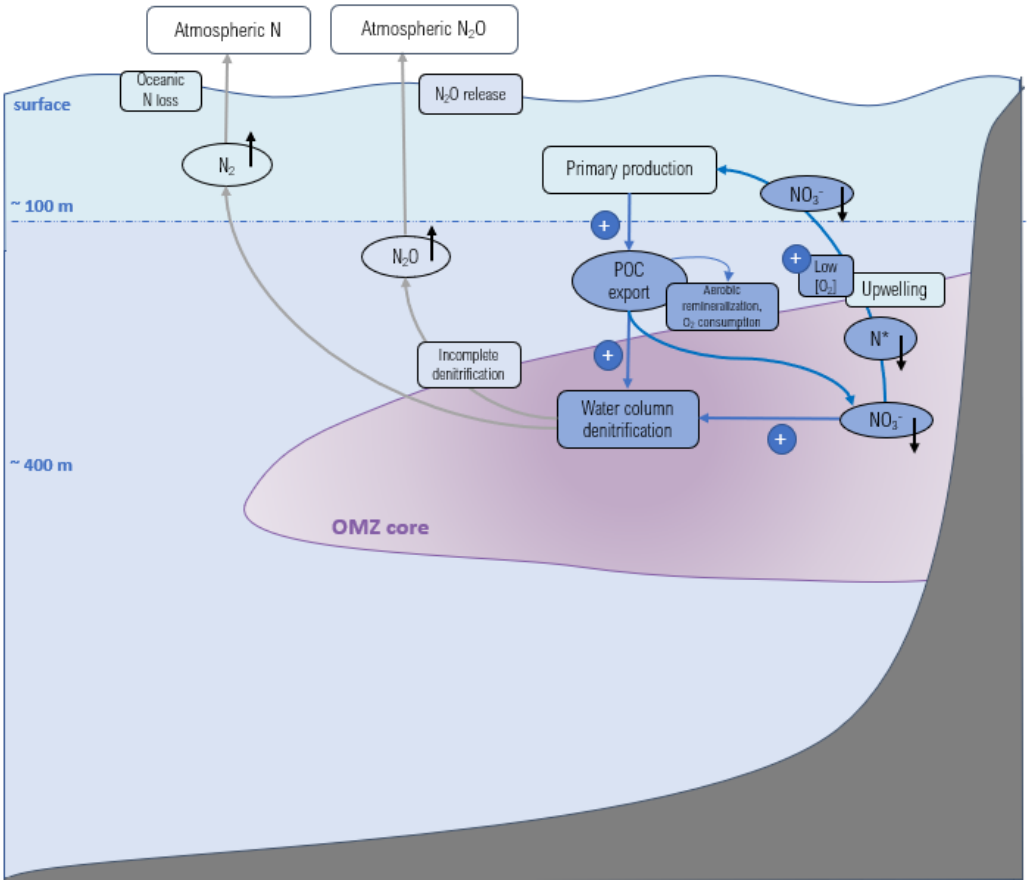

Figure 1. Schematic representation of WCD, its drivers, and its effects. The round boxes represent state variables, while the square boxes indicate processes. In blue are the drivers of WCD. Black upward and downward arrows on variables indicate the impacts of WCD.

1.2.1 Mechanisms Inducing Variability of Denitrification

WCD is affected by several physical and biological processes that span across a range of timescales. At seasonal timescales, subsurface currents, variability of primary productivity and remineralization, and upwelling and downwelling caused by local wind forcing lead to changes in O_2 concentrations and organic matter availability in the ODZs, thereby influencing WCD rates. While the response of ODZs to seasonality has been discussed in previous studies (Paulmier et al., 2006; Paulmier and Ruiz-Pino, 2008), the influence on WCD is not well established and remains a knowledge gap.

On seasonal and subseasonal timescales, WCD is impacted by mesoscale circulation, i.e. eddies and filaments, due to the influence of mesoscale processes in driving the variability in the ODZs (Köhn et al., 2022; Thomsen et al., 2016; Vergara et al., 2016) and organic matter export. Mesoscale eddies are ubiquitous in the ETP and can increase N loss by controlling O_2 supply and by enhancing vertical nutrient transport, thereby stimulating primary production and organic matter export. They can create isolated cores of suboxic waters (Frenger et al. 2018), and as such they can be hotpots of fixed N loss, as observed off the coast ODZ of Peru (Altabet et al., 2012; Callbeck et al., 2017). In this context, cyclonic eddies and anticyclonic mode water eddies are of particular interest, as they can trap strongly deoxygenated waters and lift them closer to the surface (Callbeck et al., 2017). It is therefore important to account for mesoscale and submesoscale processes in the study of N cycles.

At interannual timescales, the El Niño – Southern Oscillation (ENSO) induces strong WCD variations in the ETP. ENSO, a coupled atmospheric-oceanic climate mode, plays a significant role in shaping the climate patterns of the Pacific basin by causing pressure and temperature variations

resulting in the occurrence of distinct warm and cold conditions known as El Niño and La Niña periods, respectively. The ENSO cycle operates on timescales of approximately 2 to 7 years (NCEI, n.d.). Studies on the impact of ENSO on WCD show that variability in WCD rates is caused by wind-driven changes in circulation and isopycnal structure (Horak et al., 2016), which subsequently amplify the response of WCD through changes in the subsurface O_2 distribution and organic matter export (Yang et al., 2017). A modelling study by Yang et al. (2017) reported relatively low WCD rates during El Niño episodes, while anomalously high rates were registered during La Niña episodes, with changes compared to the mean WCD rates of approximately 20%. Their study found that ENSO enhances WCD through the shoaling and expansion of the ODZ, and by inducing an increased availability of organic matter for remineralization. However, their study combined the effects of El Niño and La Niña into a canonical mean ENSO response, thereby potentially neglecting asymmetries between the individual phenomena. Furthermore, the study by Yang et al. (2017) did not discern geographically-differing effects of ENSO on WCD and its drivers in the ODZ.

On decadal and longer timescales, WCD in the ETP is influenced by the Pacific Decadal Oscillation (PDO). Similarly to ENSO, the PDO induces fluctuations in sea level pressures and temperatures and is characterized by alternating phases of warm and cool sea surface temperature anomalies. However, PDO events occur on multi-decadal timescales lasting from 20 to 30 years (Mantua and Hare, 2002). Studies on the impact of PDO on WCD have reached contrasting conclusions. Deutsch et al. (2011) found that WCD is affected by the PDO, with an expansion of suboxic waters and WCD during negative (cold) PDO phases. On the contrary, a study by Horak et al. (2016), using hydrographic measurement from four cruises, reported that O_2 and N loss in the ETNP ODZ could not be explained by the PDO. Horak et al. (2016), however, solely analyzed the vertical expansion of the ODZs and WCD, thereby overlooking the large variability induced in the horizontal dimension. While the PDO induces changes in the dissolved O_2 concentrations in the ETP (Poupon et al, 2023), its contribution to WCD remains to be further investigated. All combined, the processes inducing climatic variability contribute to the extensive variability of WCD in the ETP.

1.2.2 Implications of Denitrification on Marine Life

In recent years, the study of the marine N cycle has gained attention due to its widespread impact on i.a. marine ecosystem health, biodiversity and climate change (Pajares & Ramos, 2019). The marine N cycle is highly dynamic, with an average residence time of merely 3000 years (Gruber, 2008). WCD leads to the loss of bioavailable N in the oceans and the production of the potent greenhouse gas (GHG) N_2O (Babbin et al., 2015; Battaglia et al., 2018; Codispoti, 2010). As a key nutrient for primary production, the bioavailability of N has implications for plankton and for carbon (C) sequestration. Given the relatively short residence time of oceanic N, WCD can swiftly cause an imbalance in the marine N cycle, thereby profoundly impacting global marine productivity (Gruber, 2008). These N deficient waters can be upwelled to the euphotic zone above the ODZ and could disturb primary production in this region. Indeed, a study by Chang et al. (2010) on measured N_2, aragonite and nutrient concentrations in the ETSP ODZ showed the N deficiency maximum at the top of the ODZ at around 100m depth, which furthermore created a N deficiency at the surface. This finding agrees with the assumption that N loss through WCD can lead to a decrease in N in the euphotic zone and thereby affect primary production. Moreover, a study by Löscher et al. (2016) comparing ODZs in the eastern tropical North Atlantic and ETSP reports a lower rate of primary production in the ETSP corresponding to a significantly stronger deficit in N:P ratio, which further corroborates this hypothesis.

In addition, the C cycle is interconnected with the N cycle, as the amount of N available plays a critical role in determining how effectively the biological pump can absorb atmospheric CO_2

(Falkowski, 1997; Gruber and Sarmiento, 1997; Neuer, 2002; Karl et al., 2002). The biological pump refers to the biologically mediated sequestration of C from the atmosphere and surface ocean to the deep ocean (Longhurst and Harrison, 1989). Therefore, understanding the impact of WCD on N availability is of crucial importance to anticipate and potentially mitigate the evolution of climate change (Gruber & Galloway, 2008; Deutsch et al., 2011). Major knowledge gaps remain regarding the intertwined impacts of the N and C biogeochemical cycles, and their implications for the oceans and climate under the influence of climate change. As aptly stated by Gruber et al. (2021, p.395), in light of the changing dynamics of i.a. low O_2 extremes, 'The conditions exhibited by present extreme events may be a harbinger of what may become normal in the future'. Through the study and quantification of the interactions between the N cycle and ODZs, and by relating these to their effects on marine biological resources, we may be able to create a window on the future state of the oceans.

1.3 Aim of the Study

Multiple studies have estimated the mean rate of WCD in the ETP, however, only a handful have shed light on the general drivers of WCD and its response to decadal and interannual variability. Through this study I aim to (1) improve the current understanding of the spatiotemporal variability of WCD and its drivers, (2) determine how the dominant climatic modes of variability in the ETP impact WCD, and (3) assess the potential perturbations induced by WCD for the marine ecosystem. These dynamics are studied in the two largest and most intense ODZs in the world's oceans through three main research questions:

1. What is the spatiotemporal variability of WCD and its drivers?
2. How do the dominant climatic processes at different timescales influence WCD in the ETP?
3. What are the potential impacts of WCD on primary production and the efficiency of the biological pump?

We hypothesize that (**1**) WCD variability is strongly determined by the variability of the ODZ extent and organic matter reaching the ODZ, with large fluctuations in WCD attributed to the expansion and contraction of the ODZs, and in particular to their vertical displacement in the water column. The belief is that the upper boundary of the ODZ contributes over-proportionally to the total WCD. A potential reason for this is that when ODZs occur relatively close to the surface, the organic matter availability is high and thus the need for an oxidant is large (Yang et al., 2017). Consequently, we expect to find the main bulk of WCD occurring at the top of the ODZs. Furthermore, we expect to visualize a strong effect of mesoscale dynamics on the ODZ outer regions driving episodic occurrences of WCD. The expectation is that the different ODZ variability regions elicit a distinct response in WCD, thereby contributing in different ways, and to different capacities, to the net N loss. Additionally, we predict to capture synergistic effects between the WCD drivers due to the simultaneous expansion of the ODZ and increased availability of organic matter, forced by natural climatic variability.

In terms of climatic forcing on WCD in the ETP, we hypothesize (**2**) to capture strong variability in WCD induced by the seasonal cycle, ENSO and PDO. In response to the physical and biological changes induced by the seasonal cycle, we expect to capture an effect in WCD associated to the intensification of tropical winds and upwelling of oxygen-poor and nutrient-rich waters, particularly inducing an increase of WCD during boreal winters. We expect to observe large interannual variability of WCD forced by ENSO, with higher WCD rates during La Niña episodes, related to the synergistic effects of the WCD drivers, while the inverse effect applies to El Niño episodes. We expect to find

similar mechanisms driving WCD enhancement during negative PDO phases, and WCD decrease during positive PDO phases.

Lastly, as a consequence of marine WCD, we hypothesize to (**3**) detect a strong decrease in N* that potentially reaches the euphotic zone, thereby having implications on primary production in the area and reducing the efficiency of the biological pump. Consequently, the diminished biological pump efficiency will contribute to increased CO_2 loss from the ocean to the atmosphere.

The study of WCD is constrained due to limited observational data availability and the large climatic variability introduced by i.a. ENSO and PDO. Understanding the mechanisms driving WCD dynamics requires the study of the spatial distribution of ODZs in a three-dimensional (3D) framework, and its concurrent effects with organic matter variability. To this end there is a need for a comprehensive analysis including both a realistic description of the N cycle and oceanic circulation in the ETP ODZs. However, due to the complex interconnectivity of the processes and the high O_2 variability in the ETP, global models often struggle to accurately represent the ODZs (Cabré et al., 2015; Margolskee, 2019; Frölicher et al., 2009, 2020; Busecke et al., 2019). To overcome these challenges, a hindcast simulation over 41 years of an eddy-resolving regional ocean model of the ETP was employed. By leveraging a high-resolution regional model, a more accurate representation of the WCD processes in the ETP is provided, accounting for the variability in the ODZ.

CHAPTER 2

Materials and Methods

To study the variability of WCD, the ETP was chosen as the study area. The ETP comprises two of the three largest ODZs in the oceans, namely in the Eastern Tropical North Pacific (ETNP) and the Eastern Tropical South Pacific, two regions that are characterized by high WCD rates (Deutsch et al., 2007).

2.1 Model Description

To study the interconnected processes that influence WCD variability in the ETP ODZs, a regional physical-biogeochemical coupled model was employed. The physical model component constitutes the UCLA-ETH version of the Regional Oceanic Modelling System (ROMS, Marchesiello et al., 2003; Shchepetkin & McWilliams, 2005). The eddy-permitting model configuration allows for the comprehensive spatiotemporal analysis of the processes involved in WCD in the ETP. By solving the incompressible, hydrostatic, primitive equations, the circulation model simulates the three-dimensional flow that varies over time (Marchesiello et al., 2003). The model is run on a telescopic grid setup over the Pacific basin with refined horizontal grid resolution toward South America at 2°S 63°W (Figure 2). As a result, the horizontal grid resolution varies from ~40 km around the Western Pacific to a finer resolution of ~4 km along the Peruvian coastline. This provides the highest model resolution in the ETP, the region of focus in the analysis of WCD. The model utilizes an orthogonal, curvilinear coordinate system in the horizontal field (1009 x 701 grid points), with state variables discretized on a staggered Arakawa C-grid. In the vertical dimension, state variables are discretized on terrain-following σ-coordinates with 64 levels up to 6500 m depth. The model has a finer resolution at the sea surfaces and a gradual decrease in resolution with depth, with subsequent refinement toward the sea floor. In the grid used, the boundaries of the Indonesian Throughflow and the Bering Strait are closed, while the lateral boundaries in the Southern Ocean in the Drake Passage, and between Antarctica and Australia, are open.

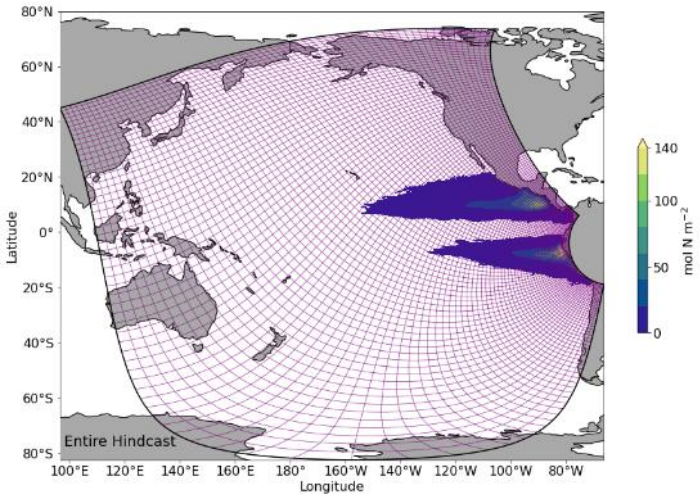

Figure 2. Model domain and horizontal grid structure. The purple lines indicate every 10th grid line. Background colours show the time- and depth-integrated WCD rates for the ROMS-BEC 1979–2019 hindcast.

The biogeochemical and ecosystem module is modelled through the Biogeochemical Elemental Cycling (BEC) Model, a marine plankton functional type (PFT) model (Moore et al., 2004, 2013). The BEC component simulates the cycling of six key elements in the oceans (N, C, oxygen (O), P, iron (Fe) and silicon (Si)) and represents phytoplankton through three explicit PFTs, namely small phytoplankton, diatoms and diazotrophs. Phytoplankton growth is limited by four key nutrient elements, i.e. N, P, Si and Fe, light conditions and temperature. Grazing is represented by one zooplankton class that grazes on all PFTs, with the grazing parameters and remineralization routes adjusted to each PFT.

In the BEC model, phyto- and zooplankton mortality, as well as zooplankton grazing, contribute to the production of particulate matter. POM (particulate organic matter) and DOM (dissolved organic matter) represent the two detrital pools, which are remineralized back into inorganic nutrients. POC sinking is explicitly represented through the assignment of a sinking velocity and a remineralization rate (Frischknecht et al., 2018). POC fluxes at high depths have been shown to be closely correlated to fluxes of ballast minerals (carbonate ($CaCO_3$) and opal (SiO_3); Iversen and Ploug, 2010; Armstrong, 2001; Frischknecht, 2018). Therefore, POC fluxes are composed of fractions of free (Φ_{poc}^{free}) and ballast mineral ($\Phi_{poc}^{mineral}$) fluxes, with explicit remineralization rates for the different particulate pools. The rate of POC remineralization at any given depth z, $J_{poc}^{remin}(z)$ follows mass conservation, and is dependent on the rate of POC production J_{poc}^{prod} (Yang, 2017), as shown in the following Equation:

$$J_{poc}^{remin}(z) = J_{poc}^{prod}(z) + \frac{d}{dz}(\Phi_{poc}^{free}(z) + \Phi_{poc}^{mineral}(z)) \quad (4)$$

The BEC model includes all major processes of the marine N cycle i.e. oceanic input of N through N_2 fixation, atmospheric deposition and riverine inputs, and N loss through WCD, sedimentary denitrification and burial of N (Figure 3). In the model, anammox and canonical denitrification processes are combined in one state variable, WCD, which is parametrized to be representative of the combined reactions happening in the ETP. The WCD rate J_{WCD} is dependent on the rate of organic matter remineralization J_{poc}^{remin} (Kalvelage et al., 2013) and the changes in O_2 distribution that determine the volume over which WCD occurs (Yang et al., 2017; Löscher et al., 2016). In this study, ODZs are defined as subsurface waters with O_2 concentrations of less than 3 mmol m^{-3}, a value low enough to elicit WCD. J_{WCD} is parametrized such that it sets in at the O_2 threshold O_2^{onset} = 3 mmol m^{-3} and increases linearly with a decreasing [O_2] until it reaches a maximum rate at O_2^{full} = 1 mmol m^{-3}. The maximum J_{WCD} is calculated by multiplying the organic C remineralization rate J_{remin} with the conversion efficiency $R_{N:C}$, set at 112:117, reflecting the moles of NO_3^- consumed per moles of organic C (Yang et al., 2017). Therefore, WCD is calculated as follows:

$$J_{WCD}(x,t) = R_{N:C} \cdot H(O_2(x,t)) \cdot J_{remin}(x,t) \quad (5)$$

where

$$H(O_2(x,t)) = \begin{cases} 1, & if\ O_2(x,t) < O_2^{full} \\ \frac{O_2^{onset} - O_2(x,t)}{O_2^{onset} - O_2^{full}}, & if\ O_2^{onset} \le O_2(x,t) \le O_2^{full} \\ 0, & if\ O_2(x,t) > O_2^{onset} \end{cases} \quad (6)$$

To ensure that WCD does not yield negative [NO_3^-], under $[NO_3^-]_{min}$ = 5 mmol m^{-3}, the J_{WCD} is reduced with the following Equation 7, where N_{no3} is the amount of NO_3^- available:

$$J^{WCD} = \begin{cases} J^{WCD}, \ if \ N_{no3} > NO_{3\,min}^{-} \\ \frac{N_{no3}}{NO_{3\,min}^{-}} J^{WCD}, \ if \ N_{no3} < NO_{3\,min}^{-} \end{cases} \quad (7)$$

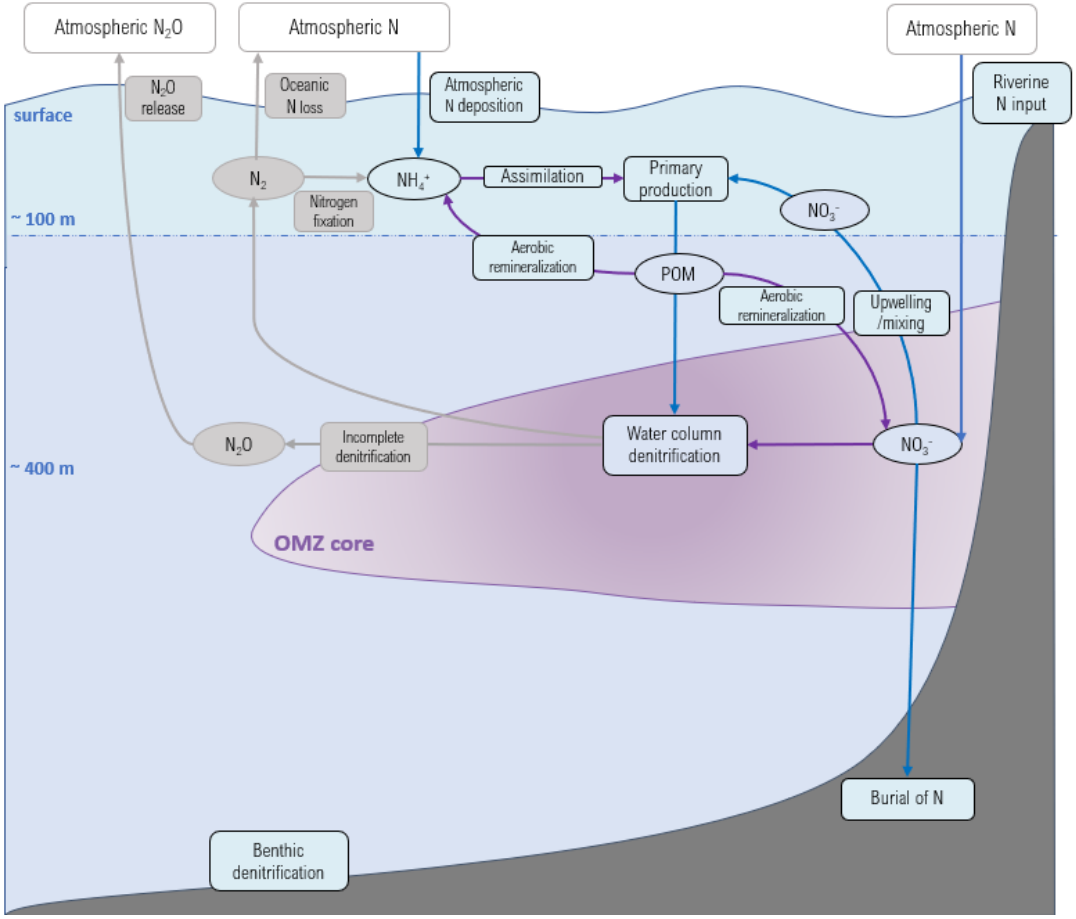

Figure 3. Schematic representation of the marine N cycle as modelled in ROMS-BEC. State variables are depicted as round boxes and processes are represented by square boxes. The purple arrows indicate processes and the blue arrows indicate transport of state variables. The processes in grey are not simulated by the BEC model.

2.2 Hindcast Simulations

The model simulation was performed by Köhn et al. (2023a, in prep; 2023b, in prep). The hindcast simulation runs from 1979 until 2019. The spin-up process consists of two 10-year spin-up phases, the first one using only the physical module and the second incorporating the BEC module. The spin-up is initialized with data from World Ocean Atlas 2018 data (WOA2018, Boyer et al., 2019), SODA3.4.2. (Carton et al., 2018), GLODAPv2.2016b (Lauvset et al., 2016), CESM-BEC (Yang et al., 2017) and SeaWiFS (NASA-OBGP, 2014). A climatological normal year forcing is applied in both spin-up phases. This is constructed from the monthly climatology with daily forcing anomalies of a single year (2001), allowing the model to achieve a representative mean forcing while still experiencing day-to-day variability (Köhn, 2023). To avoid a bias toward higher pCO_2 levels associated with the significant increase in atmospheric pCO_2 between 1979 and 2019, during the spin-up phase atmospheric pCO_2 and boundary DIC values linearly increase from 1969 until 1978 (Köhn, 2023). Open boundary conditions in the Southern Ocean use monthly climatologies from the SODA3.4.2 reanalysis dataset (1980-2017; Carton et al., 2018). The model is forced with daily forcing fields of ERA5, a global reanalysis product produced by the European Center for Medium Range Weather Forecast (ECMWF, Hersbach et al.,

2020). Additionally, the model includes riverine freshwater inputs and their N and P loads, as well as N deposition from the atmosphere. A Drakkar Forcing Set (DFS5.2) correction is applied to the ERA5 surface forcing data to reduce warm biases introduced by the lack of cloud cover in the reanalysis product (Dussin et al., 2016). Furthermore, sea-ice corrections are performed to scale momentum, radiative energy and atmospheric deposition fluxes at the sea surface (Haumann, 2016). Model sea surface temperatures (SST) are restored to the climatology at every timestep to adjust the model output with observations. The spin-up and hindcast are integrated with a time step of 600 seconds, and daily-averaged output fields are saved. As the processes studied are on monthly or longer timescales, the daily fields are downsampled to monthly averaged fields. This ensures faster run times during the model analyses. A summary of all model output variables used in this study can be found in the Supplementary Material.

2.3 Analysis Framework

2.3.1 Vertical Regridding

To analyze the ODZ and WCD at fixed depth levels, the native bathymetry-following model grid with s-level coordinates is vertically regridded to fixed depth levels (z-levels). The regridding is performed for the upper 1500m, using the maximally stretched s-level coordinates to ensure no additional intermediate depth levels are introduced. The maximally stretched z-levels are acquired by following the s-levels at the deepest model bathymetry location (6500m depth), which yields 46 z-levels (Figure 4). It is important to note that the increasing resolution toward the surface is maintained, however, grid points with a shallower bathymetry have higher resolution in s-level than in z-level coordinates. The regridding is performed for the O_2, WCD, POC, NO_3^- , PO_4^{3-} and density 3D daily averaged fields for the entire hindcast. Monthly averages are calculated from the regridded daily fields.

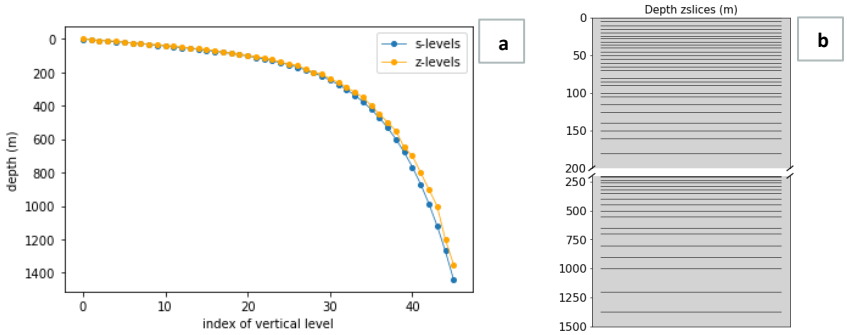

Figure 4. a) shows the chosen depths for the z-levels (orange), based on the maximally stretched s-level depths (blue). b) shows the newly interpolated z-levels with increasing resolution toward depths, up to 1500m depth.

2.3.2 ODZ Variability Regions

In order to analyze the regions within the ODZs based on their variability and examine their differing impact on WCD, the ODZs were sorted into four regions based on the temporal presence of the ODZs during the 1979 to 2019 hindcast. The four categories comprise regions with more than 90%, 90-50%, 50-10% and 10% or less presence of the ODZs throughout the entire hindcast. These regions represent the extremes of low (<=10% presence) and high (>90% presence) variability, as well as the intermediary regions. To be able to analyze the impact of the ODZ variability on WCD in the horizontal and vertical dimensions, two different types of masks were generated. First, a two-dimensional (2D) mask was created that identified the geographical locations of each of the regions, as shown in Figure 5. The classification of each geographical location to one of the four categories was based on the maximum

percentage presence of all the grid cells in the water column at each location. These regions were labeled ZONE90, ZONE50, ZONE10 and ZONE0, from the most stable (90% or more ODZ presence) to the least stable (equal or less than 10% ODZ presence).

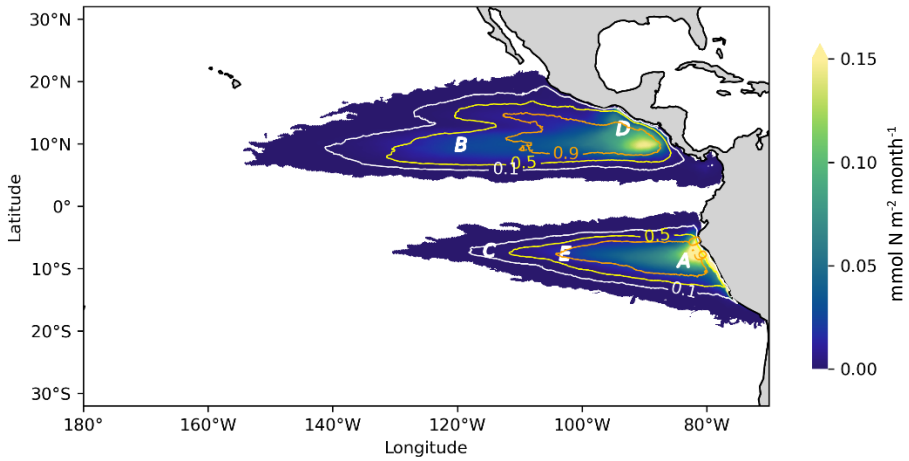

Figure 5. Map of the monthly depth-integrated WCD rates in the ETP. Contour lines show the delineation of the ODZ defined regions. The orange contour line shows the 90% perimeter, yellow the 50% perimeter and white the 10% perimeter. Points A-E indicate the locations chosen for the Hovmöller plots discussed in Section 3.5.

Subsequently, a 3D mask was created based on the ODZ percentage presence of each grid cell in the model, to analyze and quantify the mechanisms occurring within each 3D ODZ variability region. These regions were labelled as ODZ90, ODZ50, ODZ10 and ODZ0, from most stable (>90%) to the most variable (<=10%) ODZ presence regions.

2.3.3 Climatic Modes of Variability: ENSO and PDO

The Oceanic Niño Index (ONI) is an index that describes the state of the oceanic ENSO climate pattern (NOAA, 2009). In this study, it was calculated from the daily model output as the rolling 3-month average SST anomalies in the Niño 3.4 region, located in the east-central tropical Pacific between 120°-170°W. An ONI value of +0.5°C or higher indicates El Niño conditions, while a value of -0.5°C or lower indicates La Niña conditions. An El Niño or La Niña event is defined as a continuous period of at least five months where the ONI exceeds +0.5°C or falls below −0.5°C, respectively (Figure 6). A total of eight El Niño and eight La Niña events were detected during the hindcast. To assess the influence of ENSO on WCD and ODZ variability, a composite of the anomaly fields from all El Niño and La Niña events was created, representing a mean ENSO response. Anomaly fields were obtained by computing the difference between the mean state and the ENSO composites.

The PDO index is calculated as the leading principal component (EOF) of monthly SST anomalies in the North Pacific basin (polewards of 20°N) (Mantua et al., 1997). In this study, the PDO index timeseries for 1979 to 2017 by Mantua et al. (2002) was employed.

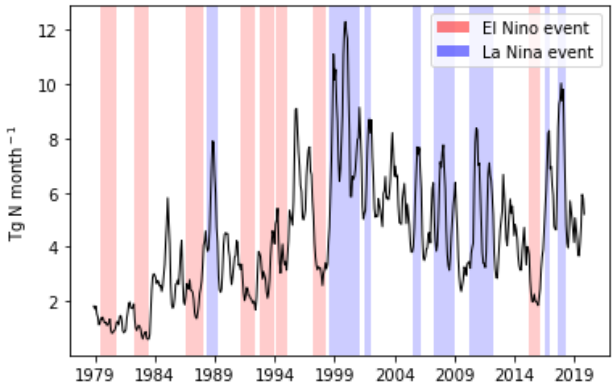

Figure 6. Timeseries of monthly spatially-integrated WCD rates in the ETP, with blue and red color bars indicating La Niña and El Niño events respectively.

To assess the temporal variability of WCD induced by atmospheric and oceanic changes associated with ENSO and PDO, the model output was detrended and deseasonalized, and subsequently correlated with the calculated ONI and PDO index.

In order to correlate the WCD timeseries to the PDO index, high-frequency variability caused by seasonal fluctuations was removed by subtracting monthly climatologies that were calculated over the entire hindcast period from the timeseries.

To correlate the WCD timeseries to the ONI, low-frequency variability related to the PDO was removed by detrending the timeseries (shown in Figure 7). Detrending was performed by applying a Butterworth high pass filter with the function scipy.signal.filtfilt() (Virtanen et al., 2020), with a sampling frequency fs = 12/year and critical frequency Wn = 0.1/year, thereby removing decadal or longer scale variability (Figure 7). This function was chosen as it applies a linear digital filter twice, once forward and once backward, and thus has zero phase. The order N of the filter was set at 5, which defines the sharpness of the frequency cutoff. Thereafter, monthly climatologies were calculated from the detrended timeseries, and subtracted from the original WCD timeseries to obtain the detrended and deseasonalized signal.

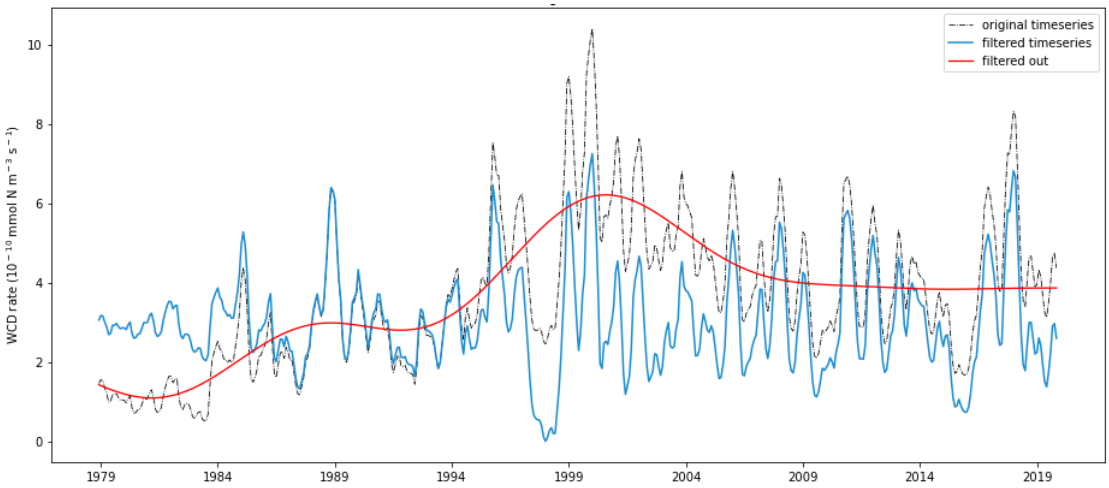

Figure 7. Detrended average WCD rate timeseries in the ETP (blue), showing the original (black striped) and filtered out (red) decadal variability.

2.3.4 Seasonal Composite Analyses

Seasonal composites were computed by taking the mean over the entire hindcast of the variable of choice for the months comprising each of the four seasons. The seasons were defined as follows: March, April and May (MAM); June, July and August (JJA); September, October and November (SON); and December, January and February (DJF). Anomalies were computed by subtracting the seasonal composite mean from the total mean over the entire hindcast. Monthly climatologies were computed in a similar fashion, by taking the averages from the entire hindcast, but for the individual months.

2.3.5 N* Analyses

To investigate the influence of WCD on the N* tracer, and its subsequent impact on primary production in the ETP, a series of analyses were performed. Firstly, the relationship between WCD rates and N* concentrations was examined by mapping a timeseries of the N* concentrations in depth in an Hovmöller diagram (Figure 39). This was performed for the horizontally-averaged ETNP and ETSP ODZs separately. However, to assess changes in N* that are induced by biological sources and sinks, and to avoid confounding effects of heaving-induced density changes, a baseline relationship between N* and density was established. To achieve this, the modelled densities were plotted against the modelled N* concentrations, and a polynomial function was fitted that predicted the N* concentrations based on changes in density (Figure 8). This model was fitted with monthly climatologies at each depth level from 0 to 650m depth, using a least squares polynomial fit numpy.polyfit() (Harris et al., 2020). A 25th-order polynomial was found to accurately represent the changes in N* based on density changes, and subsequently N* concentrations were predicted from the climatological densities using the function numpy.poly1d() (Harris et al., 2020).

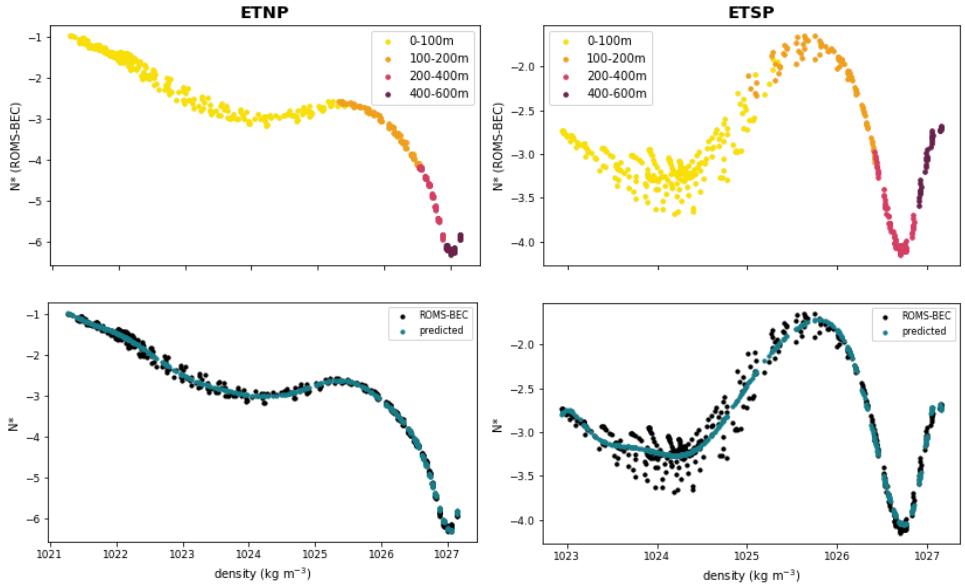

Figure 8. Top: Model N* concentrations plotted against densities, for the ETNP and ETSP ODZ regions separately. Colours indicate the depth bins that the data points belong to. Bottom: Comparison of modelled and predicted N* concentrations plotted against densities.

To verify the accuracy of the polynomial fit, the predicted N* concentrations were plotted against the ROMS-BEC N* concentrations to visualize how well the prediction aligned with the observed data (Figure 9). It was found that the majority of points aligned along the 1:1 axis, indicating a good fit.

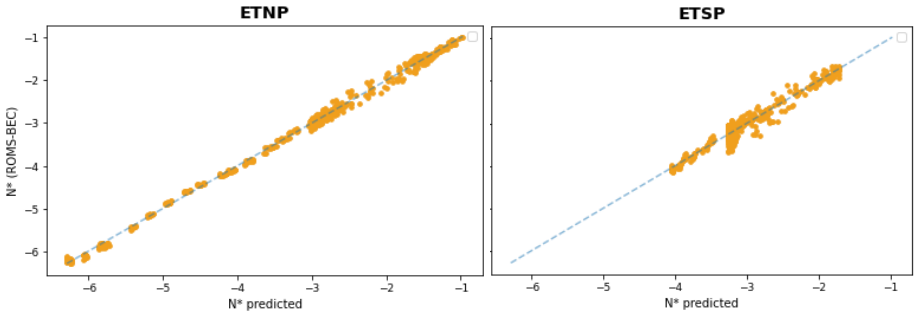

Figure 9. Predicted N* concentrations plotted against modelled N* concentrations for the ETNP and ETSP ODZ regions separately. The blue striped line indicates the 1:1 ratio, where predicted N* concentrations correspond exactly to the modelled N* concentrations.

With the baseline established, N* concentrations were predicted across the entire hindcast from surface to 650m depth from densities using the polynomial function. Solely the top 650m were plotted, since the ODZ upper boundaries reach approximately up to these depths and the aim of this analysis was to study the impact of WCD in the euphotic zone. By subtracting the predicted N* from the modelled N* concentrations, a heaving corrected plot was acquired and any changes in N* not attributed to changes in density were visualized (Figure 40). This allows for a comprehensive analysis of N* residual changes due to biological sources and sinks caused by i.a. WCD, and subsequently its impact on primary production.

2.4 Model Evaluation

The model evaluation performed in this thesis is confined to the model output variables relevant to this study and is supplementary to the model evaluation performed by Köhn (2023).

2.4.1 Oxygen Deficient Zones

A realistic representation of the ODZs and their variability over time and space is crucial to study the WCD dynamics. Frequent shortcomings of modelled ODZs in the ETP include an overestimation of the ODZ extent and inaccurate separation of the northern and southern ODZs (Cabré et al., 2015; Stramma et al., 2010). Therefore, the model evaluation of the ODZ focuses on the comparison of the modelled ODZ to observations in terms of total ODZ volumes as well as the spatial extent in both the vertical and horizontal fields.

The model simulation indicates an average ODZ volume of 16.73×10^5 km^3 in the ETP, with a larger average ODZ volume in the ETNP of 9.73×10^5 km^3, while the ETSP contained an ODZ volume of 7.00×10^5 km^3. Different studies adopt varying O_2 thresholds to define the ODZs, and thus we did not find estimates of the ODZ volumes in the ETP with O_2 concentrations of 3 mmol O_2 m^{-3} or less. To provide a rough quantitative assessment of the robustness of the modelled ODZ, we compared the average ODZ volumes over the two regions to previous estimates that use the 5 mmol m^{-3} O_2 threshold (Table 1). Bianchi et al. (2012) estimated the ODZ volumes in the ETP based on O_2 measurements from the WOCE program and by applying an empirical correction to the WOA observational dataset. Their estimates for the ETNO ODZ volume ranged from $6.7\text{-}24.1\times10^5$ km^3, while the ETSP had an estimated ODZ volume between $0.4\text{-}6.1*10^5$ km^3. Kwiecinski and Babbin (2022) constructed a three-dimensional high-resolution atlas of the ETP ODZs, based on observations from both ship casts and Argo profiles of nearly 15 million measurements collected across 3 decades. Their estimates for the ETNP ODZ volume with O_2 concentrations below 5 µmol kg^{-1} ranged from $16\text{-}19.3\times10^5$ km^3, and for the ETSP ODZ volume between $4.5\text{-}6.1\times10^5$ km^3. Although the ODZ volumes estimated by these two studies are

expected to be larger than our estimate, due to the higher O_2 threshold, the results indicate that the ETSP ODZ constitutes a larger volume in our model than in their estimates. The ETNP ODZ falls to the lower range of the previous estimates, as expected. Nonetheless, the magnitude of the modelled ODZ volume aligns with the findings of these previous studies, indicating the robustness of our modelled ODZ extent.

Table 1. Average volumes of suboxic waters for the ETP ODZs for two O_2 thresholds (5 and 3 mmol m^{-3}).

Study	O_2 threshold	ETNP	ETSP	ETP
Mean ODZ volume (10^5 km^3)				
Bianchi et at. (2012)	<5 mmol m^{-3}	6.7-24.1	0.4-6.1	-
Kwiecinski and Babbin (2022)	<5 µmol kg^{-3}	16-19.3	4.5-6.1	-
This study	=<3 mmol m^{-3}	**9.73**	**7.00**	**16.73**

In order to evaluate the robustness of the modelled ODZ in the spatial extent, the mean simulated ODZ over the entire hindcast was compared to O_2 concentration fields from the high-resolution atlas of the ETP ODZs by Kwiecinski and Babbin (2022; Figure 10). This was performed for three key descriptors, namely the distribution of O_2 concentrations within the ODZ (Figure 10 a-b), the ODZ thickness (Figure 10 c-d) and the ODZ upper boundaries (Figure 10 e-f). Analysis of the model mean O_2 concentrations within the ODZ in the ETP reveals two distinct O_2 deficient cores, located at ~10°N 95°W in the ETNP and 7°S 85°W in the ETSP, where mean O_2 concentrations drop to ~1.5 mmol m^{-3}. The ODZ cores are surrounded by gradually increasing O_2 concentrations toward the ODZ outer edges of the temporal mean ODZ, defined by the 3 mmol m^{-3} O_2 isopleth. In the latitudinal extent, the model shows an accurate separation of the northern and southern ODZs, and depicts the asymmetry between the ODZs, with a larger northern ODZ area than the southern counterpart (Cabré et al., 2015). This can be attributed to the good representation of the equatorial jets (Duteil et al., 2021) and the EUC by the model, which ventilates the ODZ with a west-to-east current (Busecke et al., 2019; Margoslkee et al., 2019; Stramma et al, 2010). The simulated ODZs are located between ~5°N and ~20°N in the ETNP and ~2°S and ~15°S in the ETSP. In the longitudinal extent, the ETNP ODZ reaches ~155°W, while the ETSP reaches ~130°W. These patterns largely match observations (Kwiecinski and Babbin, 2022). Comparison with the observations shows a similar spatial distribution of O_2, with increasing O_2 concentrations in the outer ODZ regions. It is important to note that the observational dataset contains a relatively small number of observations within the ODZ. The data points do not fully cover the ODZ area and moreover, each grid point merely contains on average 54 observations (Figure A1 Appendix A). While the atlas from Kwiecinski and Babbin (2022) provides us with a useful dataset to compare the spatial extent of the ODZ, the comparison between the model and observations is limited by the discrete distribution and limited number of observations below the 3 µmol kg^{-3} oxycline. Thus, minor differences between the model and observations can be attributed to the low and uneven frequency of the observational dataset. The ETNP ODZ spatial extent is in agreement with observations. However, for the ETSP ODZ, important differences are found in the latitudinal extent of the ODZ, where it does not extend as far south along the Peruvian and Chilean coasts as in the observations.

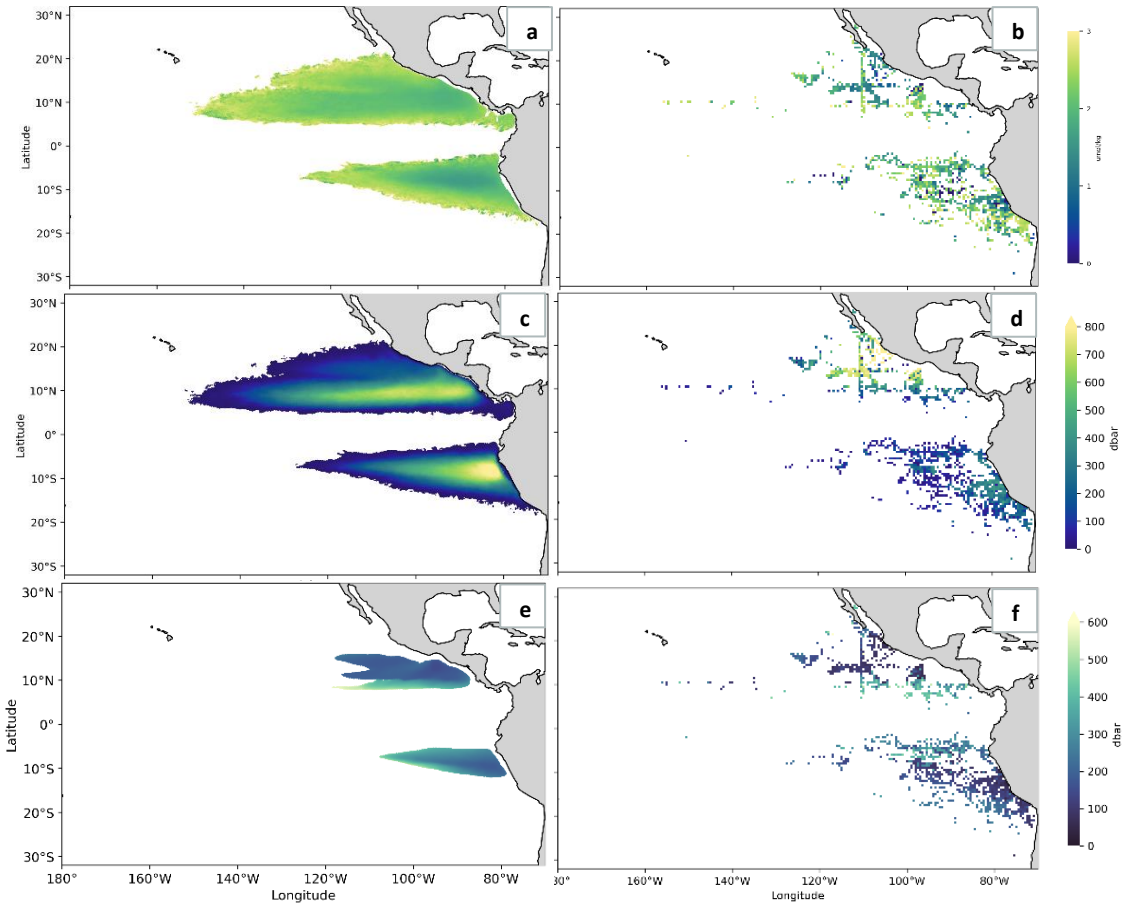

Figure 10. Comparison of the mean modelled ETP ODZs (a, c, e) and observations (b, d, f) by Kwiecinski and Babbin (2022). a-b) mean O_2 concentrations within the ODZ, c-d) mean ODZ thickness, and e-f) mean ODZ upper boundaries.

The vertical ODZ extent is described by the thickness and depth of the 3 mmol m^{-3} oxycline. The ODZ thickness at each grid point is calculated as the summed thickness of grid cells within the water column with concentrations equal to or below 3 mmol O_2 m^{-3}. The model depicts the largest ODZ thickness of more than 800m thickness in the ETNP at ~10°N (Figure 10c). The ODZ thickness is comparable to observations (Figure 10d), with slight differences in individual geographical grid points. A discrepancy is found in the location of the maximum ODZ thickness, as the observational data shows the thickest ODZ extent more to the north, between ~ 10°N and 20°N. The model overestimates the thickness of the ETSP ODZ, however, the observational dataset contains large data gaps in the core region. Overall, the model was successful in reproducing the thickness of the ODZs.

The ODZ upper boundaries were calculated by identifying the shallowest depth in the water column where O_2 concentrations drop below 3 mmol m^{-3}, following the methodology of Köhn et al. (2022), which performs a point-wise linear interpolation between grid neighbouring vertical cells. While the simulated ODZ upper boundary is generally located at ~200-300m depth, it only begins at ~600m depth along 10°N, consistent with observations (Figure 10 e-f). In the core of the ODZ, mean upper boundaries reach between 100-300m depth. Both the model simulations and observations show a shoaling of the upper boundary in the center of the ODZs as it nears the coast. Overall, the modelled ODZs display a good agreement with observations, especially when considering the large discrepancies shown in earlier modelling efforts of the ETP ODZs (Cabré et al., 2015).

2.4.2 Particulate Organic Carbon

To evaluate the simulated POC fluxes, the spatial distribution of mean POC fluxes was compared to observation-based estimates by DeVries and Weber (2017) at 100m depth (Figure 11b). Their estimates are derived from a simple data-assimilative model constrained by satellite and oceanographic tracer observations. The modelled POC export at 100m depth was compared to the observation-based POC export flux at 100m depth, shown in Figure 11. As the ROMS-BEC model simulates POC influxes at the center of the grid cells, instead of the interfaces, it represents the flux of POC at 95m depth (at the interface of the grid cells at 90m and at 100m depth). Here, it is assumed that the POC export flux at 95m depth is approximately the same as at POC export at 100m depth. Quantitative analysis of the modelled POC fluxes reveals that the spatially-integrated annual POC flux at 100m depth equals 4.63×10^{14} mol C year^{-1} (Figure 11a), while the observations show 2.98×10^{14} mol C year^{-1} (Figure 11b). The comparison reveals similar patterns of distribution between the simulated and observed fluxes. However, there are biases in the modelled POC flux magnitudes. The model demonstrates stronger POC fluxes in the highly productive eastern boundaries north of the equator and along the Peruvian coastline (Figure 11c). The overestimation of POC export along the equator reveals the positive bias of primary production, which manifests itself in global BEC applications with similar choices of parameters (Moore et al., 2004, 2013; Frischknecht et al., 2018).

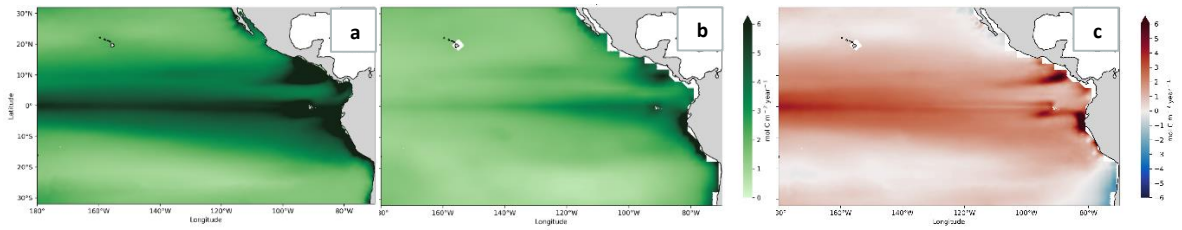

Figure 11. Mean yearly POC fluxes at 100m depth. a) ROMS-BEC simulated POC export. b) POC export fluxes from the observation-based estimate of DeVries and Weber (2017), regridded onto the model grid. c) Difference between modelled and observed POC fluxes.

2.4.3 Water Column Denitrification

The simulated average annual depth-integrated WCD rate in the ETP for the hindcast period from 1979 to 2019 equals 52.9 Tg N year^{-1}. This rate is well within the range of previous estimates, ranging from 34-70 Tg N year^{-1} for the ETP (Table 2 and references therein). The ETNP exhibits an average WCD rate of 31.1 Tg N year^{-1}, in close accordance with previous estimates between 16-52 Tg N year^{-1} (Table 2 and references therein). The ETSP yields an average WCD rate of 21.8 Tg N year^{-1}, again in good agreement with most previous estimates ranging around 18-30 Tg N year^{-1}. Notably, the volumetric WCD rates are higher in the ETSP than the ETNP, with rates of 0.175 mmol N m^{-3} month^{-1} and 0.159 mmol N m^{-3} month^{-1} respectively.

In the spatial extent, the model output (Figure 5) was compared to the WCD rates from a global 3D inverse model by DeVries et al. (2013, Figure 4A). In the ETNP, the mean spatial structure of WCD is defined by a core off the coast of central America at ~10°N 90°W, and a large horizontal extension toward the west up to ~155°W. Comparison with the findings by DeVries et al. (2013) revealed a good agreement in terms of location and intensity of WCD. However, their study reports that the WCD rates extend up to 0°N in the ETNP along the coast, which is not simulated in our model. In the ETSP, the WCD region is smaller, with a strong core off the coast of Peru at ~10°S 80°W, which gradually extends up to ~130°W. DeVries et al. (2013) report a similar distribution, however their WCD region reaches further south along the Chilean coast.

Table 2. Estimates of ETP WCD rates. The volumetric WCD rates were overaged within the ODZs.

Study	ETP	ETNP	ETSP
Annual spatially-integrated WCD rates in Tg N/year			
Tsunogai (1971)			3-7
Codispoti (1973)		19	
Codispoti (1973)		16	
Codispoti and Richards (1976)		23	
Codispoti and Richards (1976)		19	
Elkins (1978)			18-26
Liu (1979)	34-55		
Codispoti and Packard (1980)			25
Codispoti and Packard (1980)			19
Deutsch et al. (2001)	48±5	22±3.5	26±4
Bianchi et al. (2012)	39.1	21.5	17.6
Dalsgaard et al. (2012)			25
DeVries et al. (2012)	44-62	23-29	21-23
DeVries et al. (2013)	41-63		
Yang et al. (2017)	70.3	51.7	18.6
This study	**52.9**	**31.1**	**21.8**
Volumetric WCD rates in mmol N m^{-3} $month^{-1}$			
This study	**0.164**	**0.159**	**0.175**

2.4.4 N* Tracer

The impact of WCD on N limitation can be determined by using the N* tracer, which reflects the influence of N fixation and denitrification on the oceanic N content by comparing the observed NO_3^- concentrations to the available PO_4^{3-} concentrations. To evaluate the model's reproduction of N* patterns across the ETP, the average N* concentrations from the model hindcast were compared with the WOA2018 dataset (Boyer et al., 2019). To this end, the WOA2018 mean N* signal was calculated from monthly climatologies of NO_3^- and PO_4^{3-} concentrations, and the dataset was regridded to the model grid (Figures 12b and 12f). Anomalies were computed by subtracting the observations from the model output. This was done for each grid cell at the sea surface and at 100 m depth and mapped to evaluate the model spatial N* distribution (Figures 12a and 12e). The maps for the sea surface show good coherence, with a slight underestimation of the modelled N* around the equator (Figure 12c). At 100 m depth, the differences between the observed and modelled N* can be partly attributed to interpolation artefacts in the WOA2018 data (Figure 12g). Due to the lower spatiotemporal resolution of the data points used for the WOA2018 dataset, and the employed interpolation method in the generation of the WOA2018 data product, the WOA2018 can locally report values that are not representative. Additionally, the observations show higher N* concentrations along the Peruvian coastline than the model, due to an underestimation of PO_4^{3-} concentrations and an overestimation of NO_3^- concentrations in this area (Figures B1 and B2 Appendix B). These differences can be attributed to biases in the modelled ODZ extent in the ETSP, where observations show a further-reaching ODZ extent to the south along the coastline. This leads to an underestimation of WCD, and concomitantly to

an underestimation of the NO_3^- depletion in the area. In summary, despite minor biases, the model evaluation indicates that the model is an eminent tool to analyze WCD dynamics in the ETP.

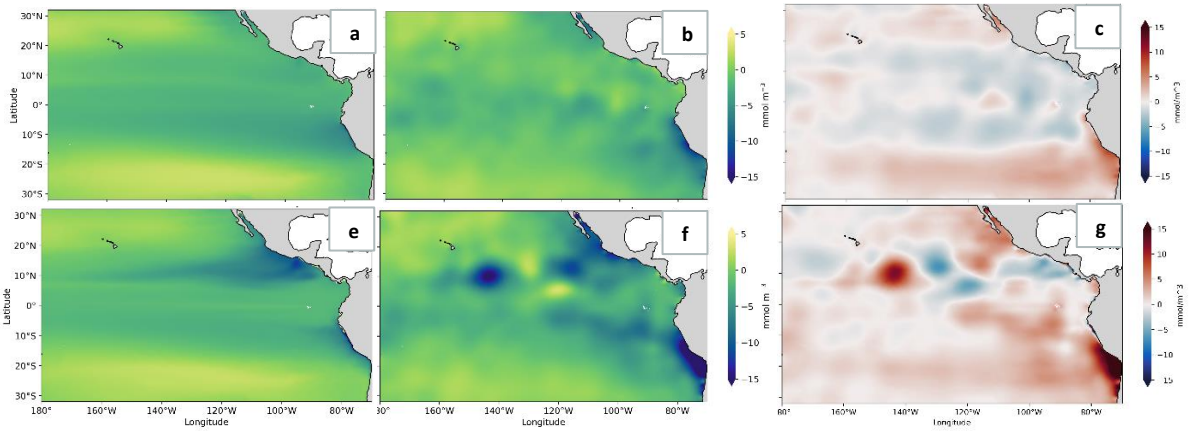

Figure 12. Mapped N* concentrations from model simulations (a, e), WOA2018 dataset (b, f), and anomalies (c, g), at the surface (a-c) and at 100m depth (e-g).

CHAPTER 3

Results

3.1 Spatiotemporal Variability of WCD and its Drivers

To understand the dynamics of WCD in the ETP, an initial characterization of the extent of the WCD variability in the spatial and temporal dimensions is performed. Subsequently, the underlying mechanisms driving WCD are identified, and their respective contributions to the observed WCD variability are analyzed.

3.1.1 WCD Variability in the ETP

The average WCD values presented in the previous chapter are representative of the mean state of WCD and reveal differences between the ETNP and ETSP. However, these values mask the substantial spatial and temporal variations that define the dynamics of WCD in the ETP. In both the ETNP and ETSP, the core WCD region displays large standard deviations in depth-integrated WCD rates (Figure 13a) and is surrounded by highly variable regions with up to 1000% changes in standard deviations relative to the mean (Figure 13b).

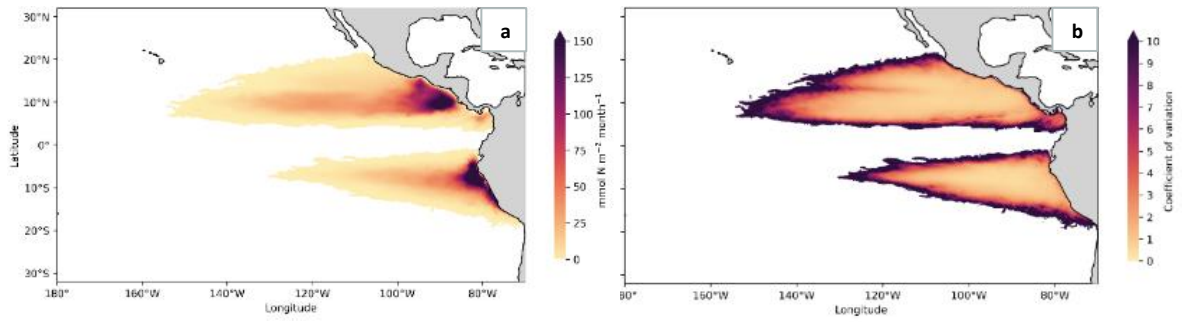

Figure 13. a) Mapped standard deviations of monthly depth-integrated WCD rates. b) Mapped variability coefficient of monthly depth-integrated WCD rates. The variability coefficient is calculated by dividing the standard deviation by the mean, and displays changes in WCD rates relative to the mean.

In the period from 1979 to 2019, the volume-integrated WCD rates over the ETP exhibit extensive variability, with fluctuations from monthly to decadal timescales. The monthly WCD rates over the ETP display fluctuations of up to 8.0 Tg N month^{-1} within a 7-month period. This constitutes intra-annual changes of twice the mean WCD rate (of 4.4 Tg N month^{-1}), illustrating the considerable variability of this process. As shown in the timeseries of the volume-integrated WCD rates over the ETNP and ETSP (Figure 14), analogous oscillations were recorded in the mean WCD rate, depth of the ODZ upper boundaries and ODZ volumes. Notably, the ETNP ODZ is nearly 40% larger than the ETSP ODZ (Table 2), however, the WCD rates are generally comparable for both regions (Figure 14a).

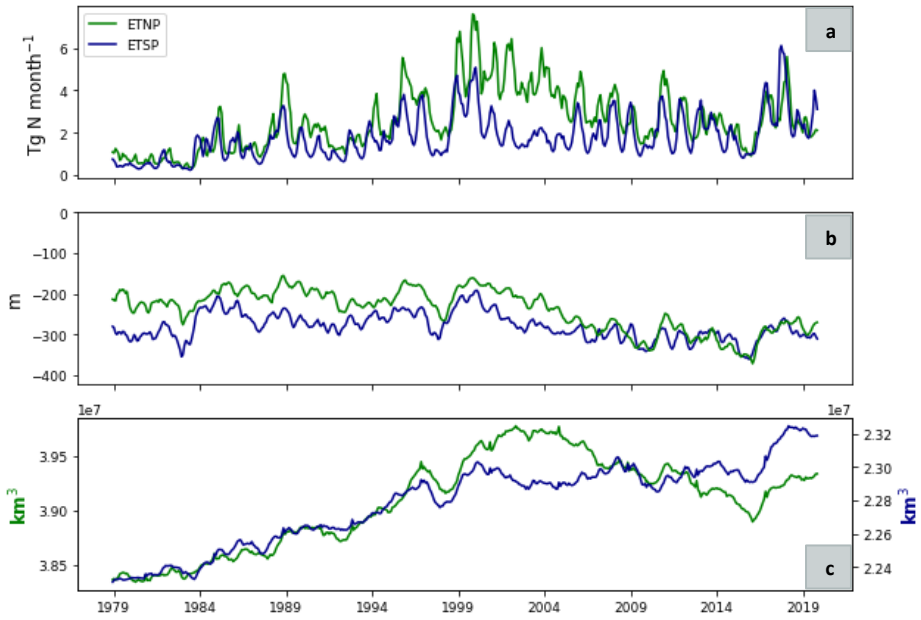

Figure 14. Timeseries of the monthly mean a) depth-integrated WCD rates, b) ODZ upper boundaries and c) ODZ volumes, for the ETNP (green) and ETSP (blue). Note the different y-axes for the ODZ volumes between the ETNP (left axis) and ETSP (right axis).

3.1.2 Drivers of WCD Variability in the ETP: The Horizontal Perspective

The maps in Figure 15 show the strong positive correlation between WCD and the ODZ thickness, ODZ upper boundaries and POC fluxes in the ETP, highlighting the critical role of the ODZs and POC export fluxes in driving WCD dynamics.

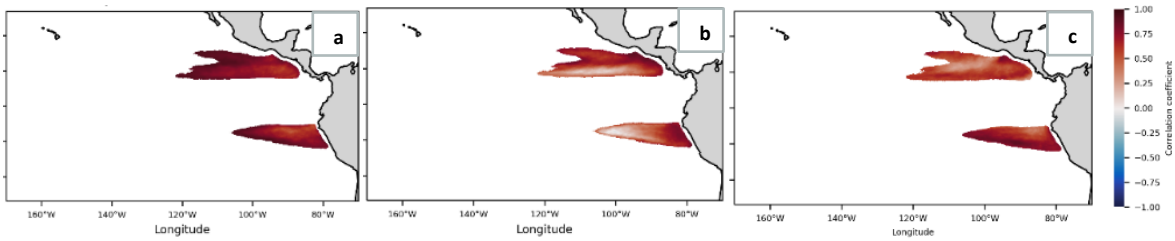

Figure 15. Maps of Spearman rank correlations between the monthly depth-averaged WCD rates and a) ODZ thickness, b) ODZ upper boundaries, and c) depth-averaged POC fluxes within the ODZ. Only locations where the ODZ was present at least 75% of the hindcast were plotted. All values plotted on the correlation maps are significant with $p < 0.05$.

To unravel the mechanisms driving the large fluctuations in WCD in the ETP, a comprehensive analysis of the drivers of WCD was performed in both the horizontal and vertical dimensions.

3.1.2.1 ODZ Variability

The first condition for WCD to occur is for the O_2 concentration to be low enough to induce the anaerobic remineralization of POC. Thus, changes in the distribution and extent of ODZs are a major factor driving variations in WCD. To assess potential differences in the contribution of the stable ODZ core to WCD as compared to the more variable ODZ edges, the volume-integrated and averaged WCD rates were plotted against the ODZ presence percentage (Figure 16). The latter variable reflects how many months of the hindcast the ODZ was present in a certain grid cell.

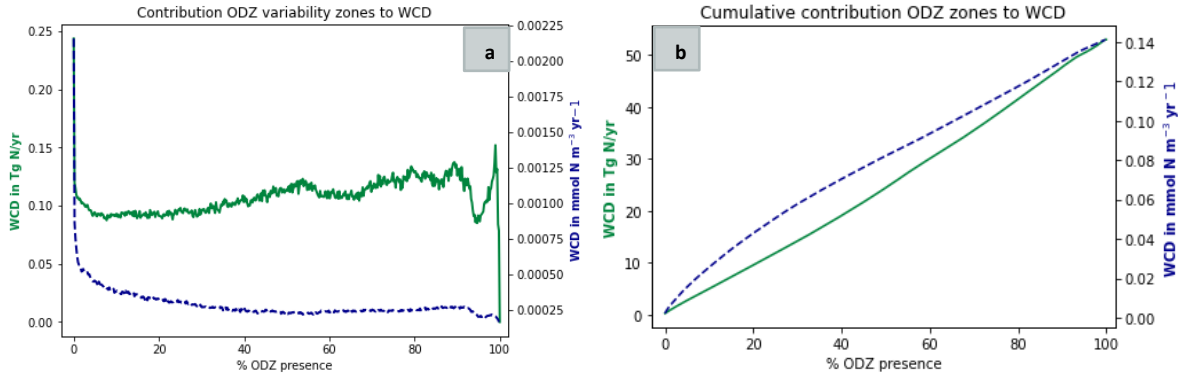

Figure 16. a) Contribution of the ODZ percentage presence zones (x-axis) to the volume-integrated annual WCD (y-axis in green) and volumetric annual WCD rates (y-axis in dashed blue). b) cumulative contribution of the ODZ percentage presence zones to WCD.

This analysis reveals that the highly variable regions (where the ODZ is only present during 0-5% of the 492 hindcast months) exhibit higher volumetric WCD rates (in dashed blue) than the stable regions, reaching a maximum WCD rate of ~0.0023 mmol N m^{-3} $year^{-1}$ (Figure 16a). In the regions where the ODZ is more frequently present, the WCD rates do not reach above 0.0005 mmol N m^{-3} $year^{-1}$. From this initial analysis it can be determined that the strongly variable regions with less than 5% presence during the hindcast display more than 5 times higher WCD rates per ODZ volume than the more stable regions. The volume-integrated WCD rates relate the contributions of the ODZ presence regions by taking into account their respective volumes. They increase gradually until approximately the 90% presence regions, where they reach a peak WCD rate of ~0.137 Tg N $year^{-1}$. This is followed by a steep decline down to ~0.085 Tg N $year^{-1}$, a strong spike at ~98% presence with rates up to ~0.150 Tg N $year^{-1}$, and subsequent return to low values of approximately 0.080 Tg N $year^{-1}$ at 100% ODZ presence regions. Despite the existence of regions with 100% presence throughout the hindcast, this region was negligibly small and does not contribute significantly to the overall denitrification. This analysis reveals that the WCD rates differ substantially depending on the temporal presence of the ODZ during the hindcast. Nevertheless, all regions contribute to a similar extent to the total WCD, as shown by the cumulative contribution of the ODZ presence regions to WCD, as shown in Figure 16b.

Distinctive patterns in the WCD rates were observed in the highly variable and the highly stable regions, notably on the two extremes of the spectrum (Figure 16). This elicited an analysis of the underlying mechanisms driving WCD in the different ODZ variability regions, which we achieved by discretizing the ODZ into separate regions of variability. The 'ODZ framework' explained in Section 2.3.2 separates the ODZ into regions of extremely high (ODZ0) and low variability (ODZ90), and the two regions in between (ODZ10 and ODZ50). This framework provides a novel perspective on the ODZ structure and allows for the identification and quantification of the mechanisms inducing changes in WCD in relation to the variability of the ODZs. To assess the relative contributions of each ODZ region to WCD, the total ODZ volumes over the hindcast and the annual volume-integrated WCD rates in the defined categories were quantified within the 3D ODZ variability regions (Table 3).

Table 3. Quantification of the average ODZ volumes, annual volume-integrated WCD rates, averaged volumetric WCD in the ODZs, and the % contributions for the four ODZ regions defined in Figure 5.

Acronym	**ODZ90**	**ODZ50**	**ODZ10**	**ODZ0**	**Total**
% presence	> 90%	90-50%	50-10%	<= 10%	-
Average ODZ volume (10^5 km^3)	1.69	7.50	6.53	1.01	16.73
% ODZ volume	10.1%	44.8%	39.0%	6.0%	100%
WCD rate (Tg N/yr)	5.39	23.17	19.46	4.75	52.78
% WCD rate	10.2%	43.9%	36.9%	9.0%	100%
Volumetric WCD rate (mmol N m^{-3} month^{-1})	0.186	0.168	0.164	0.203	0.170

The results indicate that the highly variable ODZ region (ODZ0) exhibits the highest mean volumetric WCD rate of the four ODZ regions. It displays a rate of 0.203 mmol N m^{-3} month^{-1}, 24% higher than the mean rate throughout the ETP ODZs of 0.164 mmol N m^{-3} month^{-1}. The ODZ0 contributes with an annual WCD rate of 4.75 Tg N year^{-1}, accounting for 9.0% of the total WCD, while the ODZ0 merely occupies 1.01×10^5 km^3, or 6.0% of the total ODZ volume in the ETP. The second highest mean volumetric WCD rate is encountered in the highly stable region (ODZ90) with a 13% higher rate than the mean. The ODZ90 contributes to the total WCD with a rate of 5.39 Tg N year^{-1} (10.2% of the total WCD), and with a volume of 1.69×10^5 km^3 (10.1% of the total ODZ volume). The strong difference in variability between the highly stable region (ODZ90) and the highly variable region (ODZ0) is visually represented in the timeseries in Figures 17a and 17d, respectively. While these regions give rise to a similar extent to the total WCD, their contributions over time are vastly different. Notably, the highly variable region (ODZ0, Figure 17d) displays strong peaks reaching maximal values of close to 3 Tg N year $^{-1}$, leading to significant episodic contributions to the total WCD rate. In comparison, the ODZ90 (Figure 17a) remains relatively stable and does not reach values of more than 1 Tg N year $^{-1}$ at any point in time during the hindcast. Despite their large differences in magnitude, the patterns of variability are similar across all four ODZ regions.

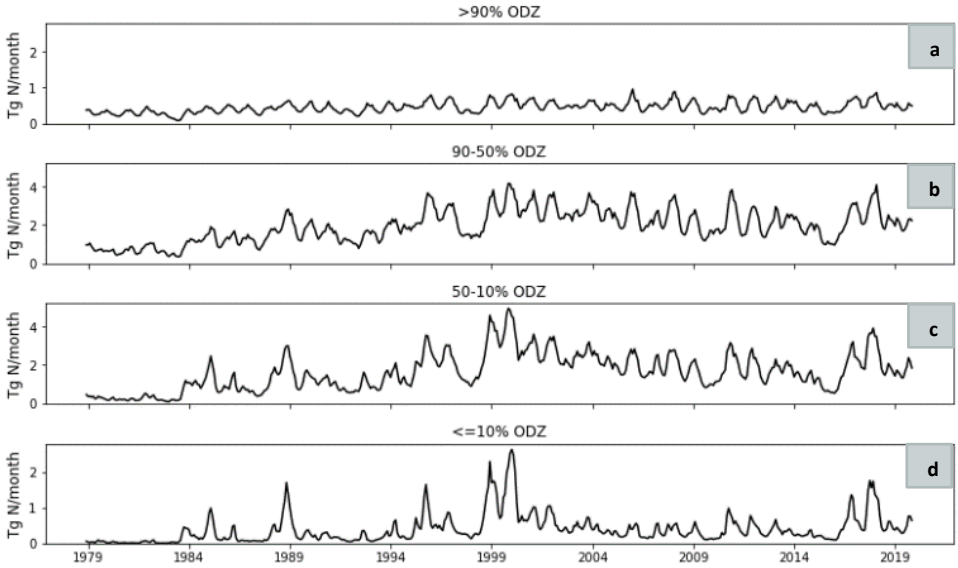

Figure 17. Timeseries of monthly spatially-integrated WCD rates in the ETP for the four defined ODZ regions. a) ODZ90, b) ODZ50, c) ODZ10, d) ODZ0. Note the difference in the scale of the y-axes between b-c, and a and d.

3.1.2.2 POC Flux Variability

The mean modelled POC flux at 100m depth over the region where WCD occurs in the ETP equals 370.31 mmol C m^{-2} $month^{-1}$ (Figure 11a). The mean POC flux is higher in the ETSP, with 438.01 mmol C m^{-2} $month^{-1}$, as compared to the ETNP with 329.66 mmol C m^{-2} $month^{-1}$. In addition to the analyses displayed in Table 3, the influence of the POC fluxes in each of the ODZ variability regions was quantified to be able to determine how the variability of the POC fluxes impacts WCD in conjunction with the ODZ variability. To this end, the fluxes occurring at 100m depth were averaged over the four 2D ODZ presence regions. This depth was chosen to represent the POC fluxes at the base of the euphotic zone. The values reported in Table 4 include ZONE50 and ZONE90. However, the ODZ50 and ODZ90 are not present at 100m depth, but only occur at greater depths. Hence, the quantified ZONE90 and ZONE50 POC fluxes in Table 4 represent the POC fluxes above the ODZ90 and ODZ50 variability regions, which will eventually reach the respective regions at deeper depths through the downward transport of POC. The results of this analysis revealed that the highly stable region (ZONE90) exhibited a considerably higher average POC flux than the more variable regions, with a POC flux of 459.20 mmol C m^{-2} $month^{-1}$, 23% higher than the mean. The outer region (ZONE0) had the lowest average POC flux at 100m depth, with 339.03 mmol C m^{-2} $month^{-1}$.

Table 4. Average POC fluxes at 100m depth for the four delineated 2D ODZ presence regions and the entire ODZ.

Acronym	**ZONE90**	**ZONE50**	**ZONE10**	**ZONE0**	**Total ODZ**
% presence	> 90%	90-50%	50-10%	<= 10%	-
POC fluxes (mmol C m^{-2} $month^{-1}$)	459.20	379.23	357.84	339.03	374.28

The spatial distribution of the standard deviations of POC fluxes throughout the hindcast illustrates which regions are more strongly impacted by variability, and to what magnitude (Figure 18a). As shown, the mean POC fluxes at 100m depth are highest in the eastern part of the ODZ close to the coast, with deviations of more than 500 mmol C m^{-2} $month^{-1}$, consistent with where the highest WCD rates are observed (Figure 5). The ODZ regions to the west of the ODZ core experience standard deviations of between 0 and 100 mmol C m^{-2} $month^{-1}$ (Figure 18a). The mapped variability coefficients at 100m depth (Figure 18b) show a similar pattern to the standard deviations, with the eastern regions of the ODZs displaying changes in the standard deviations of more than 75% relative to the mean. Together, these maps highlight the substantial variability of POC fluxes in the ETP.

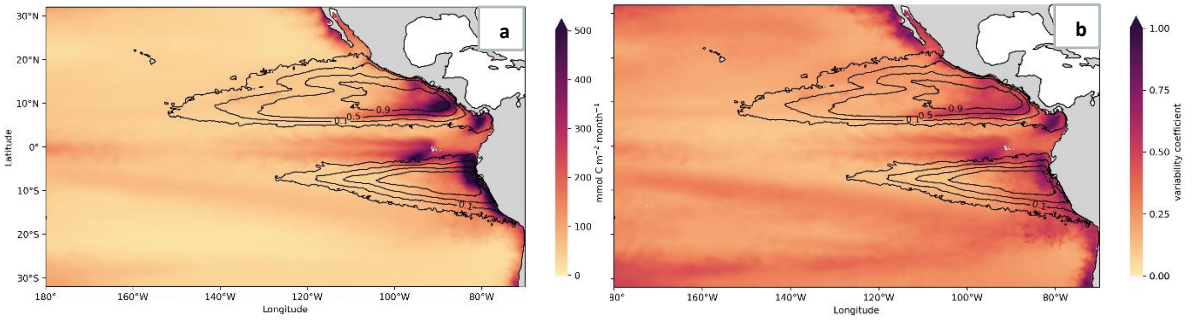

Figure 18. Maps of the standard deviations a) and variability coefficients b) of the POC fluxes at 100m depth in the ETP with the 2D ODZ region contours.

The POC timeseries in Figure 19 reveal the spatially-averaged temporal pattern of variability in all the ODZ zones, and display strong intra- and interannual fluctuations. POC flux variability occurs on

shorter timescales compared to variability in the ODZ volume (Figure 17). The highly stable region (ZONE90), when compared to the regions with higher variability, exhibits pronounced peaks indicating strong changes in POC fluxes on intra-annual timescales (Figure 19a). These fluctuations range from approximately 300 mmol C m^{-2} $month^{-1}$ to as high as 800 mmol C m^{-2} $month^{-1}$, representing a more than twofold increase in POC fluxes. This result reiterates that not solely the average POC flux at 100m is the highest in this region, but moreover its variability. The ZONE0 region shows the smallest variability in POC fluxes, which do not exceed fluctuations between 200 and 500 mmol C m^{-2} $month^{-1}$ at any timepoint in the timeseries (Figure 19d). This is in contrast to the findings in the WCD rates, which showed the strongest fluctuations in the ODZ0 3D region (Figure 17d), while the POC fluxes show the highest fluctuations in the ZONE90 region.

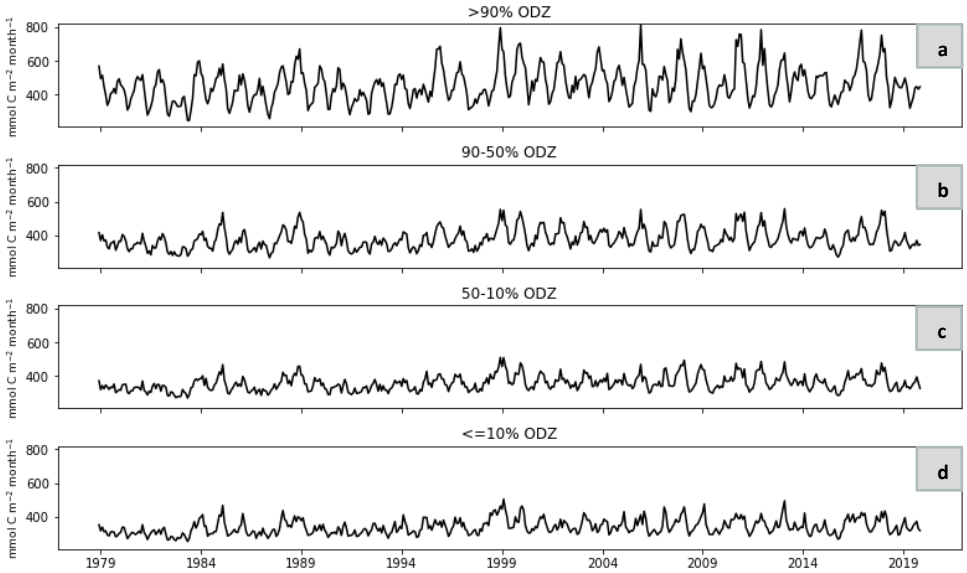

Figure 19. Timeseries of spatially averaged monthly POC fluxes at 100m depth in the 2D ODZ variability regions a) ZONE90, b) ZONE50, c) ZONE10, d) ZONE0.

3.1.3 Drivers of WCD in the ETP: The Vertical Perspective

The interplay between the WCD drivers is strongly dependent on their distributions in depth. Thus, to understand their combined effects driving WCD, the processes were characterized in the vertical dimension. To this end, the mean vertical profiles for the four 2D ODZ variability zones (delineated in Figure 5) were plotted for all drivers of WCD, as well as variables impacted by WCD for the ETNP and ETSP separately. Since these vertical profiles were calculated by averaging horizontally over the 2D ODZ zones (ZONE90 to ZONE0), each zone being determined by the maximum percentage presence of grid cells in the water column at each location, they also incorporate ODZ regions of lower variability. As a result, Figures 20-23 demonstrate that each zone encompasses its 3D ODZ and the 3D ODZs characterized by lower variability. It is important to note that the ODZ areas (Panels b and i) and yellow bars in Figures 20-23 reflect the most extreme extents where the respective 3D ODZs occur at least once during the entire hindcast. As such, they depict between which depths each 3D ODZ region can be found and not the mean extent of that ODZ. When discussing the 3D ODZ upper boundaries and thickness we therefore refer to the maximal extents.

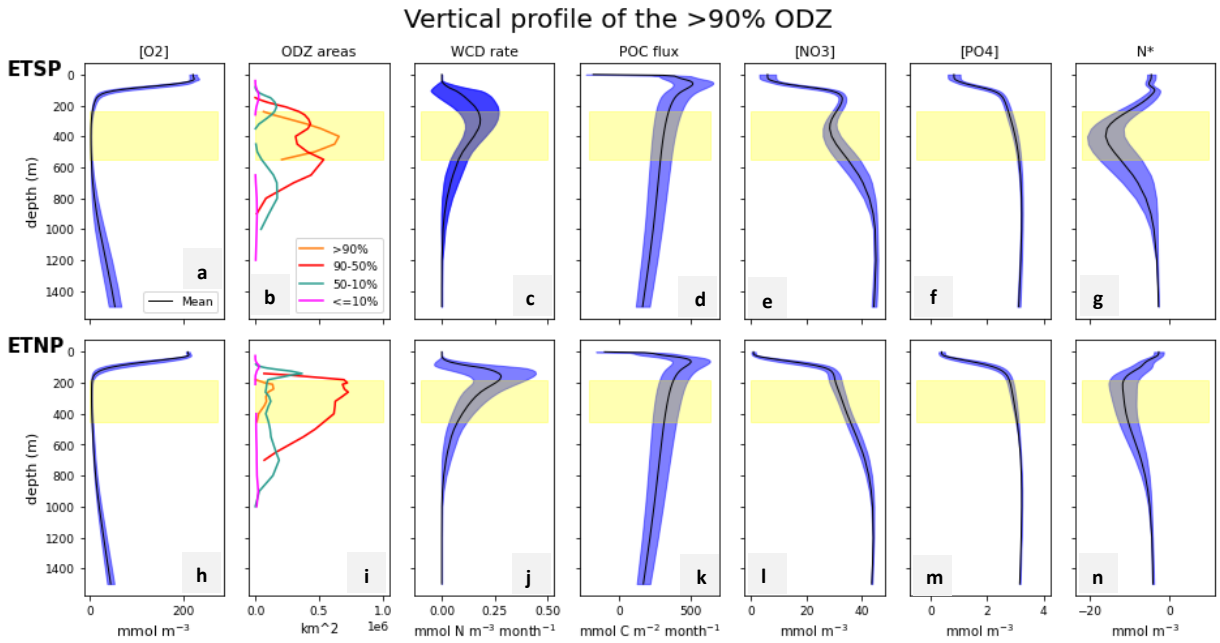

Figure 20. Vertical profiles of the mean distribution of the drivers and impacts of WCD for the 2D ZONE90 presence region, for the ETSP (a-g) and ETNP (h-n) separately. Blue shading around the black mean line indicates the standard deviations. Yellow horizontal bands indicate the furthest vertical extent of the 3D ODZ90 region during the entire hindcast. Panels b and i indicate the total time-integrated ODZ areas of each of the defined 3D regions at depth throughout the entire hindcast.

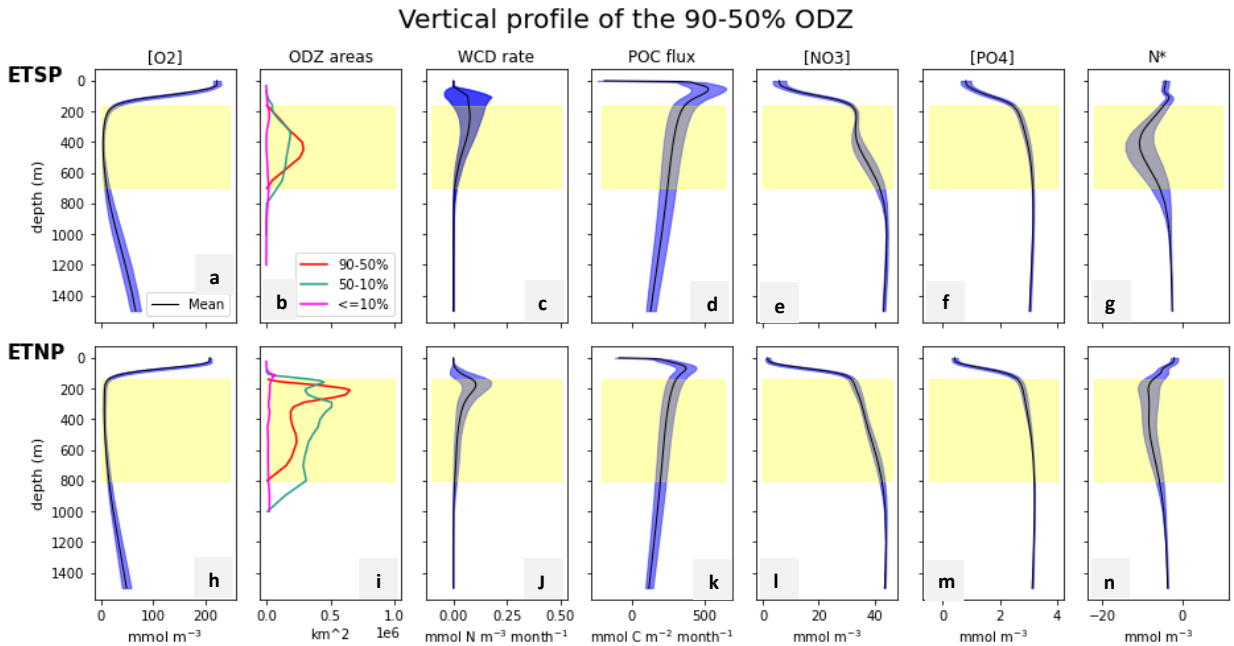

Figure 21. Idem as Figure 20, but for ZONE50 and ODZ50.

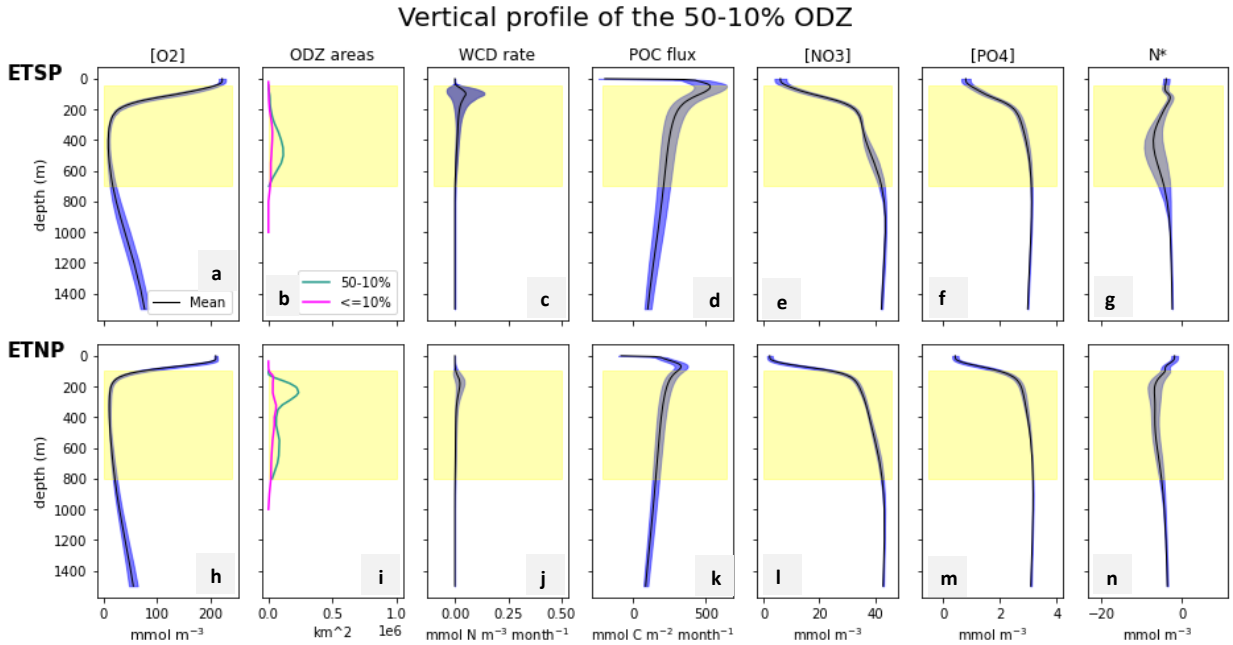

Figure 22. Idem as Figure 20, but for ZONE10 and ODZ10.

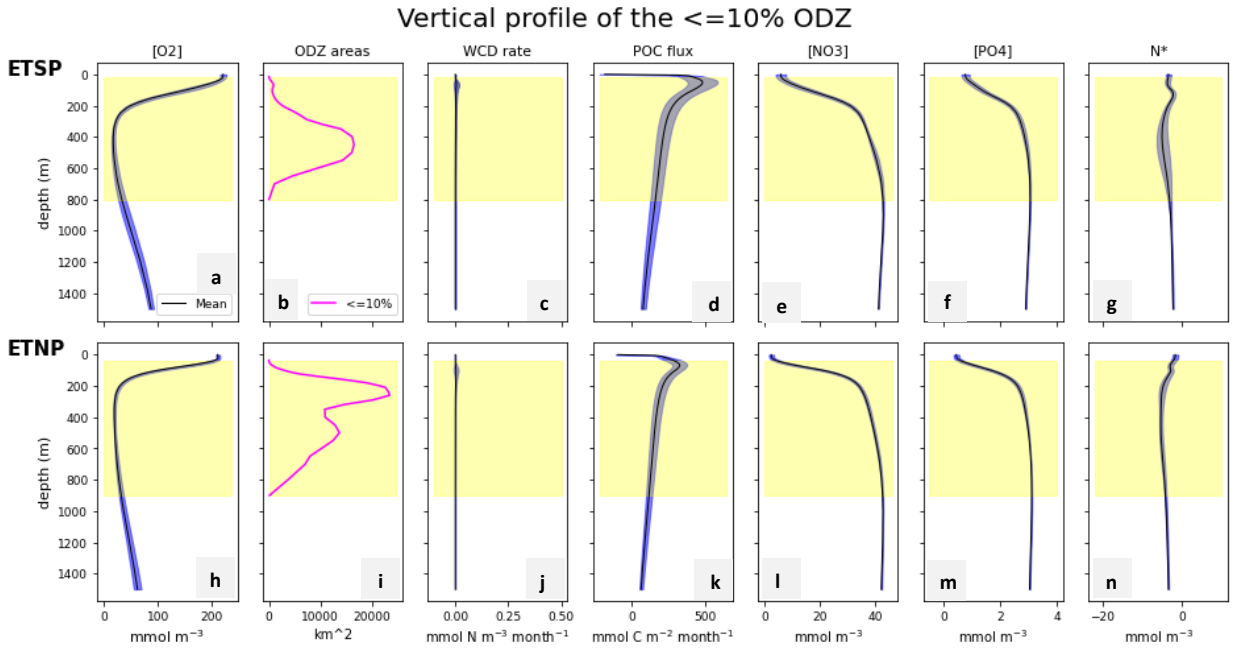

Figure 23. Idem as Figure 20, but for ZONE50 and ODZ50. Note the difference in the x-axis scale for the ODZ area plot between this figure and Figures 20-22 above.

Overall, in all the 2D ODZ zones, the mean O_2 concentrations show characteristics distribution in depth, with high O_2 concentrations near the sea surface due to ventilation, and a strong reduction down to ~200m, where the O_2 concentrations reach a minimum (Figures 20-23 Panels a and h). In all the 2D zones, the ODZs reach near the surface (Figures 20-23 Panels b and i). At the most upper part of the ODZs, reaching from close to the surface down to ~50m depth, the O_2 concentrations solely fall below 3mmol O_2 m^{-3} for less than 10% of the time, as indicated by the presence of the ODZ0 (in pink). The same applies to the lower boundaries of the ODZs. The ODZ0 has a maximum thickness of nearly 1200m in the ETSP and 1000m in the ETNP, the largest of all ODZs (as seen in Figure 20 Panels b and i in pink). The deepest extent of the ODZs is thus reached in ZONE90 by the ODZ0 up to 1200m depth in the ETSP and 1000m depth in the ETNP. In contrast to the large vertical extent of the 3D ODZ0

region, the highly stable ODZ90, where O_2 concentrations are less than 3mmol O_2 m^{-3} for more than 90% of the hindcast, is confined from ~ 225m to ~550m depth in the ETSP and from ~ 200m to ~450m depth in the ETNP, with a maximum thickness of ~ 325m and ~250m, respectively (yellow bands in Figure 20). The ODZ thicknesses and extents in depth are larger with the increasing variability of the ODZ regions. In fact, all 3D ODZ regions are surrounded above and below by regions of increasing variability (Figures 20-23, Panels b and i). In terms of the sizes of the ODZs at depth, the ODZ90 depicts a considerable size difference between the ETSP and ETNP, as it reaches a maximum area at 400m depth in the ETSP where it covers ~0.65×10^6 km^2, while the maximum extent in the ETNP spans only ~0.2×10^6 km^2 at ~220m depth (Figure 20, Panels b and i).

The WCD maxima for all ODZ regions occur at the upper boundaries of the ODZs (indicated by the yellow bands), and decrease rapidly with depth (Panels c and j Figures 20-23). In ZONE90 (Figure 20), the WCD maxima lie at approximately 200m depth in the ETNP and 300m depth in the ETSP. As the regions become more variable, the WCD maxima become increasingly shallower. For instance, in ZONE10 (Figure 22), the WCD maxima reach 200m in the ETNP and 100m in the ETSP. These profiles furthermore highlight how the highly variable regions (ZONE0, Figure 23 and ZONE10, Figure 22) have shallower WCD maxima in the ETSP (Panel c) than in the ETNP (Panel j). This is in contrast to the highly stable ZONE90, where the ETNP shows a shallower WCD maximum than the ETSP (Panels j and c, respectively, Figure 20).

In general, the spatially-averaged POC fluxes are the highest in the top 200 meters (Panels d and k). The POC maxima occur between 50 and 100m depth, followed by a steep decline down to ~150m depth, and thereafter a steady attenuation with depth. In terms of the magnitude of the POC fluxes, the ETSP shows higher maxima (~500 mmol C m^{-2} $month^{-1}$, Panel d) than the ETNP (~300 mmol C m^{-2} $month^{-1}$, Panel k) in all regions except the most stable region (ZONE90, Figure 20), where they are comparable with ~500 mmol C m^{-2} $month^{-1}$. In ZONE0 the ODZ0 reaches close to the sea surface (indicated by the yellow band) and fully encompasses the POC maxima (Figure 23 Panels d and k). In the more stable regions (Figures 20-22), the WCD maxima are located right below the POC maxima, at the upper boundaries of the ODZs.

Figures 20-23 provide an insightful depiction of the distribution of the different drivers in depth. However, as the vertical profiles are averaged over the 2D regions that include regions where, during the 41-year hindcast, the ODZ is momentarily not present, or where multiple 3D ODZ variability regions overlap, the absolute values are not as representative of the processes occurring within each ODZ. As such, it is important to take into account that this figure gives accurate representations of the distribution of the variables in the vertical dimension but is not well suited to quantify the processes at each depth. The ODZ areas (Panels b and i) are an exception to this, as these values were not averaged, but show the total time- and spatially-integrated areas of the 3D ODZs during the entire hindcast.

3.1.3.1 ODZ and POC Flux Variability

Having established the vertical distribution of the drivers, the subsequent objective is to investigate their dynamics over time and to illustrate their temporal response to climatic variability. Furthermore, in the temporal dimension, the WCD drivers are impacted to different extents in each ODZ variability region (Figure 19). To elucidate how the WCD drivers interplay over time, an in-depth analysis of the WCD variability at five distinct locations in the ETP ODZs was performed, shown in Figure 24. Figure 24 shows the POC fluxes at the top of the ODZs (top panel), the Hovmöller plots of the WCD rates and ODZ contours in depth (middle panel), and the N* concentrations as the top of the ODZs (bottom panel) throughout the hindcast at the five locations. The five locations were chosen to represent the different

ODZ variability regions that arise in the ETP (indicated in the map in Figure 5). Two locations are located in the ETNP, one in ZONE90 (Panel d), and a second one in ZONE50 (Panel b). Another three locations depict the dynamics occurring in ZONE90 (Panel a), ZONE50 (Panel e), and ZONE10 (Panel c) in the ETSP. No locations were selected in ZONE0, as the ODZ occurrence is extremely short and therefore did not bring additional information on the processes driving WCD. To evaluate if the five selected point locations are representative of their respective regions, as well as the extent and direction of any bias, we analyzed the depth- and time-average WCD rates for each point location and their 2D ODZ zone (Figure C1 Appendix C). The findings indicate an overall agreement between the chosen points and their respective zones. However, we observed that Point A and Point D, both situated within ZONE90, were skewed towards higher WCD rates compared to the average rates within their zones.

Figure 24 depicts strong WCD and ODZ variability in the vertical dimension in all locations, with fluctuations of up to hundreds of meters in the timespan of months. The depth-resolved ODZs at these individual point locations further reiterate that the ODZ is structured as a stable core in the center, with regions of increasing variability at the outer boundaries of the ODZ (seen on the coloured bars in the middle plots indicating the ODZ percentage presence).

WCD is concentrated at the top of the ODZ, where there is a higher influx of POC, and diminishes in depth. Hence, when the upper boundaries of the ODZ shoal, the WCD rates increase, as the ODZ encounters higher POC fluxes at shallower depths. In addition, there is a concurrent shoaling of the ODZ upper boundaries and increase in POC fluxes, most clearly visible in the stable regions in points A and D. To determine whether the observed positive correlation between POC fluxes and the shoaling of the upper boundaries of the ODZs is a widespread phenomenon within the ODZs and a determining factor in enhancing WCD, the POC fluxes at 100m depth were correlated with the ODZ upper boundaries (Figure 25). In general, the two variables exhibit positive correlations across the ODZ, particularly in the ODZ cores, where the most pronounced instances of WCD were observed (Figure 5).

The point location in ZONE90 in the ETSP (A) reaches maximal WCD rates of up to ~8 mmol N m^{-3} $month^{-1}$, while in the ETNP (D) the WCD rates only reach up to ~4.6 mmol N m^{-3} $month^{-1}$. In ZONE50, the WCD rates reach 0.39 mmol N m^{-3} $month^{-1}$ in the ETSP (E), and are higher in the ETNP with 1.67 mmol N m^{-3} $month^{-1}$ (B). The point location in ZONE10 in the ETSP (C) shows maximal WCD rates of 0.14 mmol N m^{-3} $month^{-1}$.

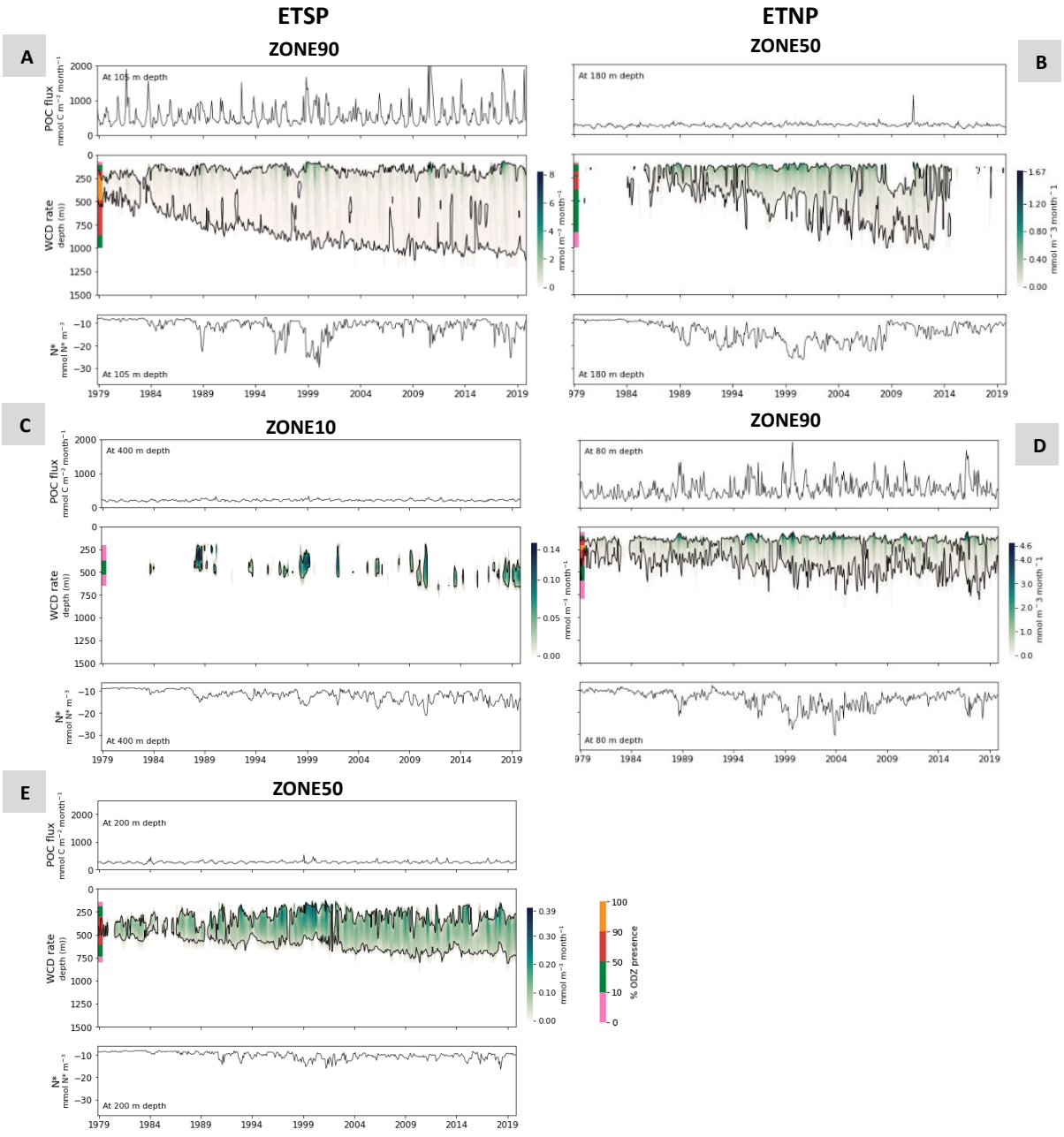

Figure 24. Hovmöller plots of the WCD rates at the five locations (A-E). Note the different ranges for the colour bars depicting the WCD rates at each location. Contours indicate the 3 mmol m^{-3} O_2 isopleth. Colored bars on the y-axis of the Hovmöller plots indicate the ODZ percentage presence at each depth. For each panel, the top plot shows the POC fluxes at the top of the ODZ. The bottom plot shows N* concentrations at the top of the ODZ.

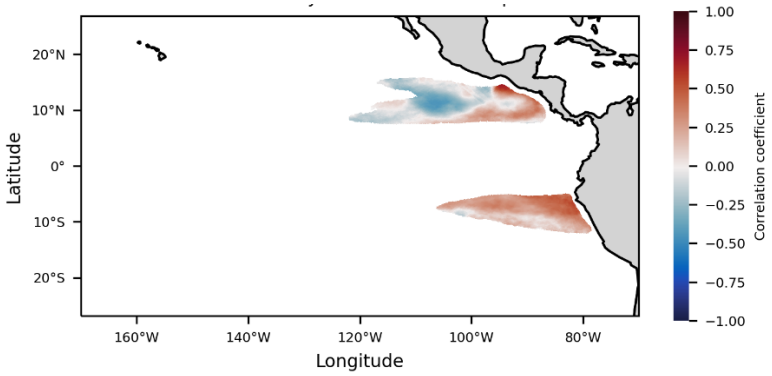

Figure 25. Mapped correlations between the POC fluxes at 100m depth and the upper boundaries of the ODZs. Only locations where the ODZ is present at least 75% of the time are plotted. All values plotted on the correlation maps are significant, $p < 0.05$.

Having established the significance of the POC fluxes and the ODZs as drivers of WCD, and having demonstrated the pronounced intra-annual to decadal variability of WCD, the focus now shifts to the analysis of how these drivers are impacted by climatic forcing across different timescales, and the consequential influence on WCD in the ETP.

3.2 Climate-Forced Dynamics of WCD Variability in the ETP

WCD is subject to a broad range of processes that contribute to its variability, from oceanic internal variability (e.g. eddies) to longer-term climate-forced variability. This study focuses on three primary climatic modes of variability in the ETP that significantly impact the fluctuations in WCD rates. The ETP is subject to large-scale variability, predominantly introduced by ENSO (Rasmusson and Wallace, 1983) and PDO (Mantua et al., 1997), and to a smaller degree by the seasonal cycle. These three phenomena have extensive consequences on the ODZ distribution, biological production and ultimately WCD in the ETP. The following chapter addresses which mechanisms, and to what extent, the atmospheric and oceanic changes induced by the main climatic modes of variability in the ETP influence WCD.

3.2.1 Seasonal Dynamics of WCD

Firstly, the smaller mode of variability in the Pacific Ocean is described, namely the seasonal cycle. For simplicity, this section refers to boreal seasons. In the ETSP, the highest WCD rates occur in winter, with an increase of 25.7% as compared to the mean volume-integrated WCD rate, and an average volumetric WCD rate of 0.210 mmol N m^{-3} $month^{-1}$. In the ETNP, the WCD rates are the highest in spring, with an increase of 19.0% and an average rate of 0.193 mmol N m^{-3} $month^{-1}$. The volumetric WCD rates in Table 5 reflect the spatially-averaged WCD rates within the ODZ, where an ODZ is present at each point in time, and show the same patterns as the volume-integrated WCD rates. For both the ETSP and ETNP, the lowest WCD rates are recorded in summer, with a decrease of 28.0% and 17.7% to the mean volume-integrated WCD rate, respectively. The ETSP shows a stronger seasonality than the ETNP, with stronger changes in the volume-integrated WCD rate between seasons.

Table 5. Average ODZ volumes, monthly volumetric WCD rates within the ODZ, and volume-integrated annual WCD rates for the four seasons, for the ETSP and ETNP separately.

		Mean	**DJF**	**MAM**	**JJA**	**SON**
	Boreal seasons		Winter	Spring	Summer	Autumn
ETSP	ODZ volume (10^5 km^3)	7.000	6.990	7.069	7.011	6.929
	Volumetric WCD rate (mmol N/m^3/month)	0.175	0.210	0.157	0.119	0.174
	Volume-integrated WCD rate (Tg N/year)	21.8	27.4	20.9	15.7	23.2
ETNP	ODZ volume (10^5 km^3)	9.729	9.710	9.645	9.772	9.787
	Volumetric WCD rate (mmol N/m^3/month)	0.159	0.172	0.193	0.136	0.151
	Volume-integrated WCD rate (Tg N/year)	31.1	33.6	37.0	25.6	28.3

The seasonal response of WCD relative to the mean is not uniform and shows clear zonal differences (Figure 26). The horizontal extents of the WCD and the ODZs (Figure 26) are not affected by seasonality. The outer boundaries of the ODZ show minor to no differences with the mean WCD rates, while the ODZ cores show strong differences in WCD rates throughout the seasons as compared to the mean state. The Costa Rica Dome, located at its mean position at approximately 9°N 90°W (Fiedler, 2002), displays differing seasonal responses in WCD rates. During autumn and winter, the WCD rates in this region decrease by up to 40 mmol N m^{-2} month^{-1} as compared to the mean, with increased WCD rates of more than 40 mmol N m^{-2} month^{-1} during spring. In the ETSP ODZ, WCD rates show a strong increase during autumn and winter along the Peruvian coast with WCD rates of more than 40 mmol N m^{-2} month^{-1}. While in autumn the strong positive anomalies are concentrated in the ODZ core between 80°W and 85°W, in winter the anomalies spread up to 110°W. In summer, WCD rates are strongly diminished as compared to the mean throughout both ODZs.

As shown in Table 5, the ODZs are present throughout all seasons and retain relatively stable volumes, for both the ETSP and ETNP, with average ODZ volumes of 7.000 10^5 km^3 and 9.729 10^5 km^3, respectively. The ODZ thickness seasonal anomalies plot does not exhibit a uniform response throughout any of the regions (Figure 27). The seasonal anomalies to the mean ODZ upper boundaries are minor and furthermore display some level of stochasticity, most notably in the ETSP ODZ and during winter in the ETNP ODZ. In the Costa Rica Dome, ODZ upper boundaries shoal during spring by approximately 25 to 50m, while they deepen during winter by up to 25m.

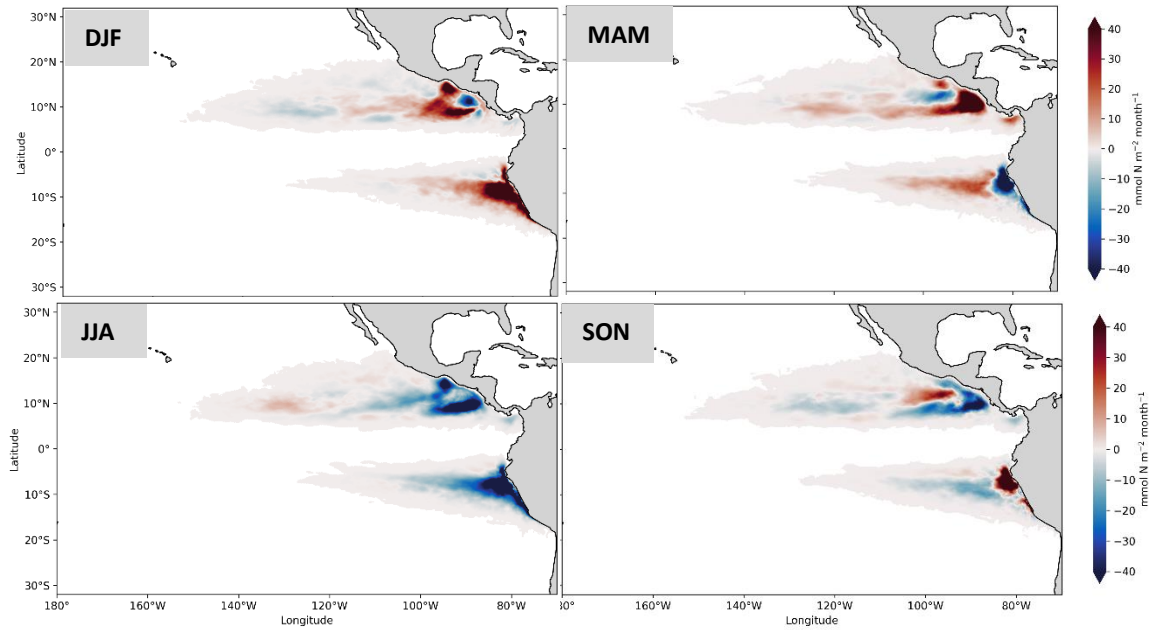

Figure 26. Climatological seasonal anomalies of the depth-integrated WCD rate. The seasonal anomalies are computed relative to the annual mean. DJF: December-February, MAM: March-May, JJA: June-August, SON: September-November.

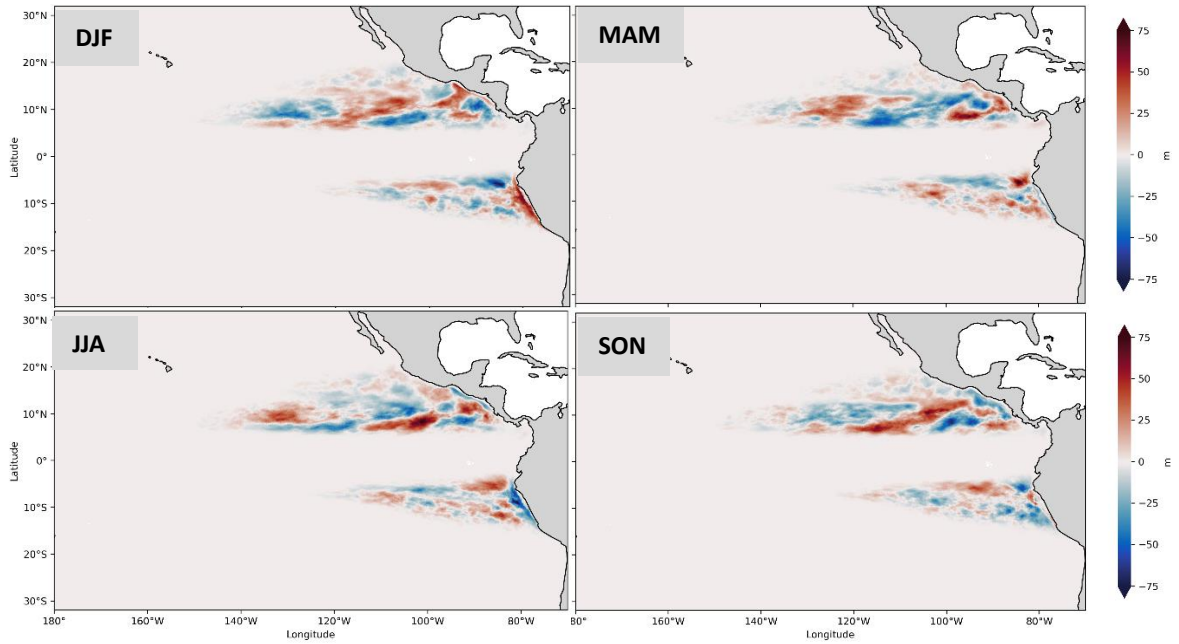

Figure 27. Mapped seasonal anomalies to the mean ODZ thickness for the four seasons.

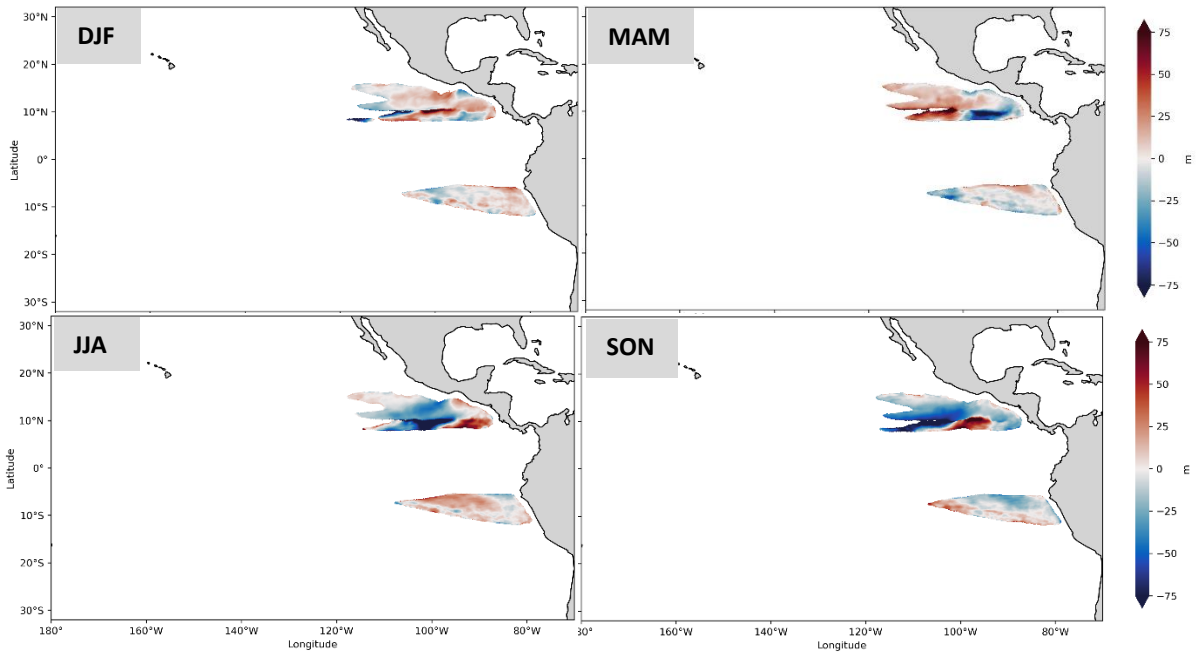

Figure 28. Mapped seasonal anomalies to the mean ODZ upper boundaries for the four seasons.

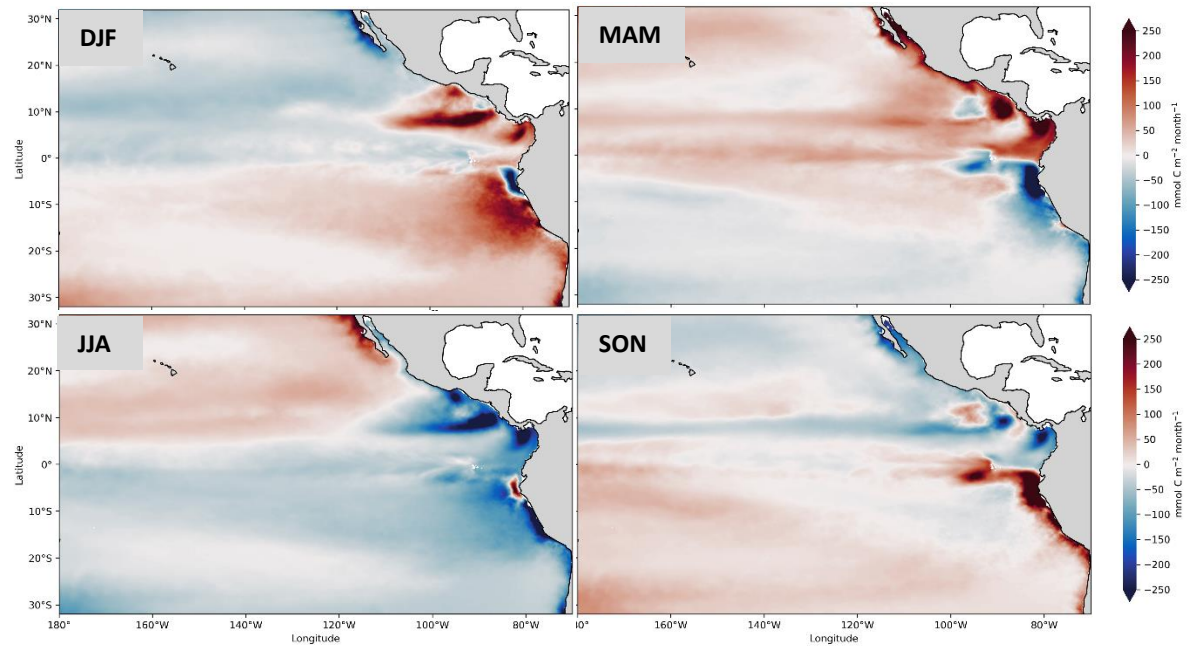

Figure 29. Mapped seasonal anomalies to the mean POC flux at 100m depth for the four seasons.

The mean POC fluxes at 100m depth reveal symmetrical responses between the ETNP and ETSP during the different seasons (Figure 29). In spring and summer, the ETNP displays increased POC fluxes in the open ocean of ~50 mmol C m^{-2} $month^{-1}$ relative to the mean, with stronger POC fluxes along the equator at ~0°N and ~10°N. The inverse is observed during autumn and winter, with anomalously low POC fluxes along the ~10°N longitude in autumn. Notably, within the ETNP ODZ, the POC fluxes show a different pattern than the rest of the ETNP, as they strongly increase during winter and spring with anomalies of more than 250 mmol C m^{-2} $month^{-1}$, and decrease to a similar magnitude during spring and autumn. Moreover, the Costa Rica Dome shows a contrasting response as compared to its immediate surrounding regions in the ODZ, with the clearest differences visualized during spring and autumn where POC fluxes decrease and increase, respectively, with ~50 mmol C m^{-2} $month^{-1}$. The ETSP

displays the opposite response to the ETNP, with increased POC fluxes in the autumn and winter months, most notably within the ODZ along the Peruvian coast and up to 100°W during winter.

To characterize the seasonal response of WCD denitrification in depth, the monthly climatologies in the ETNP and ETSP were plotted between sea surface and 800m depth, shown in Figure 30. In both the ETNP and ETSP, WCD rates were highest between approximately October and May, with a decrease in the summer months. The mean WCD rates do not exhibit major fluctuations in the depth dimension throughout the different seasons, and as previously shown in Figures 20-23, are concentrated between ~50-800m depth.

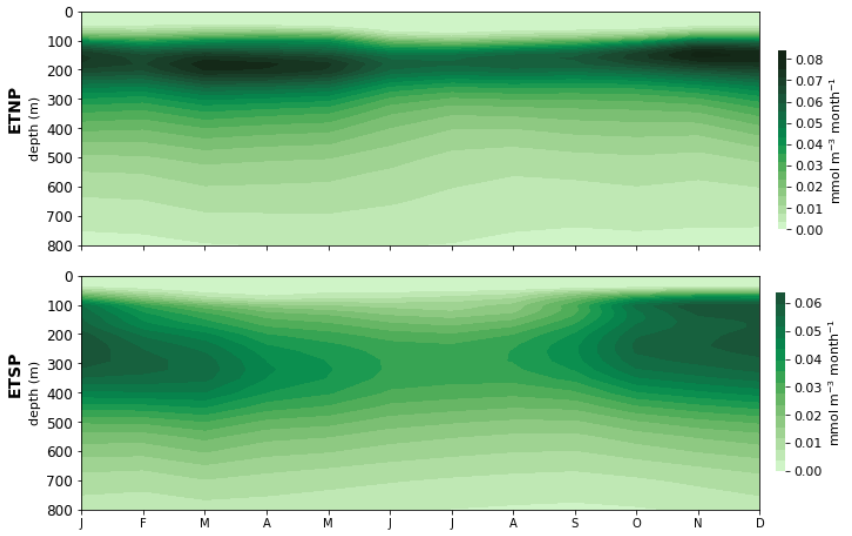

Figure 30. Spatially-averaged depth-resolved monthly climatologies of mean WCD rates within the WCD regions between sea surface and 800m depth, for the ETNP and ETSP separately.

While the seasonal cycle induces differing responses in WCD, since the ETP ODZs are located close to the equator, the seasonal cycle is not very pronounced. In the Tropical Pacific, two other modes of climatic forcing dominate the variability, namely ENSO and the PDO. These will be discussed next.

3.2.2 Dominant Modes of WCD Variability in the ETP

The simulation shows that 54% of the interannual variability in WCD rates in the ETP can be described by ENSO (Figure 31), thereby establishing ENSO as one of the dominant modes of variability controlling WCD in the ETP. La Niña episodes show increased WCD rates, reaching peaks up to 2.5×10^{-3} mmol m^{-3} $month^{-1}$, while during El Niño phases the WCD rates decrease, reaching minimal monthly averages of close to 0 mmol m^{-3} $month^{-1}$.

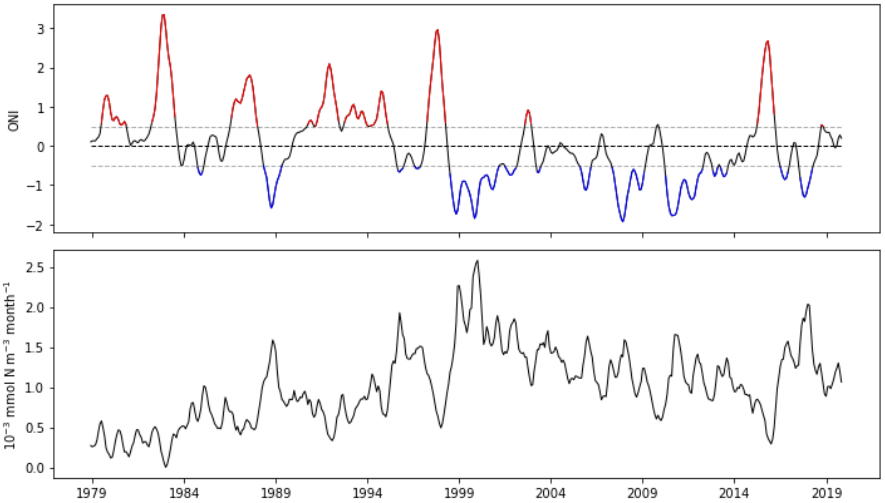

Figure 31. Timeseries of the ONI from the El Niño 3.4 SST anomalies (top) and detrended and deseasonalized WCD rates (bottom). El Niño episodes are shown in red and La Niña episodes are shown in blue. The Spearman rank correlation between ONI and WCD rates coefficient equals -0.737 with $p < 0.01$.

On decadal timescales, 15.7% of the variability in WCD rates can be explained by the PDO (Figure 32). PDO induces higher WCD rates during negative (cold) PDO phases, and lower WCD rates during positive (warm) PDO phases.

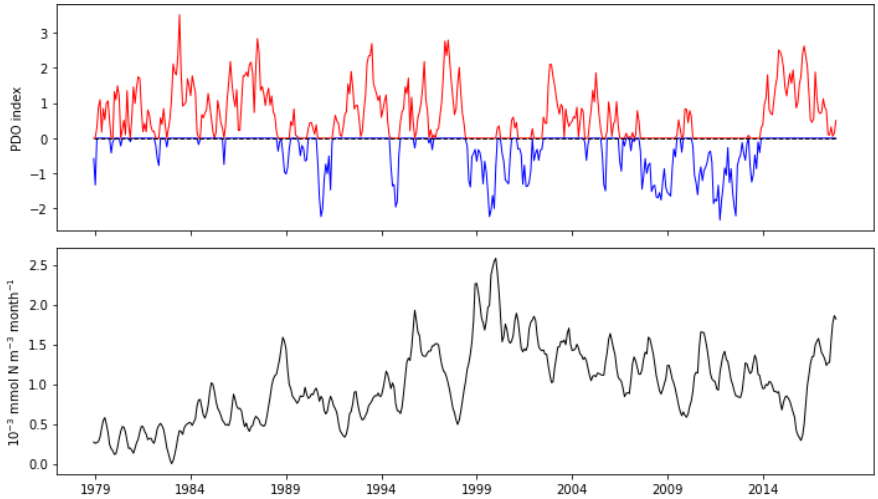

Figure 32. Timeseries of the PDO index by Mantua et al. (2002) from 1979 to 2017 (top) and of the deseasonalized WCD rates (bottom). Positive (warm) PDO phases are shown in red and negative (cold) PDO phases are shown in blue. The Spearman rank correlation coefficient between the PDO index and WCD rates equals -0.396 with $p < 0.01$.

To understand how the individual mechanisms enhancing WCD are affected by ENSO and the PDO, the impact of the climatic forcings on the drivers of WCD in each ODZ region was analyzed. To this end, the ONI and PDO index were correlated with changes in WCD rates, ODZ volumes, and POC fluxes in the defined ODZ regions, shown in Figure 33.

ENSO and WCD exhibit strong negative correlations (Figure 33), with the most pronounced correlations observed in the highly stable ODZ90 and ODZ50 of -0.72 and -0.73, respectively. The variable ODZ10 and ODZ0 display relatively more modest correlations of -0.6 and -0.48, respectively. This indicates that WCD increases during negative La Niña events and decreases during positive El Niño events. The correlation of ONI with the ODZ volumes shows moderate correlations for all regions,

with the weakest correlation of -0.27 in the highly stable ODZ90 region. The influence of ENSO on the POC flux is relatively uniform for the four ODZ regions, with gradually stronger correlations from -0.67 for the ODZ90 up to -0.72 for the ODZ0. The ODZ upper boundaries show a strong correlations with ONI in the ODZ90, however, for the other regions the correlations is extremely weak or insignificant (in grey). Overall, the impact of ENSO on WCD and POC is more pronounced than on the ODZ volume.

Correlation analysis for the PDO shows similar influences as observed for ENSO, but to a smaller extent. WCD rates are negatively correlated to the PDO index, and the correlations increase in strength from -0.19 for the ODZ0 up to -0.42 for the ODZ90. The PDO index and ODZ volumes show weak correlations ranging between -0.20 for the ODZ90 to -0.33 for the ODZ10. As for ENSO, the POC flux response is uniform over the four regions with correlations of -0.36 for ODZ90 to -0.33 for ODZ0. Similarly, the ODZ upper boundaries solely show a significant negative correlation for the ODZ90 of -0.24, while the other regions show insignificant correlations. As the 1979-2019 hindcast is too short for a robust analysis of the changes induced on decadal timescales in detail, we limit the further analysis to the influence of climatic forcing on the drivers of WCD to ENSO and seasonal cycle.

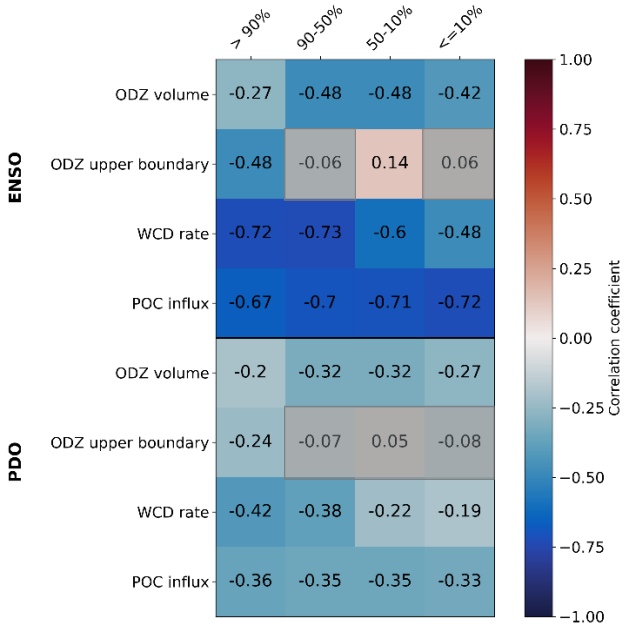

Figure 33. Heat map showing the Spearman rank correlation coefficients of the ODZ volumes, WCD rates and average POC flux within the ODZ with both the ONI and PDO index for the four defined 3D ODZ regions. For the correlation with the ONI and the PDO index, the timeseries of ODZ volumes, WCD rates and POC fluxes were deseasonalized. The correlation values in grey are not significant, all other values are significant with $p < 0.01$.

3.2.2.1 The Influence of ENSO on WCD

To further elucidate the effect of ENSO on the mechanisms at play, ENSO composited anomalies to the mean WCD rate and its drivers were mapped, shown in Figure 31. During the hindcast period, La Niña drives an increase of 51% in WCD rates relative to the mean (Figure 34 A). The mean WCD rate during La Niña equals 80.0 Tg N year^{-1}, corresponding to an increase of about 27 Tg N year^{-1} as compared to the mean state of 52.9 Tg N year^{-1}. On the contrary, El Niño drives a slightly smaller change of 47% with a mean El Niño WCD rate of 28.3 Tg N year^{-1}, and a decrease of 24.6 Tg N year^{-1} as compared to the mean state.

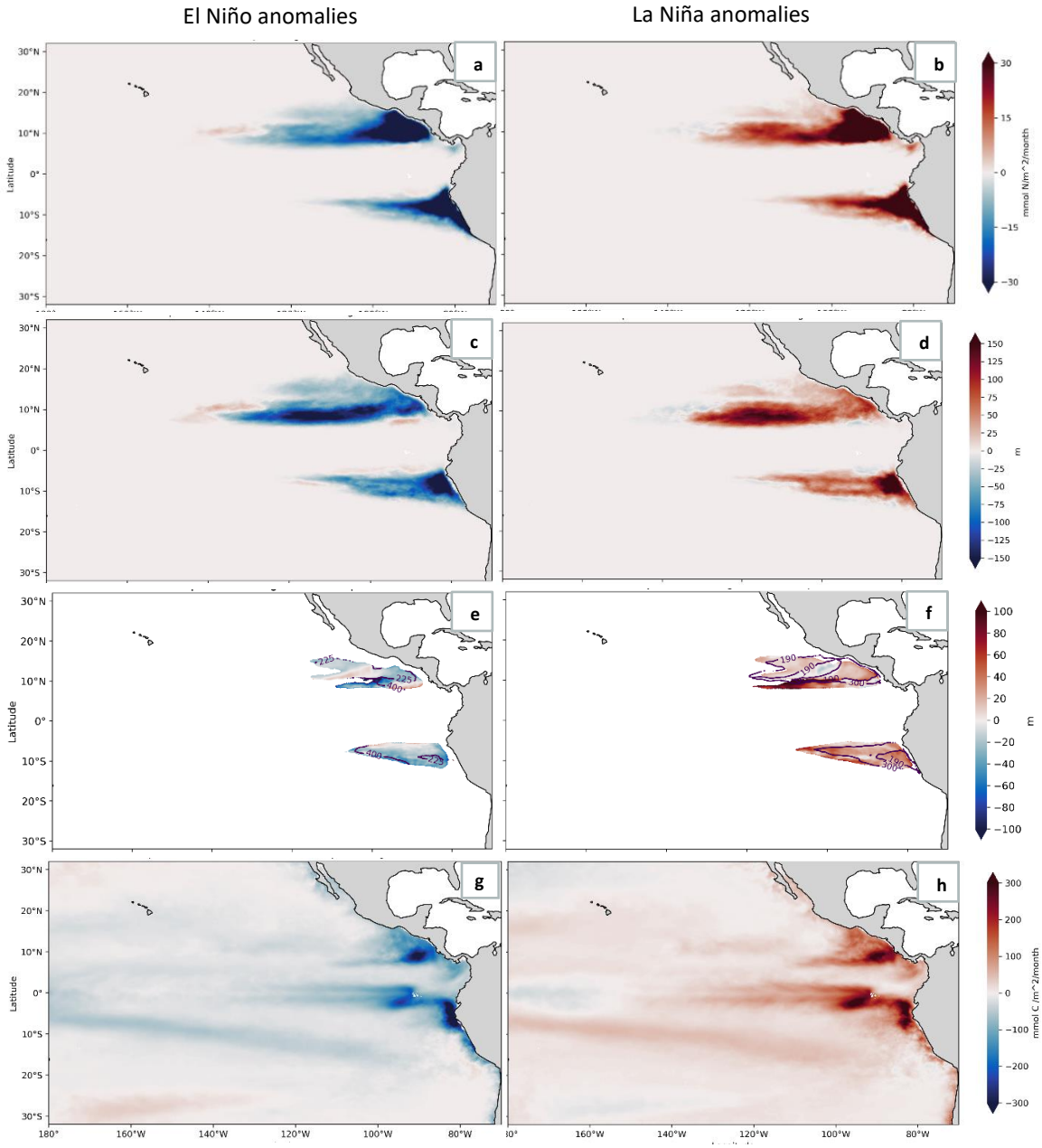

Figure 34. ENSO composited anomalies to the mean. The left column shows the El Niño anomalies, and the right column the La Niña anomalies. a-b) average depth-integrated WCD rates, c-d) average ODZ thickness, e-f) ODZ upper boundaries with contours indicating the ENSO ODZ upper boundaries, g-h) POC flux at 100m depth.

In the spatial extent, the response of WCD to La Niña and El Niño is relatively homologous (Figures 34a and 34b). In the ETNP, ENSO shows strong changes in WCD rates of more than 30 mmol N m^{-2} $month^{-1}$ in the ODZ core to the west, which extend up to ~135°W during La Niña and up to ~140°W during El Niño events. The ENSO-induced changes in WCD are only observed in the regions with approximately more than 50% presence, while in comparison the variable regions show very minor changes. In the ETSP, these changes are more strongly concentrated in the ODZ core to the east. During La Niña (El Niño), the ODZ thickness augments (diminishes) throughout the entire ODZs (Figures 34c and 34d). The changes in ODZ thickness are strongest where the mean ODZ thickness is the largest (shown in Figure 10c) along 10°N in the ETNP, and close to the coast in the ETSP, with changes of up to 150m as compared to the mean. Moreover, the shoaling of the ODZ upper boundaries during La Niña is also most pronounced along 10°N in the ETNP, with anomalies to the mean reaching up to 100m in difference (Figure 34f). In the ETSP the response is more uniform with changes between 20-60m in the ODZ upper boundaries during ENSO. El Niño events show the inverse pattern. During La Niña, the

shoaling (deepening) of the ODZ upper boundaries is accompanied by an increase (decrease) of POC fluxes at 100m depth (Figure 34h). Changes in POC fluxes due to ENSO are concentrated in the cores of the ODZs to the east and additionally to the west of the Galapagos islands where they reach anomalies of up to 300 mmol C m^{-2} $month^{-1}$, and diminish in a westward direction, with the extension of the ODZ.

It has been established that the distribution of the ODZs in the water column is a paramount determinant for the enhancement of WCD. Consequently, the changes induced by El Niño and La Niña were analyzed in depth. Firstly, the temporal patterns of change were determined by plotting the monthly climatologies of the vertically-resolved WCD rates during ENSO (Figures 35 and 36) as compared to the mean (Figure 30).

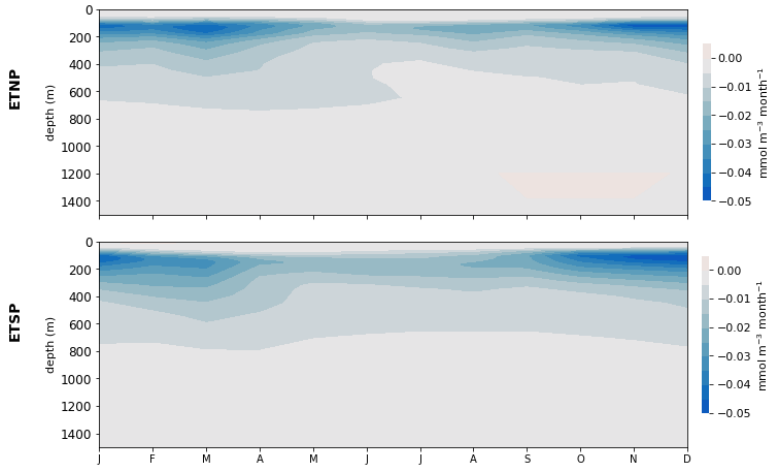

Figure 35. Anomalies of the El Niño composited monthly climatologies to the mean state for the mean depth-resolved WCD rates over the ETNP and ETSP ODZ regions.

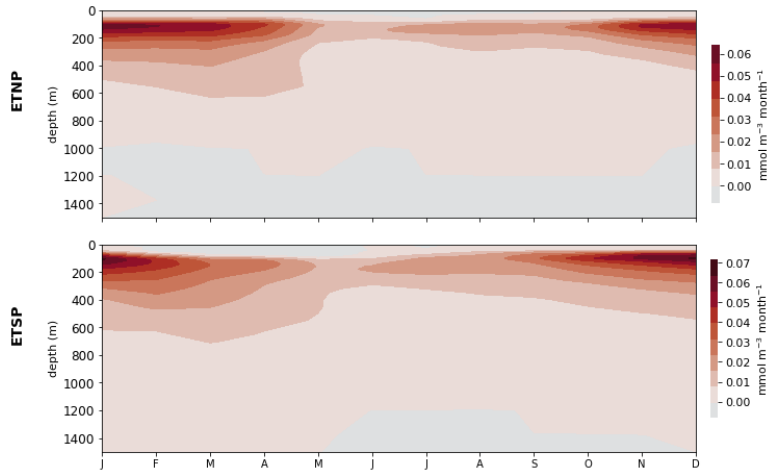

Figure 36. Anomalies of the La Niña composited monthly climatologies to the mean state for the mean depth-resolved WCD rates over the ETNP and ETSP ODZ regions.

The effect of ENSO is strongest from around September to April. Overall, ENSO induces the strongest responses in WCD closer to the surface at ~100-200m depth. At these depths, La Niña induces increases in WCD rates of up to ~0.06 mmol N m^{-3} $month^{-1}$ in the ETNP and up to ~0.07 mmol N m^{-3} $month^{-1}$ in the ETSP, a doubling of the mean maximum rates of 0.08 mmol N m^{-3} $month^{-1}$ and 0.06 mmol N m^{-3} $month^{-1}$, respectively. El Niño relates a similar but inverse response, with a decrease in WCD rates of up to ~0.05 mmol N m^{-3} $month^{-1}$. La Niña induces the shallowing of WCD, with anomalies occurring up to 200m shallower than the mean response in the ETSP (Figure 36) and reaching up to 600m depth.

On the contrary, during El Niño, the WCD anomalies reach a deeper extent than the mean WCD rate, with up to 700m depth in the ETNP and 800m depth in the ETSP.

Superimposed on long-term variability associated with climate modes such as ENSO, short-term variability elicits strong episodic events of WCD enhancement. Figure 37 shows the timeseries of the depth-resolved WCD rates for the period 1998-2004. This period was chosen to give an up-close view of the WCD dynamics during strong El Niño and La Niña events. During this period, three La Niña and two El Niño events occurred, indicated by the blue and red horizontal bars, respectively. These plots show increased WCD rates at the upper boundaries of the ODZ during La Niña periods, in particular from mid-1998 until January 2001, which corresponds with the occurrence of the longest and one of the strongest La Niña events during the hindcast (as indicated in Figures 6 and 31). As markedly illustrated in January 2002 in plot E, even in the stable ZONE50 region during a La Niña event there was an absence of WCD.

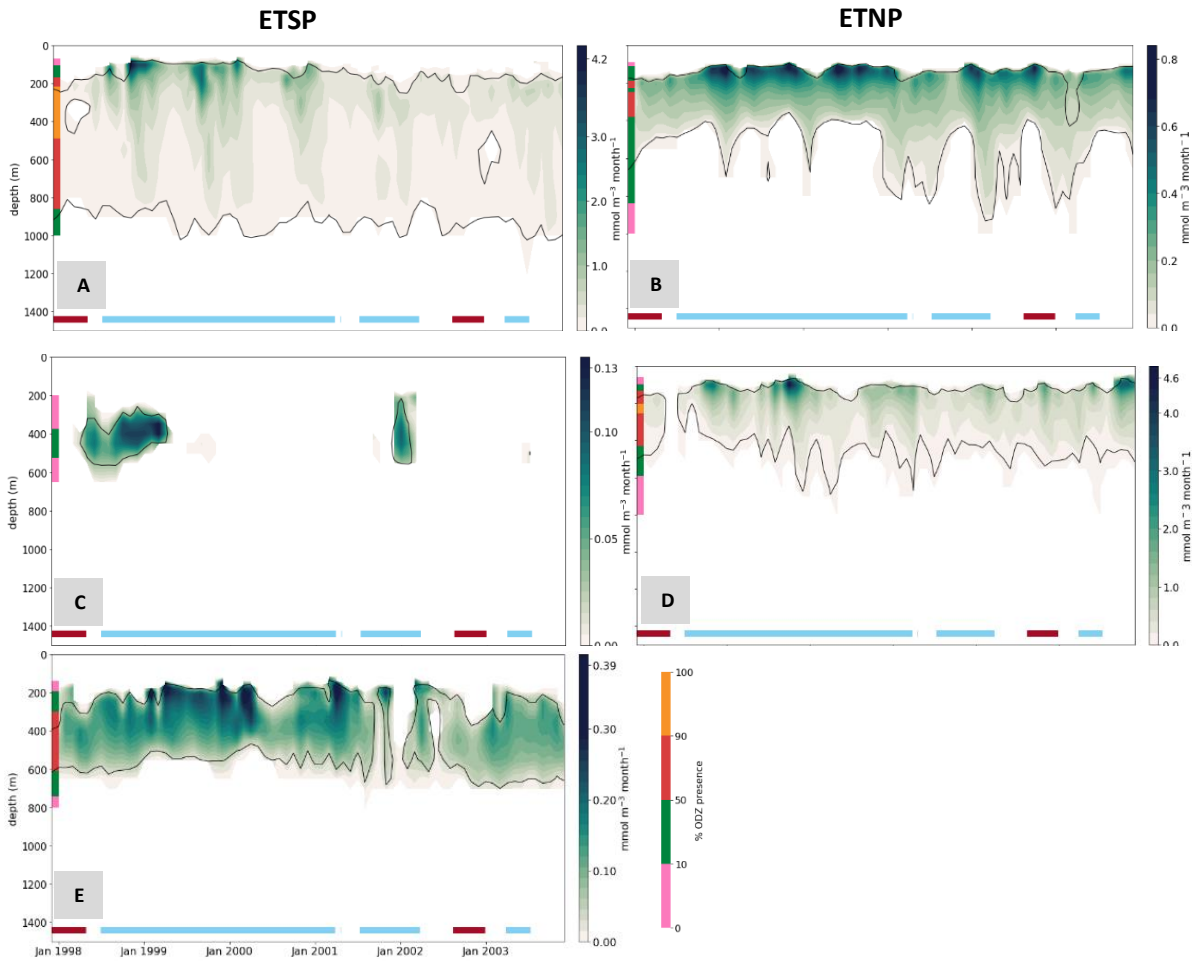

Figure 37. Hovmöller plots of the monthly mean WCD rates in five locations in the ETP from A-E, indicated in Figure 5 Section 2.3.2. A: ZONE90, B:ZONE50, C:ZONE10, D:ZONE90, E:ZONE50. All plots on the left column are in the ETSP, and in the right column in the ETNP. Blue bars on the x-axis indicate La Niña events, and red bars El Niño events. Coloured bars on the y-axis represent the 3D ODZ percentage presence in depth.

3.3 Implications of WCD on Primary Productivity

The last research question studies the implications of WCD to our natural systems, and more specifically to the fundamental base layers of the marine trophic webs, namely primary production. WCD leads to

the loss of bioavailable N from the ecosystem by converting it back to N_2, thus potentially impacting primary production and ultimately C sequestration.

Maps of the N* concentrations averaged in depth intervals from the sea surface to 400m depth show that N limitation was highly concentrated in the core of the ODZ and diminished in a westward direction (Figure 38). The N* signal was strongest between 200-400m depth, with N* values of less than -10 mmol N* m^{-3} within the ODZ (Figure 38C), indicating that the ODZ was the source of this strong N deficiency. The N* deficiency is furthermore visible in the map averaged over the euphotic zone, from sea surface to 100m depth (Figure 38A). Here, the depth-averaged N* concentrations depict N limitations of ~-6 mmol N* m^{-3} within the ODZ delineation, reaching up to ~-8 mmol N* m^{-3} along the coast (Figure 38A). To be able to determine if this N limitation is caused by WCD, and if the signal has the potential to reach the euphotic zone, where it could impact primary production, the N* concentrations were studied in the vertical dimension, as shown in Figure 39.

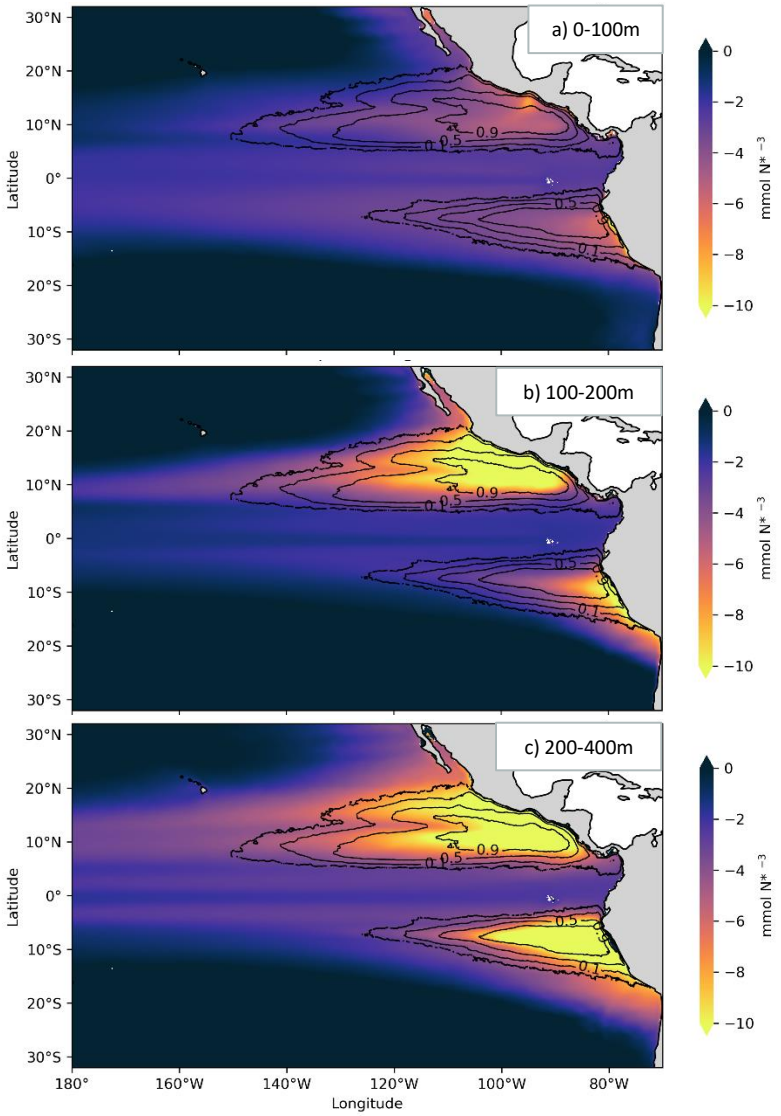

Figure 38. Maps of mean depth-averaged N* concentrations. a) Averaged over the first 100m depth, b) averaged from 100-200m depth, and c) averaged from 200-400m depth. Contour lines show the outer ODZ boundary and the 2D ODZ regions delineation.

The depth-resolved N* concentrations are characterized by a strong decrease within the ODZ, between ~100m and 800m depth, and a homologous decrease in NO_3^- concentrations, visualized in all the ODZ

presence regions (Figures 20-23). The PO_4^{-3} concentrations seem unaffected by these changes. The notion that N* is impacted by WCD is further supported by the N* variability presented in the timeseries at five distinct locations (Figure 24), where N* concentrations strongly decrease with increased WCD rates.

As shown in Figure 39, the N* signal was trapped within the ODZ and increased in magnitude over time. The Hovmöller plots reveal that in the ETSP, the N* signal was strongest (negative) within the mean ODZ, right below the ODZ upper boundaries, while in the ETNP it permeated above the mean ODZ (Figure 39). Furthermore, the bulk of the N* signal was located deeper within the ODZs than the maxima in WCD, which was concentrated at the ODZ upper boundaries (Figures 20-23). The heaving-corrected N* timeseries illustrate the decreases in N* concentrations that are not caused by changes in density, thereby alluding that the strong changes in N* were indeed induced by WCD (Figure 40).

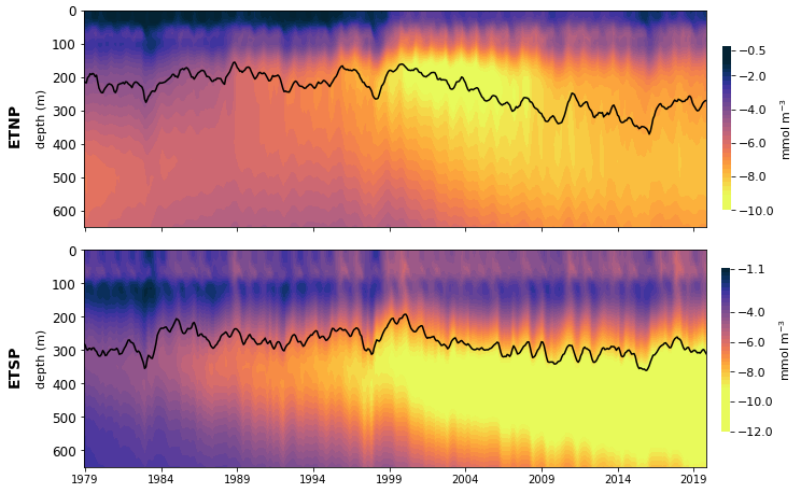

Figure 39. Hovmöller plots of N* concentrations averaged over the ETNP and ETSP WCD regions, shown as the outer delineation in Figure 34. Note that the colour bars for the top and bottom right plots have the same colour range. Black lines indicate the mean ODZ upper boundaries.

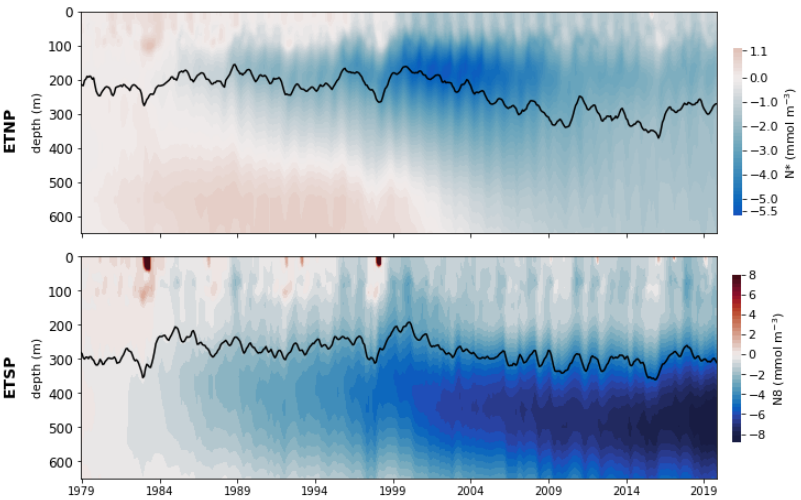

Figure 40. Hovmöller plots of the heaving-corrected anomalies of the mean N* concentrations averaged over the ETNP and ETSP WCD regions, shown as the outer delineation in Figure 34. Note that the colour bars for the top and bottom right plots have the same colour range. Black lines indicate the mean ODZ upper boundaries.

As a final step, the potential impact of changes in N* caused by WCD on C sequestration was examined. By assessing the magnitude of N limitation, we can estimate the proportion of C that remains unfixed

by primary production. To achieve this, we calculated the average concentrations of N* and NO_3^- in the ODZ between 100 to 200m depth, to acquire indicative values for the N limitation beneath the euphotic zone. The average N* concentration was -4.96 mmol m^{-3}, while the average NO_3^- concentration was 28.80 mmol m^{-3}. To determine the percentage of N limitation imposed by the N loss due to WCD, we divided the average N* concentration by the NO_3^- concentration. These rough calculations revealed that the N deficiency corresponded to ~20% of the available mean NO_3^-, thereby reducing the amount of NO_3^- reaching the euphotic zone and supporting primary production by a factor of 20%.

CHAPTER 4

Discussion

4.1 Spatiotemporal Variability of WCD and its Drivers

The first research question aims to characterize the spatiotemporal variability of WCD and elucidate the influence of the ODZ distribution and POC fluxes in controlling these changes. Firstly, the results presented here give a general overview of how WCD experiences a pronounced variability due to the variability of its drivers, both in the horizontal and vertical dimensions. While the ODZs display large interannual to decadal variability (Figure 14) the POC fluxes are more strongly affected by smaller-scale variability and are characterized by monthly to interannual variability (Figure 19). This can be attributed to the different mechanisms controlling the ODZs, which are more strongly affected by ENSO and PDO, and the POC fluxes, impacted by seasonal upwelling and seasonal gap winds. This will be thoroughly discussed in the next chapter. The combined variability of the POC fluxes and ODZs leads to large intra-annual to decadal variability in WCD rates (shown in Figures 14 and 17). Furthermore, the results corroborate the notion that WCD is concentrated at the upper boundaries of the ODZ, coinciding with the larger influx of POC into the suboxic zone, in accordance with the hypothesis. Lastly, it supports the belief that the drivers of WCD exert a synergistic effect on WCD, through the simultaneous shoaling of the ODZ, expansion of the ODZ volume, and increase of the POC fluxes.

4.1.1 ODZ Variability Shapes Distinct WCD Responses

The classification of the ODZ into regions based on their variability revealed that the response of WCD to its drivers is not uniform throughout the ODZ. The spatial variability of WCD is structured as a stable core at ~10°N 90°W in the ETNP and ~7°S 80°W in the ETSP, between approximately 200-600m depth, This stable core is surrounded by increasingly variable regions, both in the horizontal and vertical dimensions, as illustrated in Figures 5 and 20. This spatial pattern is tied to the presence of the ODZ, which relies on a balance between O_2 ventilation driven by mesoscale variability and biological depletion of O_2 (Busecke et al., 2022; Lévy et al., 2021). The analysis of the distinct ODZ variability regions revealed that the highest average volumetric rate of WCD occurs in the highly variable region (ODZ0), followed by the highly stable region (ODZ90, Table 3). To establish how the ODZs and POC fluxes are influencing the WCD rates in the different 3D ODZ regions, we need to consider the distribution of the ODZs in depth and in the geographical extent, as higher POC fluxes are encountered at shallower depths and as the magnitudes of the POC fluxes are not uniform throughout the ETP.

The ODZ0 region, while it has a smaller ODZ volume and shorter residence time, contributes overproportionally to WCD. This discovery is a promising indication of the significance of the highly variable regions in influencing the net N loss due to WCD in the ETP, and elicits further examination of the drivers and mechanisms inducing the episodic WCD events. The ODZ0 region is located at the outer boundaries of the ODZ (illustrated in the horizontal field in Figure 5, and in the vertical dimension in Figures 20-23). The outer regions of the ODZ are subject to stronger variability in the processes controlling O_2 concentrations. At the upper boundaries of the ODZ, biological consumption of O_2 for anaerobic remineralization leads to the expansion of the ODZ (Busecke et al., 2022; Levin, 2018;

Deutsch et al., 2006). In addition, ventilation of the upper ocean is dependent on atmospheric interactions. Both of these processes exhibit strong intra-annual to decadal variability, which induces variability in the ODZs (Karstensen et al., 2008) and thereby leads to the transient events of WCD enhancement (Figure 24C). One plausible explanation for the strong contribution of the highly variable regions to WCD is that they occur at shallower depths, namely from close to the surface to ~50m depth (Figures 20-23), where they encounter high POC fluxes. POC fluxes are the highest in the top 200m (Figures 20-23), since they originate from the mortality and grazing of phyto- and zooplankton, which depend on primary production in the euphotic zone. The spatial distribution of the POC fluxes at 100m depth showed a smaller mean flux in ZONE0 compared to the other zones (Table 4). However, this value only relates to the horizontal distribution of the POC fluxes, and the perspective changes when we take into account the vertical dimension of the ODZs. The ODZ0 region is located at the upper ODZ boundaries near the surface, and thus encounters the highest POC fluxes, shown in Figures 20-23. As hypothesized, this leads to high WCD rates in the highly variable, shallower ODZ region. As the ODZ10 is a big contributor to the total WCD occurring in the ETP, this underscores the importance of intermittent suboxic to anoxic episodes, which can, for instance, be driven by mesoscale eddies or filaments (Altabet et al., 2012; Köhn et al. 2022; Auger et al., 2021) and give rise to the complex and irregular shapes of the ODZ and WCD regions in the ETP.

The high volumetric WCD rates observed in the highly stable ODZ90 region (Table 3) can be attributed to its overall shallower depths compared to the ODZ10 and ODZ50 regions, as well as its location in the ODZ core where POC export fluxes are considerably higher. As shown in Figure 20, the ODZ90 is in its entirety confined to shallower depths (between ~200-550m depth), as compared to the larger and deeper extents of the ODZ50 and ODZ10. In addition, the POC fluxes within ZONE90 are 20% higher compared to the mean values (Table 4 and Figure 11), potentially resulting in increased POC fluxes reaching the ODZ90. It is important to bear in mind that the ODZ90 is encompassed by regions of increased variability, i.e. ODZ50 and ODZ10 (Figures 20b and 20i). Consequently, the elevated POC fluxes in ZONE90 will evidently reach these ODZs before reaching the ODZ90. Although the ODZ50 and ODZ10 cover shallower depths than the ODZ90 region, they have relatively more volume at deeper depths, where WCD rates are close to negligible due to low amounts of organic matter at depths. Thus, in the ODZ50 and ODZ10 the averaged WCD rates are lower than in the ODZ 90, as in these regions the contribution of the small shallow areas with high WCD rates is 'watered-down' by the large ODZ areas at deeper depths. Furthermore, despite that the ODZ50 and ODZ10 also occur within ZONE90, they contain large volumes in ZONE50 and ZONE10, where POC fluxes are comparatively lower leading to lower averaged WCD rates.

These findings support the hypothesis that the high WCD rates in the ODZ90 region can be attributed, at least in part, to the higher POC export fluxes in the region. Moreover, the high POC fluxes would contribute to the establishment of a constant ODZ through the depletion of O_2 by biological O_2 consumption. In summary, the higher WCD rates in the ODZ90 as compared to the ODZ50 and ODZ10 can be attributed to the stronger POC fluxes in ZONE90, and to the location of the ODZ90 at shallower depths, thereby receiving higher POC fluxes for remineralization into the ODZ. The volumetric ODZ50 and ODZ10 WCD rates are diminished by the larger extent in depth of these ODZs, and lower POC fluxes where the larger part of the ODZ is located.

4.1.2 Synergistic Effects Between the WCD Drivers

The analysis of the WCD drivers over time and the subsequent effects on WCD revealed that the variability of WCD is not solely dependent on the variability in ODZ volume and POC fluxes, but is further dependent on the vertical distribution of the ODZ in the water column. The results indicate that

the shoaling of the ODZ upper boundaries and the concomitant increase in POC fluxes occur simultaneously throughout the timeseries (Figures 24 and 25), displaying a positively reinforcing effect between these phenomena that are likely driven by the same underlying mechanisms. When intermediate low-oxygenated, nutrient-rich waters are upwelled, this leads to a shoaling of the ODZ while simultaneously increasing biological production through nutrient replenishment. This manifests itself in higher POC export fluxes, thereby further inducing O_2 depletion through aerobic remineralization and expansion of the ODZ at its upper boundaries (Cabré et al., 2015). Together, these synergistic processes have an amplifying effect on WCD. The correlation of the POC fluxes with the ODZ upper boundaries shows that this phenomenon is most notably observed in the core of the ODZ (Figure 25), where strong and stable WCD occurs. The western region of the ETNP ODZ shows low correlations, however, this region is where the ODZ is more variable and occurs for only a certain fraction of the hindcast period. This phenomenon is furthermore observed in the context of ENSO, where we show that in the ODZ core, the impact of ENSO on WCD is more pronounced than on the ODZ volume and POC fluxes combined, and displays a strong correlation with changes in the ODZ upper boundaries (Figure 33). This finding confirms the previous suggestion by Yang et al. (2017) that WCD is enhanced through the amplifying effect of its drivers.

4.1.3 Differing WCD Dynamics in the ETNP and ETSP

Results showed that a larger fraction of the annual spatially-integrated WCD is contributed by the ETNP and a smaller one by the ETSP, which are separated at the equator by more oxygenated waters (Table 3). However, in contrast with this observation, the ETSP displayed higher WCD volumetric rates than the ETNP. Analysis of the WCD and ODZ timeseries (Figure 14) revealed that the spatially-integrated WCD rates were similar for the largest portion of the hindcast, while the ETNP ODZ volume was approximately 40% larger than the ETSP ODZ. This suggests that the ODZ and POC fluxes driving WCD in the ETNP and ETSP are influenced by the same underlying mechanisms, however, the WCD rates are impacted in a differing manner. While the ODZs reach a deeper extent in the ETSP, up to 1200m as compared to the ETNP with 1000m, the area of the regions reaching these depths is negligible (Figure 20). The regions with considerably larger areas are located at shallower depths in the ETSP than in the ETNP. Furthermore, the ODZ90 region, which contributes substantially to WCD, with 10.2% of the total WCD contribution over the ETP (Table 3), is larger in the ETSP than in the ETNP (Figure 20). In addition, the POC fluxes at 100m depth within the ETSP ODZ are stronger than in the ETNP ODZ (Table 2 and Figures 10 and 21-23), thereby inducing higher WCD rates within the ETSP ODZ. Overall, the comparable annual WCD rate in both regions throughout the majority of the hindcast (Figure 14), despite the almost doubling in size of the ETNP ODZ (Table 2), is attributed to the shallower occurrence of the ETSP ODZ, the considerable larger area of the highly stable ETSP ODZ90 volume, and the augmented POC fluxes within the ETSP ODZ.

4.2 Climate-Forced Dynamics of WCD Variability in the ETP

The second research question builds on the previous findings and delves deeper into how climatic variability induced by the seasonal cycle, ENSO and PDO drives exhaustive fluctuations in WCD in the ETP. Through atmosphere-ocean circulations, these climatic modes of variability induce large changes in winds and sea surface temperatures from intra-annual to decadal timescales. These in turn lead to variations in primary production, organic matter export, and ODZ distribution, shaping the WCD dynamics over extended periods.

4.2.1 Seasonal Dynamics of WCD

In the ETP, the seasonal pattern is dictated by the shifting of the Inter-Tropical Convergence Zone (ITCZ), changes in local winds, and temperature-induced changes in upper ocean structure and circulation (Pennington et al., 2006). These factors lead to changes in currents and upwelling, in turn affecting primary production through nutrient limitation. This subsequently determines the export of POC and the ODZ distribution, due to the upwelling of O_2 low waters and high respiration rates related to increased POC remineralization. The seasonal anomalies of the outer ODZ regions negligible differences with the mean WCD rates, thereby indicating that the seasonal cycle does not induce considerable differences in the highly variable regions. Quantification of the ODZ volumes throughout the seasons revealed that they remain relatively homogenous (Table 5). Moreover, the ODZ thickness and ODZ upper boundary anomalies do not relate a uniform response of ODZ to seasonality and exhibit significant stochasticity (Figures 27 and 28). A potential explanation for this is that the changes observed in the ODZs are primarily driven by small-scale variability rather than being strongly influenced by the seasonal cycle. Additionally, in the vertical dimension (Figure 30), the extent of WCD does not display substantial variations across different months and suggests that the ODZ lacks a well-established pattern of fluctuations throughout the seasons. These minimal changes in ODZ do not seem to govern the changes in WCD. As shown by the timeseries of the ODZs and POC fluxes (Figures 14 and 19), the seasonal cycle exerts its influence predominantly on the POC fluxes (Pennington et al, 2006) and to a lesser extent on the ODZs.

In the ETNP, the increased POC fluxes within the ODZ during winter and spring (Figure 29) correspond to the locations of the intense gap winds, namely at the Gulfs of Tehuantepec, Papagayo, and Panama (McCreary et al., 1989). These strong and intermittent gap winds are highly seasonal and blow during boreal winter (December to April) through each of the three Gulf regions (Amador et al., 2006). The gap winds cause enhanced primary production in the ODZ core by inducing the upwelling of nutrient-rich waters and the formation of mesoscale eddies (Pennington et al., 2006). Subsequently, this increases the export of organic matter for remineralization by more than 250 mmol C m^{-2} $month^{-1}$. This phenomenon explains the increased WCD rates during winter and spring in the ETNP, and the negative anomalies during summer and autumn when the gap winds are absent (Pennington et al., 2006). The Papagayo region, located between the Tehuantepec and Panama regions, includes the presence of the Costa Rica Dome, which shows a contrasting seasonal pattern to its surrounding area. During the transition from fall to winter, the thermocline in the Costa Rica Dome deepens (Figure 28), thereby diminishing nutrient influx, which decreases the primary production and POC export (Pennington et al., 2006) and thereby leads to a decrease in WCD rates of up to 40 mmol N m^{-2} $month^{-1}$ as compared to the mean (Figure 26). During spring the opposite pattern is observed, where the Costa Rica Dome shoals by up to 50m and the WCD rates increase with more than 40 mmol N m^{-2} $month^{-1}$.

In the ETSP, strong WCD rates are recorded during boreal winter, when winds induce strong coastal upwelling in the ODZ core, and to a smaller extent farther south off southern Peru and Chile (Pennington et al., 2006). This leads to increased primary production and subsequently higher POC fluxes during boreal fall and winter (Echevin et al., 2008), as visualized in Figure 29, thereby driving the seasonal response in WCD.

In the vertical dimension, the monthly WCD climatologies are relatively uniform throughout the seasons and do not indicate strong variability in depth (Figure 30). As stated, the seasonal response of WCD displays large spatial differences, and thus the variability in the system would be masked out when averaging the WCD response over 41 years and the entire ODZ regions. Furthermore, as the seasonal response of the ODZs is minor and highly stochastic, this would explain the small changes in

the vertical extent of spatially-averaged WCD rates through the seasons. Minor differences in WCD rates are visible between 100m and 400m depth, where WCD is strongest from approximately October to May (Figure 30) in agreement with the above-stated results. The increase in the intensity of the WCD rates below the euphotic zone up to 400m depth between mid-autumn to mid-spring in both the ETNP and ETSP can be attributed to the increased POC fluxes within the ODZ during this period, as seen in Figure 29.

4.2.2 The Influence of ENSO on WCD

Previous studies have identified ENSO as a dominant mode of variability in the ETP (Rasmusson and Wallace, 1983; Wang and Fiedler, 2006; Amador et al., 2006), thereby having a strong influence on WCD variability (Yang et al., 2017). Our results further validate this notion and find that ENSO describes 54% of the interannual WCD variability in the ETP. In addition, in this study we distinguished specific ENSO-driven changes on WCD in the different ODZ variability regions. Lastly, we showed that the observation of WCD events in situ is severely restricted by the strong superimposed small-scale, inter-annual and decadal variability.

During La Niña episodes, the strengthened westward blowing trade winds lead to the increased zonal tilting of the isopycnals and the stronger upwelling of cold, nutrient-rich waters in the ETP (Amador et al., 2006). This triggers the previously discussed synergistic effects between the WCD drivers, inducing higher POC export fluxes (Figure 34D), and expansion of the suboxic waters which is observed in the shoaling of the ODZ (Figures 34C and 36) and increase in ODZ thickness (Figure 34B). These findings are furthermore corroborated by the strong negative correlations between the ONI and the WCD drivers (Figure 33). These changes drive a 51% increase in WCD rates during La Niña episodes (Figure 34A). During El Niño events, the trade winds weaken, which disrupts the normal upwelling and increases the stratification of surface waters (Amador et al., 2006). This leads to a decrease in POC export fluxes (Figure 34D), the deepening of the ODZs (Figures 34C and 35), and the diminishing of the ODZ thickness (Figure 34B), thereby driving a 47% decrease in WCD (Figures 33 and 34A).

The differing impacts of ENSO on WCD in the four ODZ regions show weaker absolute correlations for the highly variable region. This suggests that the variability of WCD in the highly variable ODZ regions is less determined by changes in ENSO. Due to the significantly high stochasticity in that region, oceanic and atmospheric changes in ENSO will not as largely affect WCD in this region. This is confirmed by the mapped WCD anomalies (Figure 34A), where a strong ENSO effect is concentrated at the core of the ODZ, and is minimal in the outer regions. In all four ODZ regions the POC flux is correlated with ONI to a similar extent, indicating that the influence of ENSO on the POC fluxes occurs over the entire ODZ. However, in terms of the magnitude of the changes, the mapped anomalies to the mean POC fluxes (Figure 34D) illustrate that the anomalies are strongest in the ODZ core, partly contributing to the strong increase (decrease) of WCD in this region during La Niña (El Niño) episodes. The relatively weaker correlation values between ONI and the ODZ volume in the highly stable (ODZ90) region can be explained as the ODZ is already present more than 90% of the time. Hence, the room for expansion within this region is solely 10% or less. In agreement with this, the strongest anomalies to the ODZ thickness are not in the ODZ core, but rather where the ODZ thickness is largest, along 10°N in the ZONE50 (Figure 10 and 34B). In addition, this region along 10°N is where the strongest shoaling (deepening) of the ODZ upper boundaries occurs, with changes of almost 100m depth (Figure 34C). This area coincides with the region of increased (decreased) WCD rates during La Niña (El Niño) episodes. The ODZ upper boundaries show weak or insignificant correlations for all regions, except for ODZ90. This can be attributed to the variability in the presence

of the ODZ in the more variable regions, resulting in a non-continuous timeseries where the ODZ upper boundary is occasionally absent. Consequently, the correlations between the ODZ upper boundaries timeseries and ONI in these variable regions are weaker or insignificant. It is important to note that this absence of the ODZ does not affect the correlations of the ODZ thicknesses. In the context of the ODZ thickness, a value of 0m signifies the absence of the ODZ. However, for the ODZ upper boundaries, the absence of the ODZ is indicated by the absence of a value for the upper boundary, as a value of 0m would indicate an upper boundary that reaches the sea surface. Overall, it can be established that ENSO-induced changes in WCD in the intermediate variability regions are dominated by variations in the ODZs, while in the ODZ cores closer to the coast the extensive changes in WCD changes driven by both strong variation in the POC export and the ODZs.

In terms of absolute values, our finding that ENSO explains 54% of the WCD variability in the ETP largely agrees with the 64% found by Yang et al. (2017). However, their study found that ENSO induces a change of ±13 Tg N $year^{-1}$, in contrast to our findings of +27 Tg N $year^{-1}$ during La Niña and -24.6 Tg N $year^{-1}$ during El Niño events. These differences between the absolute values found in this study compared to the values reported by Yang et al. (2017) can be attributed to different approaches in the computation of the ONI and the deseasonalization and detrending of the data. Moreover, it is likely that larger changes in the POC fluxes and changes in the oxycline between both studies have led to strong differences in these estimations. In addition, we have established that the effects of La Niña and El Niño are considerably symmetrical, with La Niña events inducing a slightly stronger response of the WCD drivers and WCD than El Niño events. This difference could be attributed to differences in the intensity and duration of the El Niño and La Niña events during the 1979-2019 hindcast. This facet was not covered by the previous work of Yang et al. (2017), but is important to take into account when estimating changes induced by ENSO. The findings of the ENSO-driven changes in the ODZ distribution and POC fluxes are in line with the results of previous studies (José et al., 2019, in press; Stramma et al., 2016).

4.2.3 The Influence of PDO on WCD

From our results we can establish that the PDO exerts a substantial influence on WCD variability, describing 15.7 % of its decadal variability. Correlations of the WCD drivers with the PDO index suggest that WCD is enhanced during negative (cold) phases through the enhancement of POC fluxes, increase in ODZ volumes and shoaling of the ODZ (Figure 33), in accordance with the findings by Deutsch et al (2011).

This study furthermore highlights the importance of small-scale variability superimposed on interannual and decadal fluctuations. The study by Horak et al. (2016) did not find a correlation between the PDO index and WCD, and therefore concluded that WCD is not influenced by the PDO. However, their analysis was based on hydrographic measurements in the ETNP from four cruises. As shown in this Figure 37, while the overall WCD does respond considerably to both ENSO- and PDO-induced forcing, the WCD response is not even and retains a high variability due to transient and episodic events. This places a hard limitation on our capacity to observe and study WCD events and their mechanisms in situ.

4.3 Implications of WCD on Primary Productivity

The final research question reviews the impact of WCD on marine ecosystems. During WCD, NO_3^- is converted back to N_2, thereby causing oceanic N loss with potential impacts on primary production, C sequestration, and ultimately climate change.

Our results confirm that the decrease in N* concentrations occurs within the ODZ (Figures 20-23 and 38) and is led by NO_3^- depletion due to WCD, and not due to density fluctuations or changes in PO_4^{-3} concentrations (Figures 40 and 20-23). This is expected due to no PO_4^{-3} sink within the ODZ. As shown in Figure 39, N* is an accumulative tracer and the low N* signal is augmented over time within the ODZ. The strongest N* signal is located at deeper depths compared to the maxima of WCD, which are concentrated at the upper boundaries of the ODZs. This is explained as the ODZ upper boundaries are at the interface where remineralization of organic matter occurs through respiration, thereby replenishing the NO_3^- reservoir and decreasing the strength of the negative N* signal.

In seawater, N primarily exists as inert dissolved N_2 gas, making it inaccessible to most organisms. The bioavailable form of N, NO_3^-, is of paramount importance as it provides an energetically favorable N source for organisms. Once NO_3^- is converted back to N_2 by bacteria by WCD, it becomes less accessible for assimilation (Voss et al., 2013). Primary production, which occurs in the euphotic zone where light availability allows for photosynthesis, is stimulated by the upwelling of deeper nutrient-rich waters. However, in regions of strong WCD, such as in the ETP ODZs, WCD consumes NO_3^-, thereby depleting the upwelling waters of this crucial element for marine productivity (Pennington et al., 2006). The euphotic zones above the ODZs are particularly vulnerable to the impacts of WCD, as the N deficient waters are upwelled, potentially disrupting primary production in these regions. Our findings support this hypothesis, as we observe an extension of the N* signals above the ODZ into the euphotic zone, shown in Figures 38 and 39, aligning with the findings by Chang et al. (2010) and Löscher et al. (2016). Our rough estimate indicates that WCD induces a decrease of approximately 20% in the amount of NO_3^- available for assimilation by primary producers within the euphotic zone. Moreover, the N-deficient waters can be advected to other regions, exerting widespread effects on primary production and ecosystems (Gruber, 2008). Figure 38 illustrates the presence of low N* waters with values below -4 mmol N* m^{-3} originating from the ODZs and extending into the central Pacific beyond 180°W, where high O_2 concentrations would inhibit WCD. This finding suggests a westward advection of the N deficient waters by the North and South Equatorial currents, as suggested in previous studies (Deutsch et al., 2001; Gruber, 2008; Castro et al., 2001). Furthermore, this effect was shown by Callbeck et al. (2017) in the context of eddies, where the N* signal was trapped and transported inside the eddy. Oceanic input of N through N_2 fixation cannot compensate for the created N deficit and therefore, resupply of N would need to happen through large-scale N transport such as by the EUC, or other pathways of ventilation into the ODZ and euphotic zone (Yang et al., 2017). Consequently, due to the relatively rapid turnover of N in the ocean, WCD can swiftly disrupt the marine N cycle leading to significant consequences for marine productivity (Gruber, 2008). The perturbation of the marine N cycle could potentially lead to ecosystem shifts in microbiota and phytoplankton e.g. a decrease of N* at surface waters could illicit a response from diazotrophs and induce N_2 fixation in the areas impacted by WCD (Gruber, 2016).

In addition, the bioavailability of N determines the efficiency of the biological pump, which regulates the oceanic uptake of atmospheric CO_2, and is a big determinant in the planet's response to climate warming (Falkowski, 1997; Gruber and Sarmiento, 1997; Neuer, 2002; Karl et al., 2002). WCD, through its depletion of NO_3^-, hampers C assimilation by primary producers, which represents a loss in the efficiency of the biological pump thereby impeding the process of sequestering atmospheric CO_2 in the deep ocean. When NO_3^- deficient waters are upwelled, this increases the outflux of CO_2 into the atmosphere, as the C is not sequestered by primary production and thus the residual CO_2 concentration in the upwelled waters is larger. The ETP is the largest global oceanic source of CO_2 to the atmosphere (Pennington et al., 2006; Tans et al., 1990) and thus WCD, by increasing the CO_2 outflux into the atmosphere and by leading to the production of the GHG N_2O, acts as a determining positive feedback factor in the warming world and further contributes to climate warming (Gruber, 2008).

4.4 Limitations

The limitations of this study encompass various aspects that should be acknowledged. First and foremost, it is imperative to recognize that the use of models introduces inherent biases and uncertainties. In this study, this particularly applies to the parametrization of organic C remineralization, variability and distribution of the ODZs, and WCD. Notably, the model treats WCD as a single joint process, rather than the two separate, but synchronous, processes of canonical denitrification and anammox. Furthermore, the precise mechanisms underlying these processes are not fully understood. Large knowledge gaps remain regarding various aspects, including reaction rates, the specific thresholds triggering these processes (such as O_2 concentrations and availability of NO_3^-), the spatial and temporal distributions of the individual processes, and additional limitations imposed by the environment. Studies have reported significant variations in these values (Lam and Kuypers, 2011), which hinders precise parametrization within the model. Additionally, a study by Bianchi et al. (2018) suggests that approximately half of the WCD may occur in waters with O_2 concentrations ranging from 5 to 60 mmol m^{-3} due to the presence of suboxic microenvironments in sinking particles. This challenges the prevailing assumption that WCD predominantly occurs in the ODZs and elicits the reconsideration of current modelling and estimation approaches. While the model performs well in representing the ODZ dynamics, discrepancies with observations still exist. Regarding the BEC component, the model does not account for specific phytoplankton communities found in the Humboldt Current system (Köhn, 2022), and smaller-scale processes such as viral lysis are not included. These omissions could potentially impact fluxes at larger scales (Löscher et al., 2016; Gazitúa et al., 2021).

Additionally, while the use of a model enables the comprehensive study of the processes with higher resolution in both temporal and spatial dimensions than can currently be obtained with observation-based studies, there are still inherent limitations. In the spatial dimension the study of the processes is restricted by the grid size and the depth levels. The interpolation from s-levels to z-levels further induces approximations in the vertical dimension which are inevitably accompanied by biases. In the temporal dimension, the analyses in this study are predominantly performed with monthly averaged fields to maximize the amount and intricacy of the conducted analyses within the given time frame. As the analyses are targeted to processes occurring on monthly or longer timescales, it is assumed that the monthly averaged values are representative. However, some minor biases persist, which diminish our ability to fully capture the variability of WCD and its drivers.

It is crucial to note that the findings of this study primarily pertain to the ETP ODZs. The described mechanisms controlling WCD might not scale with processes occurring in other ODZs such as e.g. in the Arabian Sea, where the physical forcings and biological processes are known to be considerably different (Paulmier and Ruiz-Pino, 2009). Therefore, the generalizability of the study's conclusions to other regions may be limited.

To more accurately represent the effect of ENSO on WCD, it would be beneficial to detrend and deseasonalize all the data used in the analyses, in order to eliminate any variability induced by smaller-scale or larger-scale variability. However, in this study, detrending and deseasonalization were only performed on the timeseries correlation with the ONI due to time constraints, while the correlation of the ONI (and PDO index) with the WCD drivers was performed with deseasonalized timeseries. Furthermore, by using composites of all La Niña and El Niño occurrences, we assume that all events behave equally. These simplified approaches may affect the overall robustness of the results.

Furthermore, this study is limited in its capacity to analyze the influence of PDO on WCD variability. The determination of the impact of PDO on WCD requires a simulation spanning several decades, to capture a sufficient sample size of positive and negative PDO periods. The hindcast

simulation used in this study from 1979 to 2019 solely includes two major PDO regime shifts, namely in the late 1970s and late 1990s (Ma et al., 2022). Consequently, the 41-year hindcast would not adequately represent the full range of PDO impacts, and thus we limited the more extensive analyses to the impacts of ENSO on WCD.

The use of the N* tracer as a proxy for N limitation comes with the assumption that there is a constant Redfield ratio, and the absence of limitations by other nutrients, which might not always be the case. The N* tracer provides a useful proxy to estimate the time- and space-integrated impact of WCD on the N inventory. However, WCD is not the sole process impacting N*, as it is also dependent on N replenishment by N fixation, which cannot be distinguished when using this proxy. Nonetheless, these processes are often spatially and temporally separated, thereby aiding the interpretation of these results (Gruber, 2008).

In addition, the interpretation of the results presented in this study is limited by assumptions and approximations made during the calculations. For instance, the approximation of the bottom of the euphotic zone at 100m depth is a simplification. A more suitable approach would involve using the 1% of photosynthetically available radiation (PAR) as an indicator of the bottom of the euphotic zone. Furthermore, the estimation of the percentage reduction in C sequestration by WCD is also an approximation. This calculation was intentionally kept simple to provide an initial understanding of the potential impacts of WCD on the climate. However, to acquire more robust and accurate results, it would be necessary to incorporate the scaling of this process with other factors involved in the transfer of dissolved C to C sequestration, such as other sources of N input and other limitations on C assimilation by primary producers.

CHAPTER 5

Conclusion and Outlook

The remineralization of organic matter in the ETP ODZs through WCD was estimated at 52.9 Tg N $year^{-1}$, and exhibits large variability, spanning from short-term monthly fluctuations to decadal changes. We find that in the ETP this process yields the highest N losses in the stable ODZ cores, at approximately 10°N 90°W in the ETNP and 7°S 80°W in the ETSP between 200 and 600m depth. These ODZ cores are surrounded by increasingly variable regions with large intra-annual to decadal variability. Our findings revealed that WCD occurs predominantly at the upper boundaries of the ODZ, and is enhanced by the synergistic effects of its drivers, through the simultaneous shoaling of the ODZ, expansion of the ODZ and increase in POC export fluxes. Furthermore, we show that the highly variable regions of the ODZ, where WCD occurs sporadically in strong episodic events, contribute overproportionally to the net N loss. The identification of the highly variable regions as critical zones of WCD underscores the importance of investigating the contribution, underlying mechanisms and impact of mesoscale variability, particularly eddies, in driving WCD. In addition, we identified differing WCD dynamics between the ETNP and ETSP ODZs. Despite being 40% smaller in size than the ETNP ODZ, the ETSP ODZ exhibited higher volumetric WCD rates, attributed to the shallower occurrence of the ODZ, larger stable ODZ core region and higher POC fluxes.

On longer timescales, the strong variability of WCD in the ETP is driven by climatic forcing, in particular by the seasonal cycle, ENSO, and PDO. Seasonal fluctuations in the ITCZ, local winds, and temperatures impact currents and upwelling patterns, leading to changes in the availability of POC and ODZ distribution that drive WCD dynamics. The largest seasonal changes in WCD are observed in the ODZ cores and are primarily influenced by variations in POC export fluxes. In the ETNP ODZ, strong intermittent gap winds during boreal winter result in intensified WCD through the strong local increase in POC export fluxes. Conversely, the Costa Rica Dome exhibits stronger WCD during spring due to the shoaling of the ODZ and concomitant increase in the export of POC. In the ETSP, seasonal variations in wind-induced upwelling during boreal autumn and winter lead to the enhanced availability of POC, thereby driving a strong seasonal increase in WCD.

On interannual timescales, we find that ENSO significantly influences WCD in the ETP, leading to variations of approximately 50% in the mean WCD rates. During La Niña episodes, the strengthening of the westward-blowing trade winds induces an amplification of WCD through the synergistic interactions of its drivers. Specifically, the ODZ core experiences the strongest increases in WCD rates through the enhancement of POC export and the expansion and shoaling of the ODZ. In regions with intermediate variability, where ODZ presence ranges from 50% to 90%, particularly along the 10°N region, the dominant factor contributing to the increase in WCD is the shoaling and expansion of the ODZ. El Niño episodes drive a symmetrical decrease in WCD rates. Additionally, we find that the PDO describes 15.7% of the decadal variability in WCD. The correlations of WCD and its drivers with PDO suggest that the PDO induces increases in WCD during negative (cold) PDO phases, through similar mechanisms as observed with ENSO. However, our analyses revealed that even in the presence of

strong La Niña or El Niño events, WCD is largely driven by episodic and transient events thereby presenting challenges in our capacity to observe WCD events in situ.

Lastly, our study highlights the impact of WCD on the decrease in the marine NO_3^- inventory. We estimate that WCD induces an N deficiency of roughly 20% of the available mean NO_3^-, affecting the euphotic zones above the ODZs and extending up to the central Pacific, potentially disrupting primary production. This could constitute effects on phytoplankton abundance and ecosystem composition. The decrease in NO_3^- availability would furthermore reduce the efficiency of the biological pump, decreasing the uptake of atmospheric CO_2 and leading to increased oceanic CO_2 outflux to the atmosphere. Furthermore, as WCD contributes to the production of the GHG N_2O, these joint effects of WCD would exacerbate climate warming, acting as a positive feedback factor in climate warming (Gruber, 2008).

In this study we contribute to the broader understanding of drivers, patterns, and impacts of WCD variability in the ETP, and give an indication of its impact on marine ecosystems. However, major questions remain regarding the long-term impact of WCD on marine ecosystems and the global climate. Under the pressures of climate warming and oceanic deoxygenation, the ETP ODZs are projected to undergo large changes. Due to their small size, ODZs are particularly sensitive to volume changes, with some studies projecting an expansion (Oschilles et al., 2008) and others a shrinking of the suboxic zones (Busecke et al., 2022; Deutsch et al., 2014). Regardless, both scenarios would entail substantial modifications in the WCD regions (Deutsch et al., 2011). Hence, a comprehensive understanding of the evolution of ODZs, particularly focusing on their variability and distribution as highlighted in this study, is crucial for predicting changes in the marine N cycle. An additional research avenue of interest is the potential spatial coupling between regions of WCD and marine N_2 fixation, as the NO_3^- deficient waters in the euphotic zone induced by WCD could provide a niche for diazotrophs (Gruber, 2016). Additionally, further research is needed to deepen our understanding of the individual processes and microorganisms involved in mediating WCD and their environmental constraints. In the context of increased GHG emissions and the alteration of the natural N cycle, there is a need for more robust studies into the influence of WCD on CO_2 dynamics and N_2O emissions, and what this entails for the future of climate change. In this regard, the determination of the relative contributions of canonical denitrification and anammox to WCD gains importance as these processes have differing impacts on CO_2 and N_2O dynamics. By advancing the knowledge of the processes driving WCD variability, we lay a foundation for forecasting future changes in WCD dynamics and understanding their impact on marine ecosystems and global biogeochemical cycles.

Acknowledgements

I would like to thank my supervisors, Jana Härri, Eike Köhn and Nicolas Gruber, for their guidance and support during this thesis, and additionally to Niki (and Meike Vogt) for giving me the opportunity to conduct my thesis in such an admirable and inviting research group. Many thanks to Matthias Münnich, for sharing your office with me during these six months, for the scientific support, and for all the enriching conversations. A heartfelt thanks to everyone in the UP group for all the guidance, advice and wonderful times. I want to thank Carla for diligently proofreading my thesis and for providing support throughout the process. Last but not least, I want to thank my IMBRSea colleagues, for I am immensely grateful to be a part of such a passionate, encouraging and supportive community.

References

Altabet, M. A., Ryabenko, E., Stramma, L., Wallace, D. W. R., Frank, M., Grasse, P., & Lavik, G. (2012). An eddy-stimulated hotspot for fixed N-loss from the Peru oxygen minimum zone. *Biogeosciences, 9*(12), 4897–4908. https://doi.org/10.5194/bg-9-4897-2012

Amador, J. A., Alfaro, E. J., Lizano, O. G., & Magaña, V. (2006). Atmospheric forcing of the eastern tropical Pacific: A review. *Progress in Oceanography*, *69*(2–4), 101–142. https://doi.org/10.1016/j.pocean.2006.03.007

Armstrong, R. C., Lee, C., Hedges, J. I., Honjo, S., & Wakeham, S. G. (2001). A new, mechanistic model for organic carbon fluxes in the ocean based on the quantitative association of POC with ballast minerals. *Deep-sea Research Part Ii-topical Studies in Oceanography*, *49*(1–3), 219–236. https://doi.org/10.1016/s0967-0645(01)00101-1

Auger, P. A., Bento, J. P., Hormazabal, S., Morales, C. E., & Bustamante, A. (2021). Mesoscale Variability in the Boundaries of the Oxygen Minimum Zone in the Eastern South Pacific: Influence of Intrathermocline Eddies. *Journal of Geophysical Research: Oceans, 126*(2). https://doi.org/10.1029/2019jc015272

Babbin, A. R., Bianchi, D., Jayakumar, A., & Ward, B. B. (2015). Rapid nitrous oxide cycling in the suboxic ocean. *Science, 348*(6239), 1127–1129. https://doi.org/10.1126/science.aaa8380

Battaglia, G., & Joos, F. (2018). Marine N2O Emissions From Nitrification and Denitrification Constrained by Modern Observations and Projected in Multimillennial Global Warming Simulations. *Global Biogeochemical Cycles, 32*(1), 92–121. https://doi.org/10.1002/2017gb005671

Bianchi, D., Weber, T., Kiko, R., & Deutsch, C. (2018). Global niche of marine anaerobic metabolisms expanded by particle microenvironments. *Nature Geoscience*, *11*(4), 263–268. https://doi.org/10.1038/s41561-018-0081-0

Bianchi, D., Dunne, J. P., Sarmiento, J. L., and Galbraith, E. D. (2012). Data-based estimates of suboxia, denitrification, and N2O production in the ocean and their sensitivities to dissolved O2. *Global Biogeochem. Cycles*, 26(2):GB2009.

Boyer, T. P., Baranova, O., Locarnini, R. A., & Zweng, M. (2019). WORLD OCEAN ATLAS 2018 Product Documentation Ocean Climate Laboratory NCEI / NESDIS / NOAA NOAA National. . . *ResearchGate*. https://doi.org/10.13140/RG.2.2.34758.01602

Busecke, J., Resplandy, L., Ditkovsky, S. J., & John, J. (2022). Diverging Fates of the Pacific Ocean Oxygen Minimum Zone and Its Core in a Warming World. *AGU Advances*, *3*(6). https://doi.org/10.1029/2021av000470

Busecke, J., Resplandy, L., & Dunne, J. P. (2019). The Equatorial Undercurrent and the Oxygen Minimum Zone in the Pacific. *Geophysical Research Letters*, *46*(12), 6716–6725. https://doi.org/10.1029/2019gl082692

Cabré, A., Marinov, I., Bernardello, R., & Bianchi, D. (2015). Oxygen minimum zones in the tropical Pacific across CMIP5 models: mean state differences and climate change trends. *Biogeosciences*, *12*(18), 5429–5454. https://doi.org/10.5194/bg-12-5429-2015

Callbeck, C. M., Lavik, G., Stramma, L., Kuypers, M. M. M., & Bristow, L. A. (2017). Enhanced N Loss by Eddy-Induced Vertical Transport in the Offshore Peruvian Oxygen Minimum Zone. *PLOS ONE, 12*(1), e0170059. https://doi.org/10.1371/journal.pone.0170059

Carton, J. A., Chepurin, G. A., & Chen, L. (2018). SODA3: A New Ocean Climate Reanalysis. *Journal of Climate*, *31*(17), 6967–6983. https://doi.org/10.1175/jcli-d-18-0149.1

Castro, C. L., Chavez, F. P., & Collins, C. A. (2001). Role of the California Undercurrent in the export of denitrified waters from the eastern tropical North Pacific. *Global Biogeochemical Cycles, 15*(4), 819–830. https://doi.org/10.1029/2000gb001324

Chang, B. X., Devol, A. H., & Emerson, S. (2010). Denitrification and the N gas excess in the eastern tropical South Pacific oxygen deficient zone. *Deep-sea Research Part I-oceanographic Research Papers*, *57*(9), 1092–1101. https://doi.org/10.1016/j.dsr.2010.05.009

Codispoti, L. A. (1973). *Denitrification in the Eastern Tropical North Pacific*. PhD thesis, University of Washington.

Codispoti, L. (2010). Interesting Times for Marine N $_2$ O. *Science*, *327*(5971), 1339–1340. https://doi.org/10.1126/science.1184945

Codispoti, L. A. and Packard, T. T. (1980). Denitrification rates in the eastern tropical southpacific. *J. Mar. Res.*, 38:453—-477.

Codispoti, L. A. and Richards, F. A. (1976). JSTORAn Analysis of the Horizontal Regime of Denitrification in the Eastern Tropical North Pacific. *Limnology and Oceanography*.

Dalsgaard, T., Thamdrup, B., Farías, L., & Revsbech, N. P. (2012). Anammox and denitrification in the oxygen minimum zone of the eastern South Pacific. *Limnology and Oceanography*, *57*(5), 1331–1346. https://doi.org/10.4319/lo.2012.57.5.1331

Deutsch, C., Gruber, N., and Key, R. M. (2001). Denitrification and N2 fixation in the Pacific Ocean. *Global Biogeochemical Cycles*.

Deutsch, C., Emerson, S., & Thompson, L. (2006). Physical-biological interactions in North Pacific oxygen variability. *Journal of Geophysical Research*, *111*(C9). https://doi.org/10.1029/2005jc003179

Deutsch, C., Sarmiento, J. L., Sigman, D. M., Gruber, N., & Dunne, J. P. (2007). Spatial coupling of N inputs and losses in the ocean. *Nature, 445*(7124), 163–167. https://doi.org/10.1038/nature05392

Deutsch, C., Brix, H., Ito, T., Frenzel, H., & Thompson, L. (2011). Climate-Forced Variability of Ocean Hypoxia. *Science, 333*(6040), 336–339. https://doi.org/10.1126/science.1202422

Deutsch, C., Berelson, W. M., Thunell, R. C., Weber, T., Tems, C., McManus, J., Crusius, J., Ito, T., Baumgartner, T. S., Ferreira, V., Mey, J. L., & Van Geen, A. (2014). Centennial changes in North Pacific anoxia linked to tropical trade winds. *Science, 345*(6197), 665–668. https://doi.org/10.1126/science.1252332

DeVries, T., Deutsch, C., Primeau, F., Chang, B., and Devol, A. (2012). Global rates of watercolumn denitrification derived from N gas measurements. *Nature Geoscience*, 5:547–550.

DeVries, T., Deutsch, C., Rafter, P. A., & Primeau, F. (2013). Marine denitrification rates determined from a global 3-D inverse model. *Biogeosciences*, *10*(4), 2481–2496. https://doi.org/10.5194/bg-10-2481-2013

DeVries, T., & Weber, T. (2017). The export and fate of organic matter in the ocean: New constraints from combining satellite and oceanographic tracer observations. *Global Biogeochemical Cycles*, *31*(3), 535–555. https://doi.org/10.1002/2016gb005551

Dussin, R., Barnier, B., Brodeau, L., & Molines, J. M. (2016). The Making Of the DRAKKAR FORCING SET DFS5. In *CNRS*. Retrieved March 4, 2023, from https://www.drakkar-ocean.eu/publications/reports/report_DFS5v3_April2016.pdf

Duteil, O., Frenger, I., & Getzlaff, J. (2021). The riddle of eastern tropical Pacific Ocean oxygen levels: the role of the supply by intermediate-depth waters. Ocean Science, 17(5), 1489–1507. https://doi.org/10.5194/os-17-1489-2021

Echevin, V., Aumont, O., Ledesma, J., & Flores, G. (2008). The seasonal cycle of surface chlorophyll in the Peruvian upwelling system: A modelling study. *Progress in Oceanography*, *79*(2–4), 167–176. https://doi.org/10.1016/j.pocean.2008.10.026

Elkins, J. W. (1978). *Aquatic sources and sinks for nitrous oxide*. PhD thesis, Harvard.

Falkowski, P. G. (1997). Evolution of the N cycle and its influence on the biological sequestration of CO2 in the ocean. *Nature*, *387*(6630), 272–275. https://doi.org/10.1038/387272a0

FAO. (n.d.). *Review of the state of world marine fishery resources*. FAO.org. Retrieved May 2, 2023, from https://www.fao.org/3/y5852e/Y5852E07.htm

Fiedler, P. C. (2002). The annual cycle and biological effects of the Costa Rica Dome. *Deep-sea Research Part I-oceanographic Research Papers*, *49*(2), 321–338. https://doi.org/10.1016/s0967-0637(01)00057-7

Frenger, I., Bianchi, D., Stührenberg, C., Oschlies, A., Dunne, J. P., Deutsch, C., Galbraith, E. D., & Schütte, F. (2018). Biogeochemical Role of Subsurface Coherent Eddies in the Ocean: Tracer Cannonballs, Hypoxic Storms, and Microbial Stewpots? *Global Biogeochemical Cycles*, *32*(2), 226–249. https://doi.org/10.1002/2017gb005743

Frischknecht, M. F. (2018). *New Perspectives on the Three- Dimensional Cycling of Carbon and Nutrients in the California Current System and its Response to ENSO* [Doctoral Thesis]. ETH Zurich.

Frischknecht, M., Münnich, M., & Gruber, N. (2018). Origin, Transformation, and Fate: The Three-Dimensional Biological Pump in the California Current System. *Journal of Geophysical Research: Oceans*, *123*(11), 7939–7962. https://doi.org/10.1029/2018jc013934

Frölicher, T. L., Joos, F., Plattner, G., Steinacher, M., & Doney, S. C. (2009). Natural variability and anthropogenic trends in oceanic oxygen in a coupled carbon cycle-climate model ensemble. *Global Biogeochemical Cycles*, *23*(1), n/a. https://doi.org/10.1029/2008gb003316

Frölicher, T. L., Aschwanden, M., Gruber, N., Jaccard, S. L., Dunne, J. P., & Paynter, D. (2020). Contrasting Upper and Deep Ocean Oxygen Response to Protracted Global Warming. *Global Biogeochemical Cycles*, *34*(8). https://doi.org/10.1029/2020gb006601

Gazitúa, M. C., Vik, D. R., Roux, S., Gregory, A. C., Bolduc, B., Widner, B., Mulholland, M. R., Hallam, S. J., Ulloa, O., & Sullivan, M. B. (2021). Potential virus-mediated N cycling in oxygen-depleted oceanic waters. *The ISME Journal*, *15*(4), 981–998. https://doi.org/10.1038/s41396-020-00825-6

Goering, J. (1968). Denitrification in the oxygen minimum layer of the eastern tropical Pacific Ocean. *Deep Sea Research and Oceanographic Abstracts*. https://doi.org/10.1016/0011-7471(68)90037-5

Graf, D., Jones, C. W., & Hallin, S. (2014). Intergenomic Comparisons Highlight Modularity of the Denitrification Pathway and Underpin the Importance of Community Structure for N2O Emissions. *PLOS ONE*, *9*(12), e114118. https://doi.org/10.1371/journal.pone.0114118

Gruber, N. (2008). The Marine N Cycle. In *Elsevier eBooks* (pp. 1–50). https://doi.org/10.1016/b978-0-12-372522-6.00001-3

Gruber, N. (2011). Warming up, turning sour, losing breath: ocean biogeochemistry under global change. *Philosophical Transactions of the Royal Society A: Mathematical, Physical and Engineering Sciences, 369*(1943), 1980–1996. https://doi.org/10.1098/rsta.2011.0003

Gruber, N. (2016). Elusive marine nitrogen fixation. *Proceedings of the National Academy of Sciences of the United States of America*, *113*(16), 4246–4248. https://doi.org/10.1073/pnas.1603646113

Gruber, N., & Galloway, J. N. (2008). An Earth-system perspective of the global N cycle. *Nature, 451*(7176), 293–296. https://doi.org/10.1038/nature06592

Gruber, N., Boyd, P. W., Frölicher, T. L., & Vogt, M. (2021). Biogeochemical extremes and compound events in the ocean. *Nature, 600*(7889), 395–407. https://doi.org/10.1038/s41586-021 03981-7

Gruber, N., & Sarmiento, J. L. (1997). Global patterns of marine N fixation and denitrification. *Global Biogeochemical Cycles*, *11*(2), 235–266. https://doi.org/10.1029/97gb00077

Harris, C.R., Millman, K.J., van der Walt, S.J. et al. *Array programming with NumPy*. Nature 585, 357–362 (2020). DOI: 10.1038/s41586-020-2649-2.

Haumann, F. A., Gruber, N., Münnich, M., Frenger, I., & Kern, S. (2016). Sea-ice transport driving Southern Ocean salinity and its recent trends. *Nature*, *537*(7618), 89–92. https://doi.org/10.1038/nature19101

Hersbach, H., Bell, B., Berrisford, P., Hirahara, S., Horányi, A., Muñoz-Sabater, J., Nicolas, J., Peubey, C., Radu, R. N., Schepers, D., Simmons, A., Soci, C., Abdalla, S., Abellan, X., Balsamo, G., Bechtold, P., Biavati, G., Bidlot, J., Bonavita, M., . . . Villaume, S. (2020). The ERA5 global reanalysis. *Quarterly Journal of the Royal Meteorological Society*, *146*(730), 1999–2049. https://doi.org/10.1002/qj.3803

Horak, R. E. A., Ruef, W., Ward, B. B., & Devol, A. H. (2016). Expansion of denitrification and anoxia in the eastern tropical North Pacific from 1972 to 2012. *Geophysical Research Letters, 43*(10), 5252–5260. https://doi.org/10.1002/2016gl068871

Iversen, M. H., & Ploug, H. (2010). Ballast minerals and the sinking carbon flux in the ocean: carbon-specific respiration rates and sinking velocity of marine snow aggregates. *Biogeosciences*, *7*(9), 2613–2624. https://doi.org/10.5194/bg-7-2613-2010

José, Y. S., Stramma, L., Schmidtko, S., & Oschlies, A. (2019). ENSO-driven fluctuations in oxygen supply and vertical extent of oxygen-poor waters in the oxygen minimum zone of the Eastern Tropical South Pacific. *Biogeosciences*. In press. https://doi.org/10.5194/bg-2019-155

Kalvelage, T., Lavik, G., Lam, P., Contreras, S., Arteaga, L., Löscher, C. R., Oschlies, A., Paulmier, A., Stramma, L., & Kuypers, M. M. M. (2013). N cycling driven by organic matter export in the South Pacific oxygen minimum zone. *Nature Geoscience, 6*(3), 228–234. https://doi.org/10.1038/ngeo1739

Karl, D. M., Michaels, A. F., Bergman, B., Capone, D., Carpenter, E. P., Letelier, R. M., Lipschultz, F., Paerl, H. W., Sigman, D. M., & Stal, L. J. (2002). DiN fixation in the world's oceans. In *Springer eBooks* (pp. 47–98). https://doi.org/10.1007/978-94-017-3405-9_2

Karstensen, J., Stramma, L., & Visbeck, M. (2008). Oxygen minimum zones in the eastern tropical Atlantic and Pacific oceans. *Progress in Oceanography*, *77*(4), 331–350. https://doi.org/10.1016/j.pocean.2007.05.009

Keeling, R. F., & Garcia, H. G. (2002). The change in oceanic O $_2$ inventory associated with recent global warming. *Proceedings of the National Academy of Sciences of the United States of America*, *99*(12), 7848–7853. https://doi.org/10.1073/pnas.122154899

Keeling, R. F., Körtzinger, A., & Gruber, N. (2010). Ocean Deoxygenation in a Warming World. *Annual Review of Marine Science*, *2*(1), 199–229. https://doi.org/10.1146/annurev.marine.010908.163855

Köhn, E. E. (2023). *Water column perspectives on marine heatwaves and low oxygen extreme events in the Eastern Pacific* [Doctoral Thesis]. ETH Zurich.

Köhn, E. E., Münnich, M., Vogt, M., Desmet, F., & Gruber, N. (2022). Strong Habitat Compression by Extreme Shoaling Events of Hypoxic Waters in the Eastern Pacific. Journal of Geophysical Research: Oceans, 127(6). https://doi.org/10.1029/2022jc018429

Köhn, E. E., Gruber, N., Munnich, M., and Vogt, M. (2023a). On the vertical structure and propagation of marine heatwaves in the Eastern Pacific. [Manuscript in preparation].

Köhn, E. E., Gruber, N., Munnich, M., and Vogt, M. (2023b) Seasonal and inter-annual variability of vertically propagating marine heatwaves in the Eastern Pacific. [Manuscript in preparation].

Kwiecinski, J. V., & Babbin, A. R. (2021). A High-Resolution Atlas of the Eastern Tropical Pacific Oxygen Deficient Zones. *Global Biogeochemical Cycles*, *35*(12). https://doi.org/10.1029/2021gb007001

Lam, P., & Kuypers, M. M. M. (2011). Microbial N Cycling Processes in Oxygen Minimum Zones. *Annual Review of Marine Science*, *3*(1), 317–345. https://doi.org/10.1146/annurev-marine-120709-142814

Lauvset, S. K., Key, R. M., Olsen, A., Van Heuven, S., Velo, A., Lin, X., Schirnick, C., Kozyr, A., Tanhua, T., Hoppema, M., Jutterström, S., Steinfeldt, R., Jeansson, E., Ishii, M., Pérez, F. F., Suzuki, T., & Watelet, S. (2016). A new global interior ocean

mapped climatology: the 1° × 1° GLODAP version 2. *Earth System Science Data*, *8*(2), 325–340. https://doi.org/10.5194/essd-8-325-2016.

Levin, L. A. (2018). Manifestation, Drivers, and Emergence of Open Ocean Deoxygenation. *Annual Review of Marine Science*, *10*(1), 229–260. https://doi.org/10.1146/annurev-marine-121916-063359

Lévy, M., Resplandy, L., Palter, J. B., Couespel, D., & Lachkar, Z. (2022). The crucial contribution of mixing to present and future ocean oxygen distribution. In *Elsevier eBooks* (pp. 329–344). https://doi.org/10.1016/b978-0-12-821512-8.00020-7

Liu, K.-K. (1976). *Geochemistry of inorganic N compounds in two marine environments: the Santa Barbara Basin and the ocean off Peru* [PhD Thesis]. University of California, Los Angeles.

Longhurst, A. R., & Harrison, W. T. A. (1989). The biological pump: Profiles of plankton production and consumption in the upper ocean. *Progress in Oceanography*, *22*(1), 47–123. https://doi.org/10.1016/0079-6611(89)90010-4

Löscher, C. R., Bange, H. W., Schmitz, R. A., Callbeck, C. M., Engel, A., Hauss, H., Kanzow, T., Kiko, R., Lavik, G., Loginova, A., Melzner, F., Meyer, J., Neulinger, S. C., Pahlow, M., Riebesell, U., Schunck, H., Thomsen, S., & Wagner, H. (2016). Water column biogeochemistry of oxygen minimum zones in the eastern tropical North Atlantic and eastern tropical South Pacific oceans. *Biogeosciences, 13*(12), 3585–3606. https://doi.org/10.5194/bg-13-3585-2016

Luyten, J. R., Pedlosky, J., & Stommel, H. (1983). The Ventilated Thermocline. *Journal of Physical Oceanography*, *13*(2), 292–309. https://doi.org/10.1175/1520-0485(1983)013

Ma, Y., Yuan, N., Dong, T., & Dong, W. (2022). On the Pacific Decadal Oscillation Simulations in CMIP6 Models: A New Test-Bed from Climate Network Analysis. *Asia-pacific Journal of Atmospheric Sciences*, *59*(1), 17–28. https://doi.org/10.1007/s13143-022-00286-1

Mantua, N. J. (1997). A Pacific Interdecadal Climate Oscillation with Impacts on Salmon Production. *AMETSOC*. https://doi.org/10.1175/1520-0477(1997)078

Mantua, N. J., & Hare, S. R. (2002). The Pacific Decadal Oscillation. *Journal of Oceanography*, *58*(1), 35–44. https://doi.org/10.1023/a:1015820616384

Marchesiello, P., McWilliams, J.C., & Shchepetkin, A.F. (2003). Equilibrium Structure and Dynamics of the California Current System. *Journal of Physical Oceanography, 33*(4), 753–783. https://doi.org/10.1175/1520-0485(2003)33

Margolskee, A., Frenzel, H., Emerson, S. U., & Deutsch, C. (2019). Ventilation Pathways for the North Pacific Oxygen Deficient Zone. *Global Biogeochemical Cycles*, *33*(7), 875–890. https://doi.org/10.1029/2018gb006149

McCreary, J. P., Lee, H. J., & Enfield, D. B. (1989). The response of the coastal ocean to strong offshore winds: With application to circulations in the Gulfs of Tehuantepec and Papagayo. *Journal of Marine Research*, *47*(1), 81–109. https://doi.org/10.1357/002224089785076343

Moore, J. K., Doney, S. C., & Lindsay, K. (2004). Upper ocean ecosystem dynamics and iron cycling in a global three-dimensional model. *Global Biogeochemical Cycles, 18*(4), n/a-n/a. https://doi.org/10.1029/2004gb002220

Moore, J. K., Lindsay, K., Doney, S. C., Long, M. C., & Misumi, K. (2013). Marine Ecosystem Dynamics and Biogeochemical Cycling in the Community Earth System Model [CESM1(BGC)]: Comparison of the 1990s with the 2090s under the RCP4.5 and RCP8.5 Scenarios. *Journal of Climate, 26*(23), 9291–9312. https://doi.org/10.1175/jcli-d-12-00566.1

NASA Goddard Space Flight Center, Ocean Ecology Laboratory, Ocean Biology Processing Group. Sea-viewing Wide Field-of-view Sensor (SeaWiFS) Chlorophyll Data; 2022 Reprocessing. NASA OB.DAAC, Greenbelt, MD, USA. doi: 10.5067/ORBVIEW-2/SEAWIFS/L3M/CHL/2022.
Accessed on 05/25/2023

NCEI. (n.d.). *El Niño/Southern Oscillation (ENSO) | National Centers for Environmental Information (NCEI)*. Retrieved May 22, 2023, from https://www.ncei.noaa.gov/access/monitoring/enso/

Neuer, S., Davenport, R., Freudenthal, T., Wefer, G., Llinás, O., Rueda, M. J., Steinberg, D. K., & Karl, D. M. (2002). Differences in the biological carbon pump at three subtropical ocean sites. *Geophysical Research Letters*, *29*(18), 32–34. https://doi.org/10.1029/2002gl015393

NOAA.(2009). *Climate Variability: Oceanic Niño Index*. https://www.climate.gov/news-features/understanding-climate/climate-variability-oceanic-ni%C3%B1o-index

Oschlies, A., Schulz, K. G., Riebesell, U., & Schmittner, A. (2008). Simulated 21st century's increase in oceanic suboxia by CO_2-enhanced biotic carbon export. *Global Biogeochemical Cycles*, *22*(4), n/a. https://doi.org/10.1029/2007gb003147

Pajares, S., & Ramos, R. (2019). Processes and Microorganisms Involved in the Marine N Cycle: *Knowledge and Gaps. Frontiers in Marine Science, 6*. https://doi.org/10.3389/fmars.2019.00739

Paulmier, A., Ruiz-Pino, D., Garçon, V., & Farías, L. (2006). Maintaining of the Eastern South Pacific Oxygen Minimum Zone (OMZ) off Chile. *Geophysical Research Letters*, *33*(20). https://doi.org/10.1029/2006gl026801

Paulmier, A., & Ruiz-Pino, D. (2009). Oxygen minimum zones (OMZs) in the modern ocean. *Progress in Oceanography*, *80*(3–4), 113–128. https://doi.org/10.1016/j.pocean.2008.08.001

Pennington, J. T., Mahoney, K. J., Kuwahara, V. S., Kolber, D. D., Calienes, R., & Chavez, F. P. (2006). Primary production in the eastern tropical Pacific: A review. *Progress in Oceanography*, *69*(2–4), 285–317. https://doi.org/10.1016/j.pocean.2006.03.012

Poupon, M. A., Resplandy, L., Lévy, M., & Bopp, L. (2023). Pacific Decadal Oscillation Influences Tropical Oxygen Minimum Zone Extent and Obscures Anthropogenic Changes. *Geophysical Research Letters*, *50*(7). https://doi.org/10.1029/2022gl102123

Rasmusson, E. M., & Wallace, J. L. (1983). Meteorological Aspects of the El Niño/Southern Oscillation. *Science*, *222*(4629), 1195–1202. https://doi.org/10.1126/science.222.4629.1195

Sarmiento, J. L., & Gruber, N. (2006). *Ocean Biogeochemical Dynamics*. Princeton University Press.

Schepetkin, A. F., & McWilliams, J. C. (2005). The regional oceanic modeling system (ROMS): a split-explicit, free-surface, topography-following-coordinate oceanic model. *Ocean Modelling, 9*(4), 347–404. https://doi.org/10.1016/j.ocemod.2004.08.002

Schmidtko, S., Stramma, L., & Visbeck, M. (2017). Decline in global oceanic oxygen content during the past five decades. *Nature*, *542*(7641), 335–339. https://doi.org/10.1038/nature21399

Pauli Virtanen, Ralf Gommers, Travis E. Oliphant, Matt Haberland, Tyler Reddy, David Cournapeau, Evgeni Burovski, Pearu Peterson, Warren Weckesser, Jonathan Bright, Stéfan J. van der Walt, Matthew Brett, Joshua Wilson, K. Jarrod Millman, Nikolay Mayorov, Andrew R. J. Nelson, Eric Jones, Robert Kern, Eric Larson, CJ Carey, İlhan Polat, Yu Feng, Eric W. Moore, Jake VanderPlas, Denis Laxalde, Josef Perktold, Robert Cimrman, Ian Henriksen, E.A. Quintero, Charles R Harris, Anne M. Archibald, Antônio H. Ribeiro, Fabian Pedregosa, Paul van Mulbregt, and SciPy 1.0 Contributors. (2020) SciPy 1.0: Fundamental Algorithms for Scientific Computing in Python**.** *Nature Methods*, 17(3), 261-272.

Sigman, D. M., & Casciotti, K. L. (2001). N Isotopes in the Ocean. In *Elsevier eBooks* (pp. 1884–1894). https://doi.org/10.1006/rwos.2001.0172

Stramma, L., Johnson, G. C., Sprintall, J., & Mohrholz, V. (2008). Expanding Oxygen-Minimum Zones in the Tropical Oceans. *Science, 320*(5876), 655–658. https://doi.org/10.1126/science.1153847

Stramma, L., Johnson, G. C., Firing, E., & Schmidtko, S. (2010). Eastern Pacific oxygen minimum zones: Supply paths and multidecadal changes. *Journal of Geophysical Research*, *115*(C9). https://doi.org/10.1029/2009jc005976

Stramma, L., Fischer, T., Grundle, D., Krahmann, G., Bange, H. W., & Marandino, C. A. (2016). Observed El Niño conditions in the eastern tropical Pacific in October 2015. *Ocean Science*, *12*(4), 861–873. https://doi.org/10.5194/os-12-861-2016

Strous, M., Fuerst, J. A., Kramer, E., Logemann, S., Muyzer, G., Van De Pas-Schoonen, K. T., Webb, R. I., Kuenen, J., & Jetten, M. S. M. (1999). Missing lithotroph identified as new planctomycete. *Nature*, *400*(6743), 446–449. https://doi.org/10.1038/22749

Tans, P. P., Fung, I., & Takahashi, T. (1990). Observational Contrains on the Global Atmospheric Co $_2$ Budget. *Science*, *247*(4949), 1431–1438. https://doi.org/10.1126/science.247.4949.1431

Thomsen, S., Kanzow, T., Colas, F., Echevin, V., Krahmann, G., & Engel, A. (2016). Do submesoscale frontal processes ventilate the oxygen minimum zone off Peru? *Geophysical Research Letters*, *43*(15), 8133–8142. https://doi.org/10.1002/2016gl070548

Tsunogai, S. (1971). Ammonia in the oceanic atmosphere and the cycle of N compounds through the atmosphere and the hydrosphere. *GEOCHEMICAL JOURNAL*, 5(2):57–67.

Vergara, O., Dewitte, B., Montes, I., Garçon, V., Ramos, M., Paulmier, A., & Pizarro, O. (2016). Seasonal variability of the oxygen minimum zone off Peru in a high-resolution regional coupled model. *Biogeosciences*, *13*(15), 4389–4410. https://doi.org/10.5194/bg-13-4389-2016

Voss, M., Bange, H. W., Dippner, J. W., Middelburg, J. J., Montoya, J., & Ward, B. B. (2013). The marine N cycle: recent discoveries, uncertainties and the potential relevance of climate change. *Philosophical Transactions of the Royal Society*, *368*(1621), 20130121. https://doi.org/10.1098/rstb.2013.0121

Wang, C., & Fiedler, P. C. (2006). ENSO variability and the eastern tropical Pacific: A review. *Progress in Oceanography, 69*(2–4), 239–266. https://doi.org/10.1016/j.pocean.2006.03.004

Ward, B. B., Devol, A. H., Rich, J. J., Chang, B. X., Bulow, S. E., Naik, H., Pratihary, A., & Jayakumar, A. (2009). Denitrification as the dominant N loss process in the Arabian Sea. *Nature, 461*(7260), 78–81. https://doi.org/10.1038/nature08276

Yang, S., & Gruber, N. (2016). The anthropogenic perturbation of the marine N cycle by atmospheric deposition: N cycle feedbacks and the 15 N Haber-Bosch effect. *Global Biogeochemical Cycles, 30*(10), 1418–1440. https://doi.org/10.1002/2016gb005421

Yang, S. (2017). *Dynamics of the contemporary marine N cycle* [Doctoral Thesis]. ETH Zurich.

Yang, S., Gruber, N., Long, M. C., & Vogt, M. (2017). ENSO-Driven Variability of Denitrification and Suboxia in the Eastern Tropical Pacific Ocean. *Global Biogeochemical Cycles, 31*(10), 1470–1487. https://doi.org/10.1002/2016gb005596

Zhou, Y., Gong, H., & Zhou, F. (2022). Responses of Horizontally Expanding Oceanic Oxygen Minimum Zones to Climate Change Based on Observations. *Geophysical Research Letters, 49*(6). https://doi.org/10.1029/2022gl097724

Appendix

Appendix A: Dataset ODZ Model Evaluation

Evaluation of the number of observations in the Kwiecinski and Babbin (2022) dataset. The left map on Figure A1 illustrates the depth-integrated number of observations at each grid cell. The right map visualized the number of observations below the 3 µmol kg^{-1} oxycline.

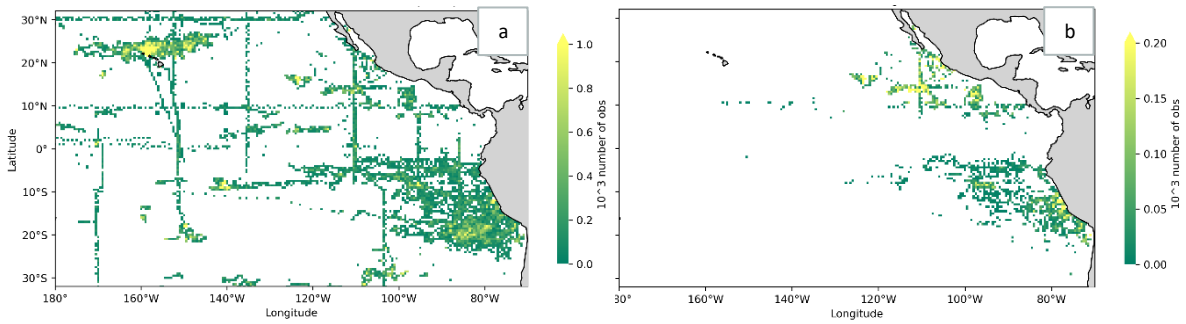

Figure A1. a) Mapped depth-integrated number of observations in the Kwiecinski and Babbin (2022) dataset in the study area. b) Mapped depth-integrated number of observations below the 3 µmol kg^{-1} oxycline.

Appendix B: NO_3^- and PO_4^{3-} Model Evaluations

Figure B1 depicts the WOA2018 NO_3^- concentrations regridded onto the model grid, and their anomalies to the model mean NO_3^- concentrations. Figure B2 shows the WOA2018 PO_4^{3-} concentrations regridded onto the model grid, and their anomalies to the model mean PO_4^{3-} concentrations.

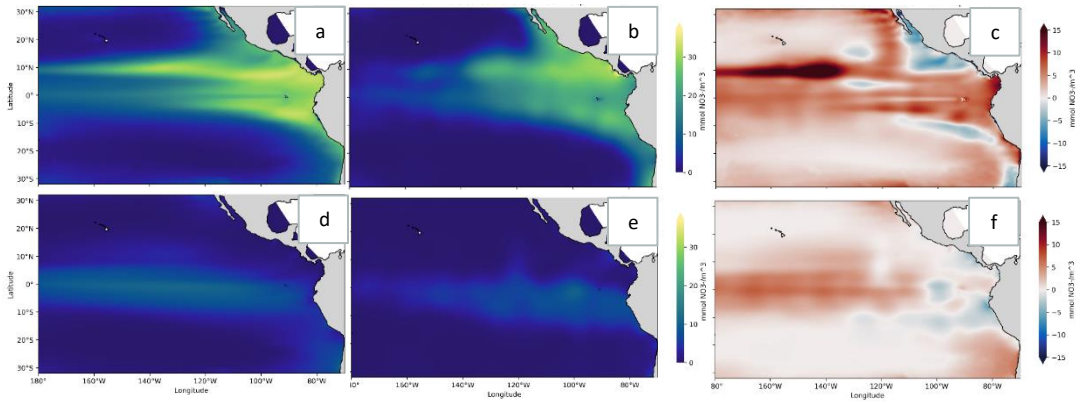

Figure B1. Mapped NO_3^- concentrations from model simulations (a and d), WOA2018 dataset (b and e), and anomalies (c and f), at the sea surface (a-c) and at 100m depth (d-f).

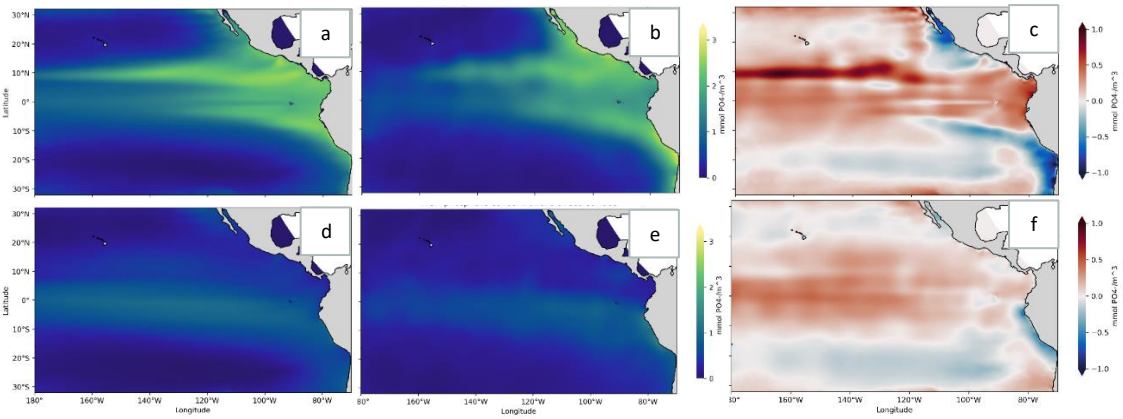

Figure B2. Mapped PO43- concentrations from model simulations (a and d), WOA2018 dataset (b and e), and anomalies (c and f), at the sea surface (a-c) and at 100m depth (d-f).

Appendix C: Point Locations Validation

In order to assess whether the five chosen point locations are representative of their respective regions, and to what degree and direction they are skewed, the mean WCD rates averaged over depth and over the hindcast for each point location and the 2D ODZ zone they are located in. The results show good overall agreement between the chosen points and their respective zones. Point A and D (both located in the ZONE90) are skewed towards higher WCD rates than in the mean of their zones.

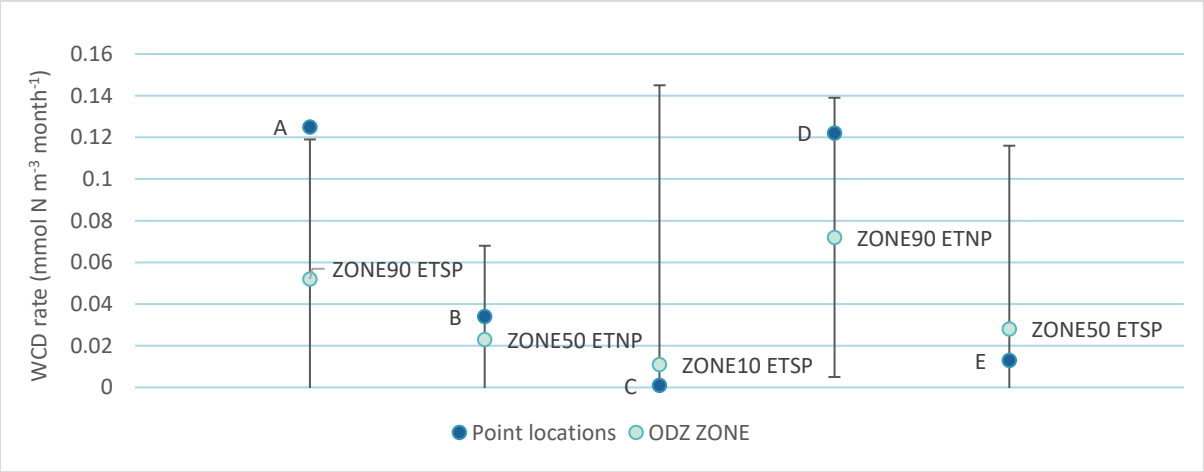

Figure C1. Plotted depth-averaged and time-averaged WCD rates for the five point locations (A-E, in dark blue) plotted in Figure 5, and for their respective 2D ODZ zones (light blue). Bars indicate the standard deviations of all gridpoints in each 2D ODZ zone.

Supplementary Material

Description of datasets used in this study

This study is based on ROMS-BEC model outputs from a 41 year hindcast from 1979 to 2019 over the Pacific Basin. The model output is stored in netCDF4 files, with a total of 41 files employed in this analysis. Each file encompasses all fields corresponding to each year of the hindcast. The structure of every netCDF4 file comprises six dimensions: (eta_rho, xi_rho, time, s_rho, xi_u, eta_v) with respective sizes of (1009, 701, 365, 64, 700, 1008). The dimensions 'eta_rho' and 'xi_rho' represent the two horizontal dimensions, referring to specific latitudes and longitudes calculated using a grid file. The 'time' dimension encompasses 365 fields, corresponding to each day of the year (366 fields for leap years). The 's_rho' dimension characterizes the vertical dimension from the sea surface down to a depth of 6500m through 64 s-levels. The velocity fields are described by 'xi_u' and 'eta_v'. Each file contains 36 variables, described in the aforementioned dimensions. Detailed descriptions of the variables employed in this study can be found in Table 6. The files are stored at the ETH Zurich's Research Collection and is under the responsibility of Nicolas Gruber (nicolas.gruber@env.ethz.ch). The model output was created by Köhn (2023). Table 7 outlines the additional datasets used in this study.

Table 6. ROMS-BEC model output variables used in this study

Variable	ROMS-BEC name	Unit	Description
WCD	DENITRIF	mmol N m^{-3} s^{-1}	Averaged water column denitrification
[NO_3^-]	NO3	mmol NO_3^- m^{-3}	Averaged nitrate concentration
[PO_4^{3-}]	PO4	mmol PO_4^{3-} m^{-3}	Averaged phosphate concentration
POC influx	POC_FLUX_IN	mmol C m^{-2} s^{-1}	Averaged POC flux into cell
[O_2]	O2	mmol O_2 m^{-3}	Averaged oxygen concentration
density	RHO	kg m^{-1}	Density anomaly

Table 7. Additional datasets used in this study

Variable	Data source	Unit	Temporal resolution	Spatial resolution	Underlying data period	Format	Link to dataset
$[NO_3^-]$	WOA2018 (Boyer at al., 2019)	mmol NO_3^- m^{-3}	Monthly climatologies	1° and 43 vertical levels	1955-2017	netCDF4	https://www.ncei.noaa.gov/access/world-ocean-atlas-2018/
$[PO_4^{3-}]$	WOA2018 (Boyer at al., 2019)	mmol PO_4^{3-} m^{-3}	Monthly climatologies	1° and 43 vertical levels	1955-2017	netCDF4	https://www.ncei.noaa.gov/access/world-ocean-atlas-2018/
POC export	DeVries and Weber (2017)	mmol C m^{-2} yr^{-1}	Annual	2° and 24 vertical levels	-	netCDF4	https://bg.copernicus.org/articles/10/2481/2013/bg-10-2481-2013.html
$[O_2]$	Kwiecinski and Babbin (2022)	µmol/kg	-	0.5°×0.5°×20 dbar	Data collected across 3 decades up to April 2019	netCDF4	https://agupubs.onlinelibrary.wiley.com/doi/10.1029/2021GB007001
PDO index	Mantua et al. (1997)	°C	Monthly	-	1979-2017	Text	http://research.jisao.washington.edu/pdo/PDO.latest.txt

Eidgenössische Technische Hochschule Zürich
Swiss Federal Institute of Technology Zurich

Declaration of originality

The signed declaration of originality is a component of every semester paper, Bachelor's thesis, Master's thesis and any other degree paper undertaken during the course of studies, including the respective electronic versions.

Lecturers may also require a declaration of originality for other written papers compiled for their courses.

I hereby confirm that I am the sole author of the written work here enclosed and that I have compiled it in my own words. Parts excepted are corrections of form and content by the supervisor.

Title of work (in block letters):

VARIABILITY OF WATER COLUMN DENITRIFICATION AND ITS DRIVERS IN THE EASTERN TROPICAL PACIFIC OXYGEN DEFICIENT ZONES

Authored by (in block letters):

For papers written by groups the names of all authors are required.

Name(s):	**First name(s):**
VAN LANGEN ROSON	ANDREA

With my signature I confirm that

- I have committed none of the forms of plagiarism described in the 'Citation etiquette' information sheet.
- I have documented all methods, data and processes truthfully.
- I have not manipulated any data.
- I have mentioned all persons who were significant facilitators of the work.

I am aware that the work may be screened electronically for plagiarism.

Place, date	**Signature(s)**
Zurich, 07.06.2023	Andrea

For papers written by groups the names of all authors are required. Their signatures collectively guarantee the entire content of the written paper.